

# CANADIAN JOURNAL OF RESEARCH

VOLUME 28

MARCH, 1950

NUMBER 2

## — SECTION A —

### PHYSICAL SCIENCES

#### Contents

	Page
Selective Reflection from Mercury and Cadmium Vapors— <i>H. L. Welsh, J. Kastner, and A. C. Lauriston</i> - - - - -	93
Integrator-Expander Circuits for the Control of the Maximum X-ray Energy from the Betatron— <i>L. Katz, A. G. McNamara, P. A. Forsyth, R. N. H. Haslam, and H. E. Johns</i> - - -	113
A More Exact Fresnel Field Diffraction Relation— <i>G. A. Woonton</i>	120
Effect of the Illumination of the Negative on the Resolving Power of a Projection Print— <i>P. A. Tate</i> - - - - -	127
Isotope Shift in the Resonance Lines of Zinc— <i>M. F. Crawford, W. M. Gray, F. M. Kelly, and A. L. Schawlow</i> - - -	138
Forbidden Transitions in Diatomic Molecules. I. The Quadrupole Rotation-Vibration Spectrum of $H_2$ — <i>G. Herzberg</i>	144
A Saturated Core Recording Magnetometer— <i>D. C. Rose and J. N. Bloom</i> - - - - -	153
Formation of Radioactive Surface Films on Minerals— <i>T. G. Church</i> - - - - -	164
Electron Diffusion in a Spherical Cavity— <i>A. D. MacDonald and Sanborn C. Brown</i> - - - - -	168
Tables of the Function $e^{-az/\sqrt{M(a; \gamma; z)}}$ — <i>A. D. MacDonald</i>	175
The Microwave Absorption Spectrum of Methyl Alcohol— <i>Barbara M. Girdwood</i> - - - - -	180
Energy Distribution of Fission Fragments from $U^{235}$ and $U^{238}$ — <i>D. C. Brunton and G. C. Hanna</i> - - - - -	190

NATIONAL RESEARCH COUNCIL  
OTTAWA, CANADA

## CANADIAN JOURNAL OF RESEARCH

The *Canadian Journal of Research* is issued in six sections, as follows:

- |                       |                        |
|-----------------------|------------------------|
| A. Physical Sciences  | D. Zoological Sciences |
| B. Chemical Sciences  | E. Medical Sciences    |
| C. Botanical Sciences | F. Technology          |

For the present, Sections A, C, D, and E are to be issued six times annually, and Sections B and F, twelve times annually, each under separate cover, with separate pagination.

The *Canadian Journal of Research* is published by the National Research Council of Canada under authority of the Chairman of the Committee of the Privy Council on Scientific and Industrial Research. The *Canadian Journal of Research* is edited by a joint Editorial Board consisting of members of the National Research Council of Canada, the Royal Society of Canada, and the Chemical Institute of Canada.

Sections B and F of the *Canadian Journal of Research* have been chosen by the Chemical Institute of Canada as its medium of publication for scientific papers.

### EDITORIAL BOARD

<i>Representing</i> NATIONAL RESEARCH COUNCIL	<i>Representing</i> ROYAL SOCIETY OF CANADA
<p>DR. H. P. ARMES (<i>Chairman</i>), Dean of the University, University of Manitoba, Winnipeg, Man.</p> <p>*DR. G. H. HENDERSON Professor of Mathematical Physics, Dalhousie University, Halifax.</p> <p>DR. ROBERT NEWTON, President, University of Alberta, Edmonton, Alta.</p> <p>DR. C. H. BEST, The Banting and Best Department of Medical Research, University of Toronto, Toronto.</p>	<p>DR. A. NORMAN SHAW, Chairman, Department of Physics, McGill University, Montreal.</p> <p>DR. J. W. T. SPINKS, Head, Department of Chemistry, University of Saskatchewan, Saskatoon.</p> <p>DR. H. S. JACKSON, Head, Department of Botany University of Toronto, Toronto.</p> <p>DR. E. HORNE CRAIGIE, Department of Zoology, University of Toronto, Toronto.</p>
	} Section III
	} Section V
<i>Ex officio</i>	<i>Representing</i> THE CHEMICAL INSTITUTE OF CANADA
<p>DR. LÉO MARION, Editor-in-Chief, Division of Chemistry, National Research Laboratories, Ottawa.</p> <p>DR. H. H. SAUNDERSON, Director, Division of Information Services, National Research Council, Ottawa.</p>	<p>DR. H. G. THODE, Department of Chemistry, McMaster University, Hamilton.</p>

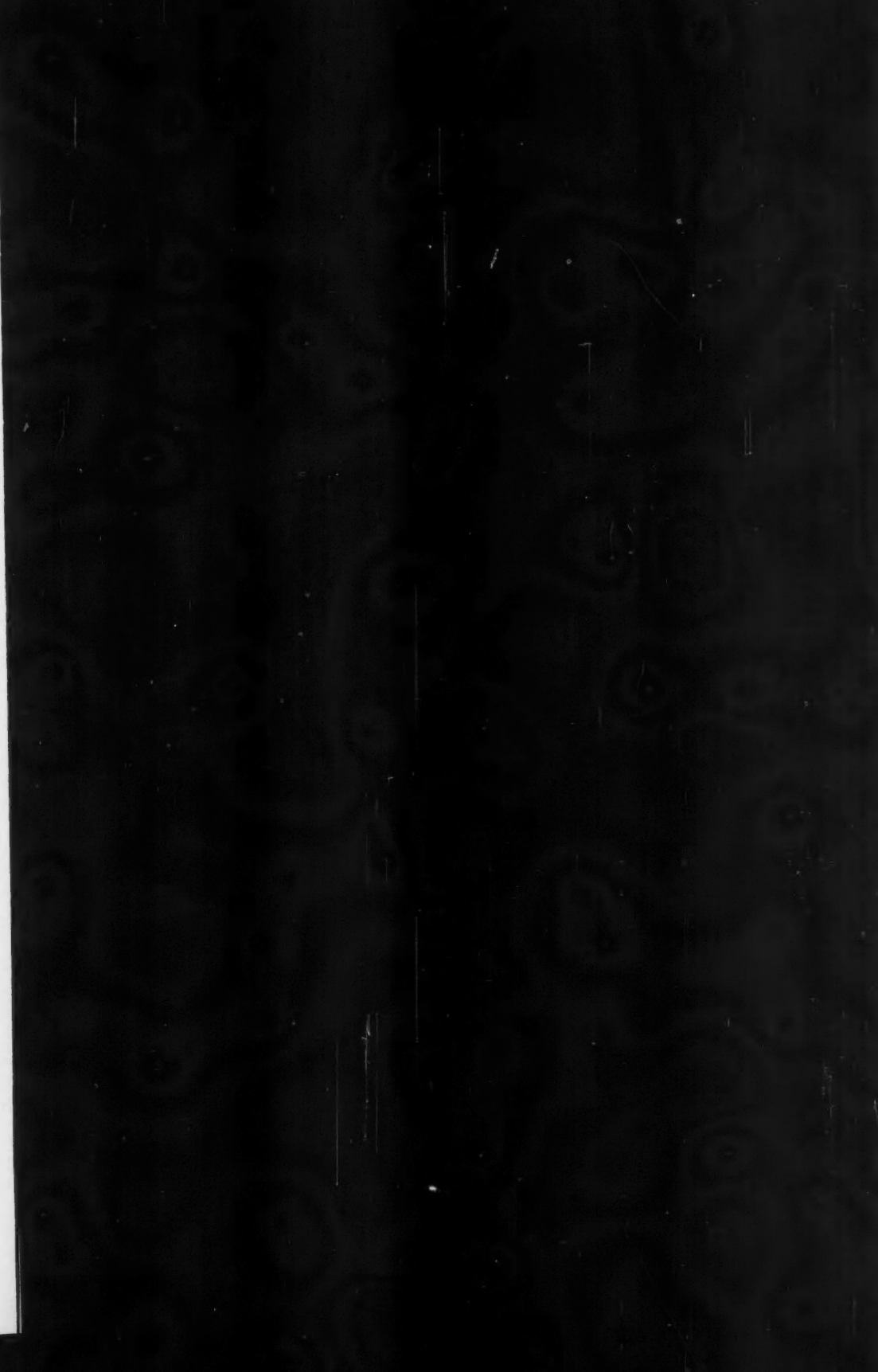
### EDITORIAL COMMITTEE

Editor-in-Chief, Editor, Section A, Editor, Section B, Editor, Section C,	DR. LÉO MARION DR. A. NORMAN SHAW DR. J. W. T. SPINKS DR. H. G. THODE DR. H. S. JACKSON	Editor, Section D, Editor, Section E, Editor, Section F,	DR. E. HORNE CRAIGIE DR. J. B. COLLIP DR. J. A. ANDERSON DR. A. NORMAN SHAW DR. H. G. THODE
--	---	--	---

Manuscripts should be addressed:

*Editor-in-Chief,  
Canadian Journal of Research,  
National Research Council, Ottawa, Canada.*

\*Deceased.







# Canadian Journal of Research

Issued by THE NATIONAL RESEARCH COUNCIL OF CANADA

VOL. 28, SEC. A.

MARCH, 1950

NUMBER 2

## SELECTIVE REFLECTION FROM MERCURY AND CADMIUM VAPORS<sup>1</sup>

BY H. L. WELSH, J. KASTNER<sup>2</sup>, AND A. C. LAURISTON<sup>3</sup>

### Abstract

Selective reflection from mercury and cadmium vapors in the neighborhood of the resonance lines was investigated quantitatively using incident light of continuous spectral distribution. For a given experimental arrangement the lowest vapor density (atoms per cubic centimeter) at which selective reflection could be detected at Hg 2537 Å, Cd 2288 Å, and Cd 3261 Å was inversely proportional to the oscillator strength ( $f$ -value) of the absorption line. Contours of the selective reflection of the Hg 2537 Å and Cd 2288 Å lines were obtained over a large range of vapor densities up to  $80 \times 10^{18}$  atoms per cc. At this density the cadmium reflection extended over several thousand  $\text{cm}^{-1}$  compared to about a hundred  $\text{cm}^{-1}$  for mercury. The general features of the reflection contours can be explained by the theory of reflection from an absorbing medium. Fitting a theoretical curve to the experimental reflection contour yields values of the oscillator strength and the damping constant. For Hg 2537 Å and Cd 2288 Å the  $f$ -values are 0.0268 and 1.40 respectively, in good agreement with those found by other methods. The damping constant,  $\gamma$ , varies as the square root of the number of atoms per cubic centimeter, indicating that the mechanism of selective reflection is not the same as that for absorption and emission. An empirical areal law for selective reflection confirms the relationship  $\gamma \propto \sqrt{N}$ . A shift of the resonance frequency of the order of magnitude of the coupling shift calculated by Weisskopf was observed for Hg 2537 Å. Deviations from theory at both high and low pressures were observed for Cd 2288 Å. The low pressure deviation takes the form of a line of residual intensity at the resonance frequency, which may be due to a different kind of selective reflection.

### Introduction

Selective reflection of light from a metallic vapor was first observed by Wood (20). When a quartz bulb containing mercury vapor at room temperatures was irradiated with the unreversed resonance line 2537 Å, the vapor throughout the whole bulb emitted the resonance line in fluorescence. As the vapor pressure was increased the fluorescence was confined more and more to the surface of the vapor in the path of the incident light. The surface fluorescence diminished in intensity with further increase in pressure until it was no longer observable. However, in this region of vapor pressure (*c.* 80 mm.), Wood observed that the reflection of the resonance line from the quartz-mercury vapor surface was enhanced and that its intensity increased steadily with increasing vapor pressure. The polarization characteristics of the selec-

<sup>1</sup> Manuscript received September 20, 1949.

Contribution from the McLennan Laboratory, University of Toronto, Toronto, Ont.

<sup>2</sup> Holder of scholarships under the National Research Council of Canada, 1946-49. Now in the Physics Division, National Research Laboratories, Ottawa, Canada.

<sup>3</sup> Holder of the E. F. Burton Fellowship in Physics, School of Graduate Studies, University of Toronto, 1948-49.

tive reflection were qualitatively the same as those of light reflected from a metallic surface. It was also found that the immediate neighborhood of the line was a region of anomalous reflection, with high intensity on the short wave-length side and low intensity on the long wave-length side. Wood pointed out that this intensity distribution could be explained by the variation of the refractive index of the vapor in the neighborhood of a strong absorption line, as given by anomalous dispersion theory.

Resonance fluorescence and selective reflection are of quite different natures. Rump (13), using the sharp line from a primary mercury resonance lamp, showed that the half-width of the line in selective reflection was the same as that of the incident line, whereas the half-width of the line in fluorescence was dependent on the temperature of the vapor. The effect of foreign gases on the intensity of the reflection was investigated by Schnettler (14). The reflected intensity decreased only 15% when two-thirds of an atmosphere of hydrogen or carbon dioxide was introduced into the tube containing the mercury vapor. It is well known, however, that only small pressures (*c.* 1 mm.) of these gases are necessary to produce considerable quenching of the resonance fluorescence at room temperature. Schnettler therefore concluded that a finite lifetime of the excited state cannot be involved in the process of selective reflection. This view is confirmed by the recent work of Hansen and Webb (7). When a mercury vapor surface was illuminated intermittently with resonance radiation, the selective reflection, unlike the resonance fluorescence, did not persist between the light pulses. The resolution of the timing method was about one-fortieth of the lifetime of the excited state of the free atom.

It is apparent that selective reflection has been investigated much less extensively than the related phenomenon of resonance fluorescence, although its study might be expected to yield useful information concerning the interaction of light and matter. Regular reflection is by its nature a coherent process. Classically, partial coherence is introduced into resonance fluorescence when the distance between the atoms becomes small compared to the wave-length of the light. Theoretical discussions on this basis have been given by Burton (2) and Fermi (4). An explanation in terms of the quantum theory is more difficult. Weisskopf (16), in the extension of his quantum theory of resonance fluorescence to gases at high densities, has deduced that the fluorescence has a definite phase relationship with the incident light. He states that this explains the selective reflection observed by Wood. The theory, however, is not complete enough to explain in detail the experimental results.

In the present experimental investigation attempts were made to observe selective reflection from other metallic vapors. For cadmium the reflection was found to be easily observable at the resonance line 2288 Å. The other resonance line at 3261 Å was also observed in reflection at high vapor pressures (*c.* 20 atm.). The effect could not be observed in thallium because of the difficulty of containing the vapor in a quartz tube at very high temperatures.

Some of the possibilities of a quantitative study of selective reflection were explored. In particular the Hg 2537 Å and the Cd 2288 Å reflections were studied quantitatively over a wide range of vapor pressures. The variation of the reflected intensity with frequency could be interpreted in a general way in terms of the classical anomalous dispersion equations. There remain however certain features of the experimental results which do not appear to be explainable in terms of existing theories.

### Experimental Procedure

Since selective reflection is not confined to the resonance frequency alone, the selective reflections were detected and studied by using incident light of continuous spectral distribution and analyzing the reflected light spectrographically. The region of anomalous reflection at Hg 2537 Å is very narrow for vapor pressures up to a few atmospheres, so that it was necessary to use a spectrograph of high dispersion. At Cd 2288 Å the region of anomalous reflection is many times broader and a low dispersion spectrograph could be used.

A reflection cell with a window of good optical quality was necessary to obtain sufficient intensity for the study of the mercury reflection at high dispersion. The cell used was originally a Hilger absorption cell of fused quartz, 1.4 cm. in internal diameter and 4 cm. long, with contacted plane windows. The outer surface of one window was ground and polished at an angle of 1° with the inner surface to give an angular separation of the reflections from the two surfaces. Mercury was distilled under vacuum into a small side tube, and the cell was then sealed off. A nichrome oven with a plane window of fused quartz was used to heat the cell, which was supported by a solid quartz rod fused to the cell and extending through the wall of the oven to a clamp outside. The oven was differentially wound so that the front window of the reflection cell could be maintained 20° to 30°C. hotter than the side tube to prevent condensation of mercury vapor on the window. Thermocouples were attached to the front of the cell and to the side tube containing the liquid mercury.

A low voltage hydrogen arc of the type described by Allen and Franklin (1) furnished the ultraviolet continuum. A condensing lens of quartz with the small luminous portion of the hydrogen lamp at its focal point gave a parallel beam falling on the quartz-mercury vapor surface at almost normal incidence (Fig. 1a). The reflected beam was focused on the slit of the spectrograph by the same lens. A double-prism quartz spectrograph with Littrow mounting gave a linear dispersion of 1.7 Å per mm. in the region of 2537 Å. With a spectral slit width of 1 cm.<sup>-1</sup> the reflection spectrum could be photographed in one hour on Ilford Special Lantern plates.

Several reflection cells were made up for use with cadmium. These were constructed by fusing a prismatic window with an angle of 5° to a fused quartz tube, 1.2 cm. in internal diameter. Some distortion of the windows was introduced in the fusion process with a consequent loss in intensity in the reflected

image of the lamp. Cadmium was distilled under vacuum into the cell which was then sealed off. A differentially wound platinum oven, designed for use up to  $1400^{\circ}\text{C}.$ , was used to heat the cell. A condensing lens placed between the hydrogen arc and the cell gave a converging beam reflected from the cell and focused on the slit of the spectrograph (Fig. 1*b*). A single-prism quartz spectrograph with an  $f/4.5$  camera lens and a linear dispersion of  $20\text{\AA}$  per mm. in the region of  $2288\text{\AA}$  was used. With Ilford Q.1. plates exposure times of 30 min. were required for a spectral slit width of  $11\text{ cm.}^{-1}$ .

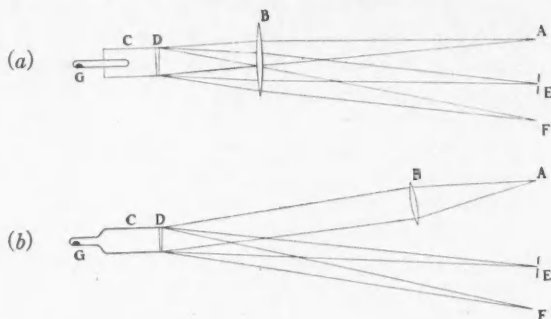


FIG. 1. Optical arrangements used for selective reflection (a) from mercury vapor, (b) from cadmium vapor. A—light source; B—lens; C—reflection cell; D—prismatic window; E—slit of spectrograph; F—image reflected from front surface of the window; G—metal.

The photographic plates were calibrated for intensity measurements by photographing the continuous spectrum of the hydrogen arc with a stepped slit substituted for the usual slit of the spectrograph. The calibration spectra were photographed with the same exposure times as the reflection spectra. A Leeds and Northrup microphotometer was used to measure the densities of the spectrograms.

The spectrum of a cold mercury arc was photographed in juxtaposition with each spectrum of the selective reflection of mercury. When the two spectra were microphotometered with fiducial marks superposed the position of the sharp mercury line at  $2534.8\text{\AA}$  could be transposed to the reflection spectrum. It was found from a series of plates taken at the same mercury vapor pressure that the calibration reproduced to  $0.025\text{\AA}$ . The cadmium reflection spectra were calibrated in a similar manner with a nickel arc comparison spectrum.

Vapor pressures for mercury were obtained from the formula given by Menzies (10), while those for cadmium were taken from the review of Ditchburn and Gilmour (3). Vapor pressures for cadmium have been measured only up to  $840^{\circ}\text{C}.$ , so that the higher pressures which were obtained by extrapolation cannot be expected to be accurate. The number of atoms per cubic centimeter,  $N$ , was found from the formula,  $N = p/kT$ , where  $T$  is the temperature in degrees Kelvin at the window of the cell. The pressure,  $p$ , of the vapor in the cell was taken to be the same as the vapor pressure of the liquid in the side tube.

This procedure is justified according to Weber (15), when the mean free path of the atoms is much smaller than the diameter of the connecting tube.

### Selective Reflection from Cadmium Vapor

Although earlier investigations on selective reflection have been confined to the mercury resonance line  $2537\text{ \AA}$  ( $6^1S_0-6^3P_1$ ), the effect should be observable for any strong absorption line, and the intensity of reflection should show a relationship to the absorption strength of the line. The second mercury resonance line at  $1849\text{ \AA}$  ( $6^1S_0-6^1P_1$ ) has a much greater absorption strength than the intercombination line  $2537\text{ \AA}$ , but it lies in a wave-length region inconvenient for observation. However, the corresponding resonance lines of cadmium lie at longer wave lengths and can be readily investigated.

The hydrogen continuum reflected from the cadmium cell was examined for cell temperatures up to  $1125^\circ\text{C}$ . Selective reflection of the resonance line  $2288\text{ \AA}$  ( $5^1S_0-5^1P_1$ ) was first observed at a vapor pressure of 4 mm. as a faint sharp line just discernible on the continuous background of the spectrum. With increasing vapor pressure the region of anomalous reflection broadened and assumed the characteristic appearance of selective reflection, with a less than normal intensity on the long wave-length side and a greater than normal intensity on the short wave-length side (Fig. 2). At the higher pressures (5 to 20 atm.) the region of the anomalous reflection was several hundred Angstroms wide compared to a maximum width of about  $10\text{ \AA}$  for the Hg  $2537\text{ \AA}$  reflection at 8 atm. The cadmium resonance line at  $3261\text{ \AA}$  ( $5^1S_0-5^3P_1$ ) was first detected in the reflected spectrum at  $1125^\circ\text{C}$ ., the highest temperature reached. This temperature corresponds to a vapor pressure of 15,000 mm. as obtained by extrapolation of the vapor pressure equation. With a similar experimental arrangement the selective reflection of the Hg  $2537\text{ \AA}$  line was detected first at a vapor pressure of 170 mm.

TABLE I  
RELATION BETWEEN  $f$ -VALUE AND  $N$  FOR FIRST APPEARANCE  
OF SELECTIVE REFLECTION

Resonance line	Oscillator strength, $f$	No. of atoms per cc., $N$ , ( $\times 10^{-17}$ )	$Nf$ , ( $\times 10^{-17}$ )
Cd 2288Å	1.19	0.5	0.6
Cd 3261Å	$1.9 \times 10^{-3}$	1000	1.9
Hg 2537Å	$2.68 \times 10^{-2}$	28.5	0.76

The conditions for first appearance in reflection of the two cadmium lines and the mercury line are given in Table I. The  $f$ -values or oscillator strengths of the absorption lines, obtained from the summary of Mitchell and Zemansky (11), are given in the second column. The value of the product,  $Nf$ , is found to be approximately the same for the two lines for which the data are most

reliable, and is not greatly different for the other line. This gives an empirical rule which might be used to predict the vapor density of the first appearance of selective reflection for any absorption line whose  $f$ -value is known.

### Contour of the Mercury Reflection at 2537Å

#### EXPERIMENTAL RESULTS

Reduction of photographic densities to intensities over the whole contour of the reflection was carried out for a series of plates at mercury vapor pressures of  $\frac{1}{2}$ , 1, 2, 4, and 8 atm. The intensity contours of the selective reflection plotted against the distance in  $\text{cm}^{-1}$  from  $\nu_0$ , the frequency of the resonance line, are shown in Fig. 3. Relative intensities are given as "% reflected intensity" since

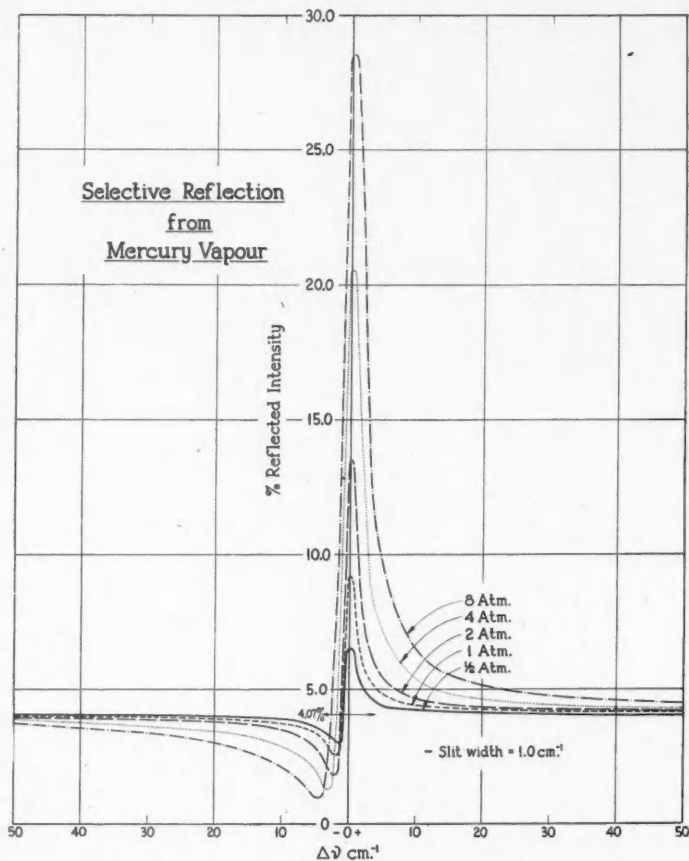


FIG. 3.

PLATE I

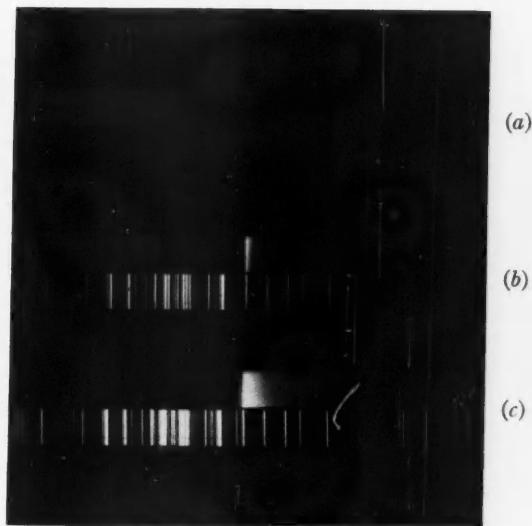
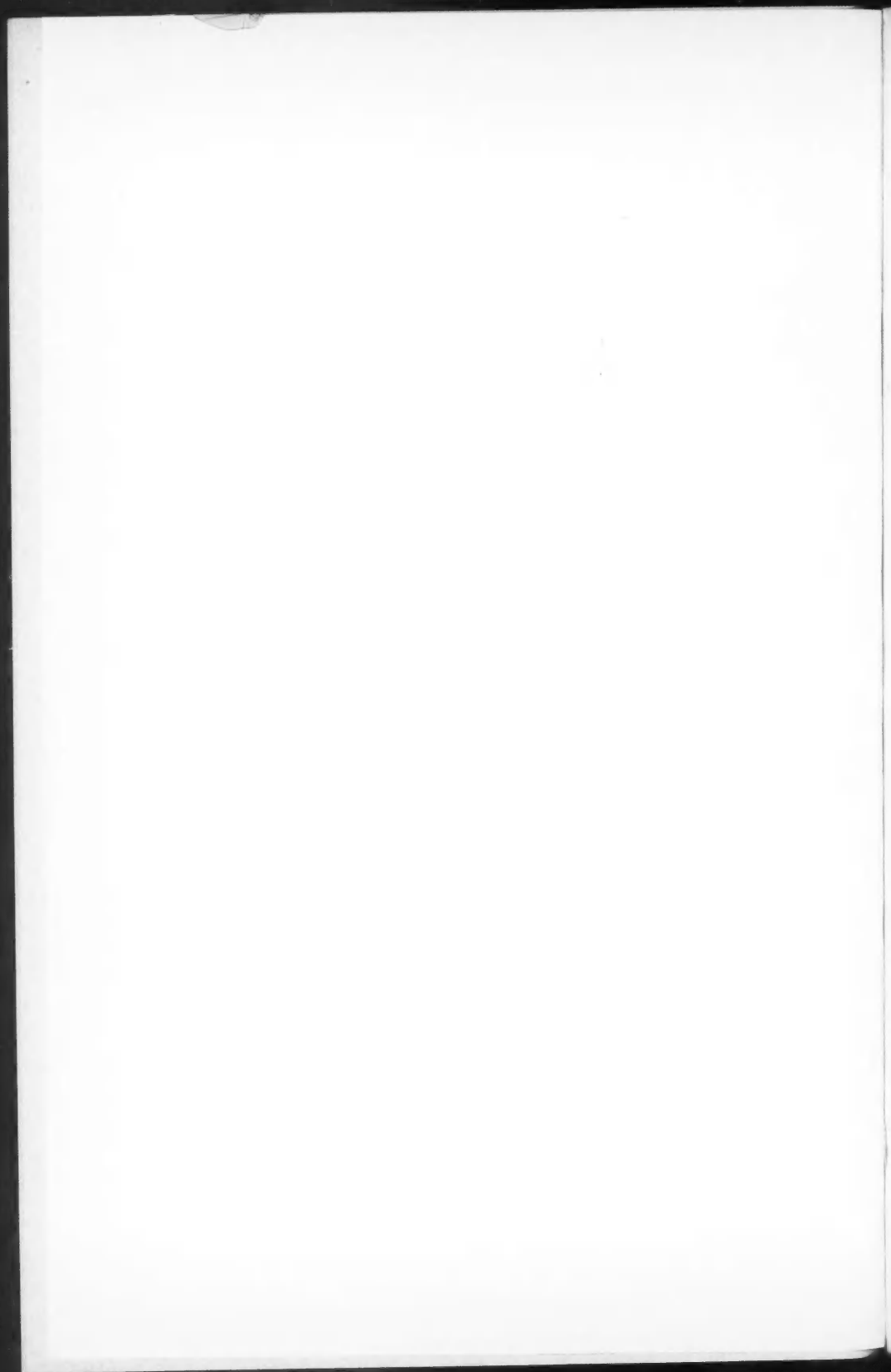


FIG. 2. Selective reflection in the neighborhood of Cd 2288 Å for vapor pressures of (a) 34 mm., (b) 2 atm., (c) 14.7 atm. Nickel arc comparison spectrum. Wave-length region 2200 to 2400 Å.





this quantity is used in the interpretation. The "% reflected intensities" are based on a calculated value for the "normal reflection" outside of the region of anomalous reflection, where the refractive index of mercury vapor at the pressures used here can be taken as unity according to the dispersion formula given by Wolfsohn (19). The normal intensity of reflection was calculated from the Fresnel reflection formula for normal incidence to be 4.06% at 300°C. and 4.08% at 500°C., using refractive index measurements for fused quartz by Ramachandran (12).

#### INTERPRETATION OF THE RESULTS

The main features of the contour of the selective reflection can be explained qualitatively, as Wood pointed out, by the anomalous behavior of the refractive index of the vapor at frequencies near the resonance frequency. The most obvious approach to the interpretation of the experimental results is therefore through the classical theory of reflection from an absorbing medium. The refractive index,  $n$ , and absorption coefficient,  $k$ , are given as functions of the frequency,  $\nu$ , by the dispersion equations:

$$n^2 - k^2 = n_0^2 + \frac{1}{2\pi m\nu_0} \frac{Nfe^2(\nu_0 - \nu)}{(\nu_0 - \nu)^2 + (\gamma/4\pi)^2} \quad (1)$$

$$2nk = \frac{\gamma}{8\pi^2 m\nu_0} \frac{Nfe^2}{(\nu_0 - \nu)^2 + (\gamma/4\pi)^2}, \quad (2)$$

in which  $\nu_0$  is the resonance frequency,  $n_0$  is the hypothetical refractive index if no anomalous dispersion were present,  $\gamma$  is the damping constant,  $f$  is the classical oscillator strength (related to the quantum mechanical transition probability), and the other symbols have their usual meanings.

The reflecting power of an absorbing medium for light at normal incidence is given in terms of  $n$  and  $k$  by the Fresnel formula:

$$R = \frac{(n - n')^2 + k^2}{(n + n')^2 + k^2}, \quad (3)$$

where  $n'$  is the refractive index of the bounding medium (fused quartz in the present case).

#### Calculation of the $f$ -value from the Wings of the Contour

The absorption coefficient,  $k$ , decreases rapidly with increasing frequency displacement,  $\Delta\nu = \nu - \nu_0$ , from the resonance frequency. Hence, in the wings of the contour the refractive index of the vapor can be calculated from the reflected intensity by means of Equation (3) with  $k = 0$ . Also, when  $k$  is negligible the dispersion equations (1) and (2) reduce to the form:

$$n^2 - 1 = - \frac{Nfe^2}{2\pi m\nu_0} \frac{1}{\Delta\nu}, \quad (4)$$

in which  $n_0$  has been put equal to unity. A plot of  $1/(n^2-1)$  against  $\Delta v$  should therefore give a straight line in the region in which  $k$  is negligible, and the slope of the line can be used to calculate the  $f$ -value of the transition. Fig. 4 is an example of such a plot for mercury vapor at 8 atm. pressure. The fact that the best straight line does not pass through the origin indicates a change of  $v_0$  with pressure. The  $f$ -values obtained for various vapor pressures by this method ranged from 0.023 to 0.027, in fair agreement with values obtained by other

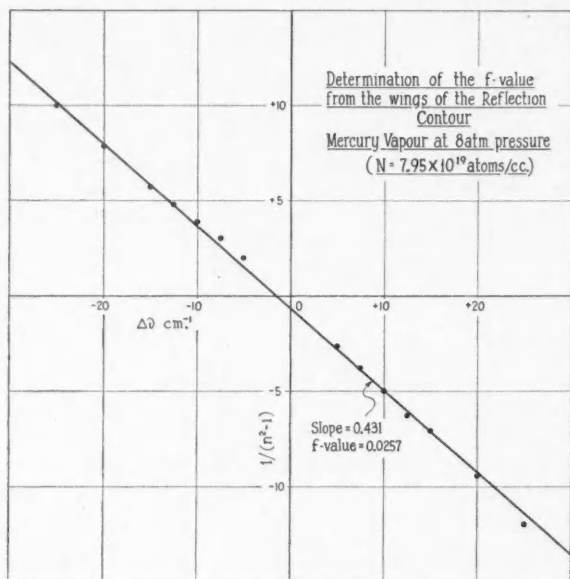


FIG. 4.

methods (11). However, since the calculated values of  $n$  are very sensitive to small errors in the measured reflectivity in the wings of the pattern, this method is not the most accurate way of determining the  $f$ -value from the reflection contour.

#### *Fitting of a Theoretical Curve to the Complete Reflection Contour*

The explanation of selective reflection on the basis of anomalous dispersion can be tested quantitatively by attempting to fit the experimental contour by a variation of the parameters  $f$  and  $\gamma$  in Equations (1), (2), and (3). The procedure used in fitting a theoretical curve to the experimental contour was as follows: The dispersion equations are written in the form

$$n^2 - k^2 = n_0^2 - \frac{Mx}{1 + x^2} = A \quad (5)$$

$$2nk = \frac{M}{1+x^2} = B, \quad (6)$$

where  $x = \frac{4\pi}{\gamma} \Delta\nu$  and  $M = \frac{2Nfe^2}{m\gamma\nu_0}$ . (7)

The solutions for  $n$  and  $k$  are

$$n^2 = \frac{\sqrt{A^2 + B^2} + A}{2}, \quad k^2 = \frac{\sqrt{A^2 + B^2} - A}{2}, \quad (8)$$

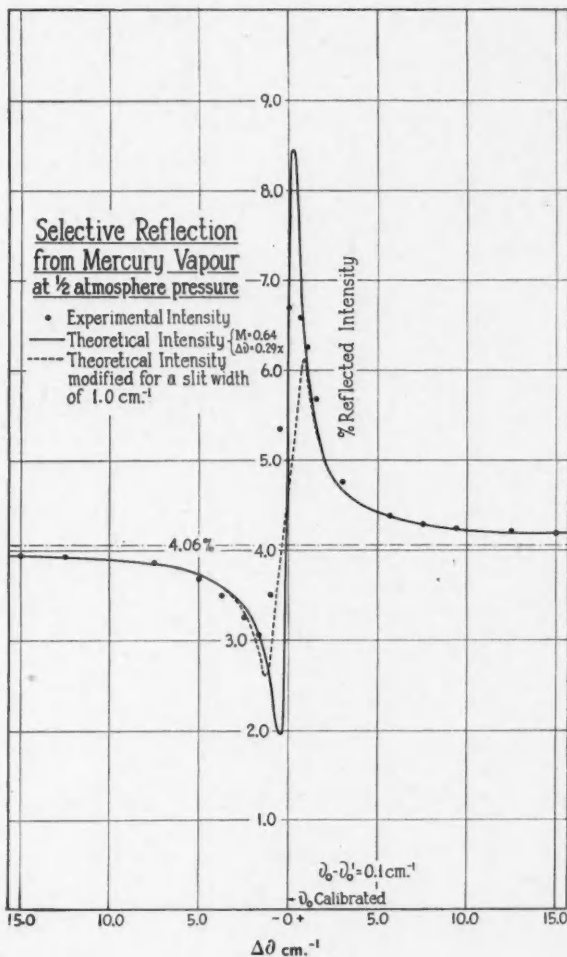


FIG. 5

which can be used to obtain  $R$  from Equation (3). It was found convenient to obtain the fit by varying the quantities  $M$  and  $4\pi/\gamma$  rather than  $f$  and  $\gamma$ . Since the spread of the theoretical pattern along the  $\Delta\nu$  axis is determined by  $4\pi/\gamma$  and along the  $R$  axis by  $M$ , the two quantities can be varied independently to obtain

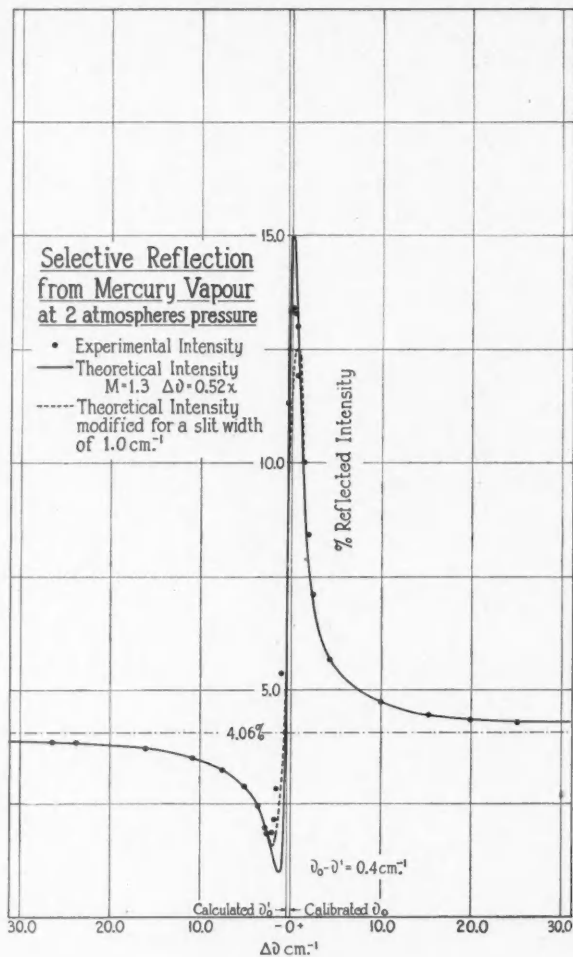


FIG. 6.

the fit. The experimental contour was plotted against  $\log \Delta\nu$  and the theoretical contour for a given  $M$  against  $\log x$  on separate sheets of graph paper. A test for fit should have been possible by shifting the theoretical and experimental curves relative to one another along the abscissa axis, since this corresponds to

a variation of  $4\pi/\gamma$ . However, the change in  $\nu_0$  with pressure adds a complication, the shape of the experimental curve being extremely sensitive to the choice of zero of the  $\Delta\nu$  scale. A family of experimental curves was therefore plotted corresponding to shifts in the resonance frequency from 0 to  $1.5 \text{ cm}^{-1}$

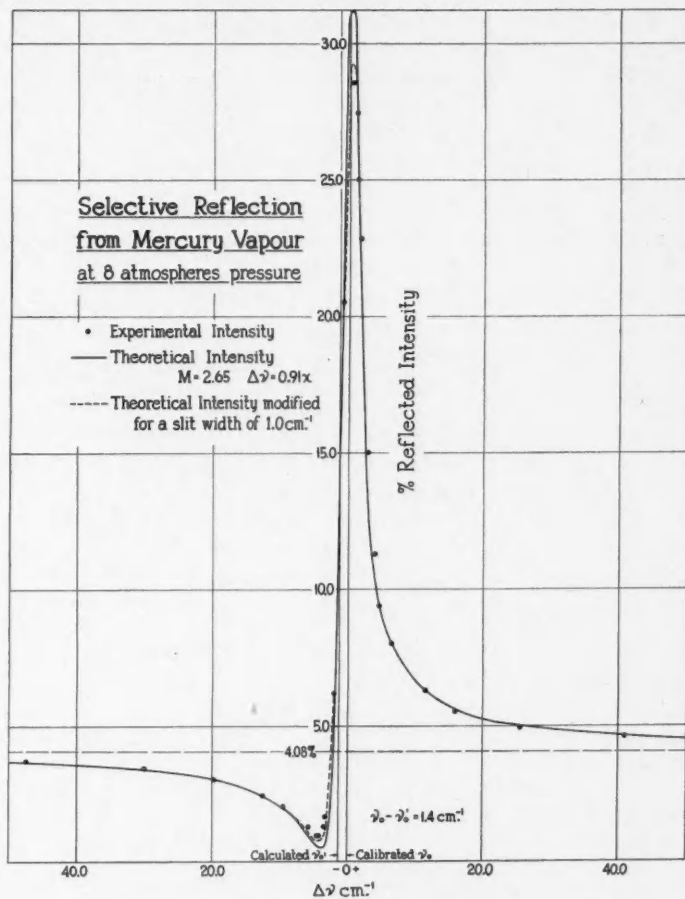


FIG. 7.

in steps of  $0.1 \text{ cm}^{-1}$  from  $\nu_0$ , the calibrated frequency of the resonance line. For the correct choice of  $M$  it was then possible to fit a theoretical contour ( $R$  against  $\log x$ ) to one of the family of experimental curves ( $R$  against  $\log \Delta\nu$ ).

Examples of the results obtained by this procedure are shown in Figs. 5, 6, and 7. In each case the agreement was improved at the maximum and minimum

when the theoretical curve was modified for the finite slit width of the spectrograph. The agreement was excellent for the higher vapor pressures but became progressively worse in going to lower pressures. This may be due in part to the larger experimental error at lower pressures where the reflection pattern is very narrow. However, the deviation is always such that the experimental intensities are higher than the theoretical intensities in the vicinity of  $\nu_0$ . This could mean that there is an additional intensity around  $\nu_0$  which is not accounted for in the interpretation of the reflection contour based on the anomalous dispersion equations. This residual intensity is much greater in the case of cadmium at low pressures and will therefore be discussed at greater length later.

*Derived Values of  $f$ ,  $\gamma$  and  $\delta\nu_0$*

The fitting of a theoretical reflection curve to the experimental contour for a given vapor pressure yields values of  $f$ ,  $\gamma$  and  $\delta\nu_0 = \nu_0 - \nu_0'$ , where  $\nu_0$  and  $\nu_0'$  are respectively the calibrated and calculated values of the resonance frequency. The results for five vapor pressures are given in Table II.

TABLE II  
VALUES OF  $f$ ,  $\gamma$ ,  $\delta\nu_0$  DERIVED FROM THE REFLECTION CONTOUR OF Hg 2537 Å

Vapor pressure, atm.	No. of atoms per cc., $N$ , ( $\times 10^{-18}$ )	Oscillator strength, $f$	Damping constant, sec. <sup>-1</sup> $\gamma (\times 10^{-11})$	$\gamma/\sqrt{N}$ , ( $\times 10^{-1}$ )	Shift of $\nu_0$ , cm. <sup>-1</sup> $\delta\nu_0$
0.5	6.03	0.0269	1.09	4.40	-0.1
1.0	11.1	0.0269	1.42	4.23	-0.2
2.0	22.2	0.0267	1.96	4.14	-0.4
4.0	44.4	0.0263	2.64	3.94	-0.8
8.0	79.5	0.0265	3.43	3.81	-1.4

The  $f$ -value remains constant with increasing vapor density, and the mean value,  $f = 0.0267 \pm 0.0003$ , is in good agreement with values obtained by other methods. These have been summarized by Mitchell and Zemansky (11), who conclude that the most reliable of the older values is 0.0268 found by Garrett (6) from the decay of electrically excited resonance radiation.

Selective reflection thus provides a new means of measuring the  $f$ -values of strong absorption lines. The method seems to be comparable in accuracy with the best of the older methods and could undoubtedly be improved by more accurate intensity measurements.

The variation of the damping constant,  $\gamma$ , with vapor pressure is of special interest. If the  $\gamma$  measured in this experiment were the same as the damping constant due to collision broadening and given by the half width of the absorption line, one would expect a direct proportionality between  $\gamma$  and  $N$ . This

relation has been derived theoretically by Weisskopf (18), Margenau (9), Fursow and Wlassow (5) and others. However, the  $\gamma$  in selective reflection varies more closely as  $\sqrt{N}$  as shown by the fifth column in Table II. This result is confirmed by an empirical areal law discussed below and also by the results on cadmium. Thus the damping present in selective reflection seems to differ fundamentally from collision damping in the broadening of spectral lines.

The shifts in the resonance frequency,  $\delta\nu_0$ , show a direct proportionality with  $N$ . However, since the frequency calibrations of the spectrograms were reproducible only to about  $0.2 \text{ cm}^{-1}$ , the values of  $\delta\nu_0$  can have a large percentage error. Weisskopf (17) has shown that the coupling of atoms in the Lorentz-Lorenz sense should cause  $\nu_0$  to move to lower frequencies at higher densities and the displacement of  $\nu_0$  should be proportional to  $N$ . The frequency shift is given by

$$\delta\nu_0 \text{ (in cm}^{-1}\text{)} = - \frac{e^2 f N}{6\pi c^2 m \nu_0} \quad (9)$$

The reality of the effect cannot be checked in absorption experiments because the small shift is masked completely by the resonance broadening of the absorption line. Although the shifts calculated from Formula (9) are only a little greater than half of those observed, it is considered that  $\delta\nu_0$  can be interpreted as a shift due to coupling. The corresponding change in  $\gamma$  due to coupling, as derived by Weisskopf, is much too small to be observable here.

#### *An Empirical Areal Law for Selective Reflection*

It is well known that the integral of the absorption coefficient of a spectral line is proportional to  $N$  and is independent of broadening processes. A similar relationship was found to hold for the contour of the selective reflection. When the area between the contour of the reflection and the straight line corresponding to the normal reflected intensity was plotted against  $N$  a straight line was obtained (Fig. 8). The existence of such an empirical law implies a certain relationship between  $\gamma$  and  $N$ , since the  $f$ -value appears to be independent of  $N$ . An attempt was therefore made to integrate the metallic reflection equation to determine the variation of  $\gamma$  with  $N$ , but this was not found to be possible. However, a numerical evaluation of the integral

$$\int_{-\infty}^{\infty} \left| \frac{(n - 1.506)^2 + k^2}{(n + 1.506)^2 + k^2} - 0.0407 \right| d\nu$$

was carried out\* for two widely separated vapor pressures. The variation of  $n$  and  $k$  with  $\nu$  was calculated by assuming  $f = 0.0267$  and  $\gamma = 40\sqrt{N}$ , these values representing an average of the experimental results. The computation confirmed the empirical areal law. The observed proportionality of the area under the reflection contour to  $N$  is therefore consistent with a variation of  $\gamma$  as  $\sqrt{N}$ , as indicated in the results obtained in fitting a theoretical curve to

\*The authors are indebted to the Computation Centre, University of Toronto, for assistance in this calculation.

the reflection contour (Table II). Indeed the areal law can be looked upon as the more convincing proof of the relation  $\gamma \propto N$  since it is more direct.

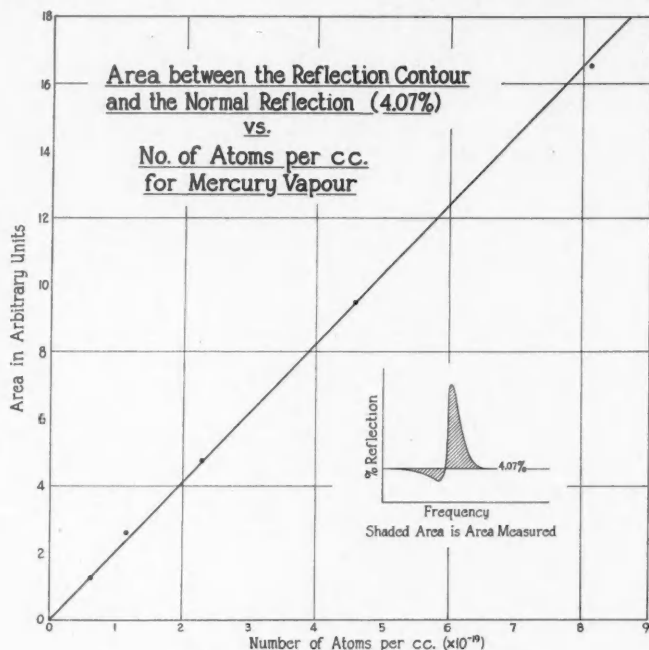


FIG. 8.

### Contour of the Cadmium Reflection at 2288Å

Examples of the reduced reflection contours obtained for the Cd 2288Å line are shown in Fig. 9. The large change in background density over the region of the selective reflection made the reduction to "% reflected intensity" more difficult at the higher vapor densities. From the shape of the background density at low pressures empirical rules were established with which the reduction was effected. The "normal reflected intensity" of 4.27%, calculated from the refractive index of fused quartz at 2288Å assuming a refractive index of unity for the vapor, was used for the whole range of the reflection. The error thus introduced was probably small compared to the error due to the uncertain background density at high vapor pressures.

Theoretical contours were fitted to several of the experimental curves by the method previously outlined. Since the contours for the lower vapor pressures were distorted by the low purity of spectrum obtained with the small spectrograph, only the results for pressures higher than 350 mm. were treated quantitatively. Examples of the results obtained are given in Figs. 10, 11, and 12.



In the medium pressure range (1–2 atm.) the experimental curves could be accurately reproduced, but at lower and higher pressures only the outer portions of the pattern could be fitted.

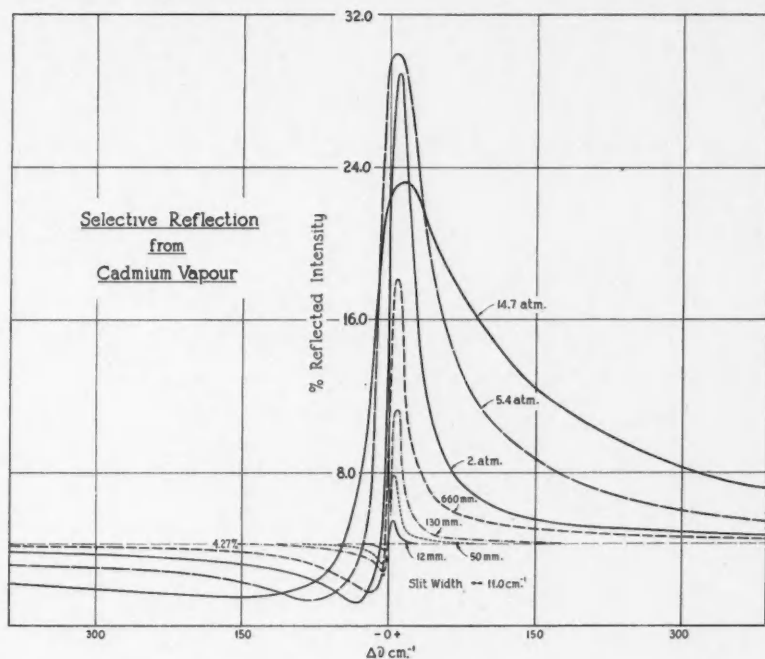


FIG 9.

TABLE III

VALUES OF  $f$  AND  $\gamma$  DERIVED FROM THE REFLECTION CONTOUR OF Cd 2288Å

Vapor pressure, atm.	No. of atoms per cc., $N$ , ( $\times 10^{-18}$ )	Oscillator strength, $f$	Damping constant, sec. <sup>-1</sup> $\gamma (\times 10^{-11})$	$\gamma/\sqrt{N}$ ( $\times 10^{-2}$ )
0.17	1.36	1.53	11.0	9.4
0.46	3.32	1.38	16.0	8.8
0.87	5.96	1.36	21.0	8.6
2.0	12.4	1.38	30.0	8.6
5.4	31.1	1.36	48.0	8.7
14.7	77.7	1.38	77.0	8.8

The values of  $f$  and  $\gamma$  obtained from the fittings are given in Table III. The  $f$ -value remained constant except at the lowest pressure where the experimental error was rather large. The average  $f$ -value obtained, 1.40, yields a mean life-time of  $1.7 \times 10^{-9}$  sec. for the  $5^1P_1$  state of cadmium. The value  $2.0 \times 10^{-9}$  sec.,

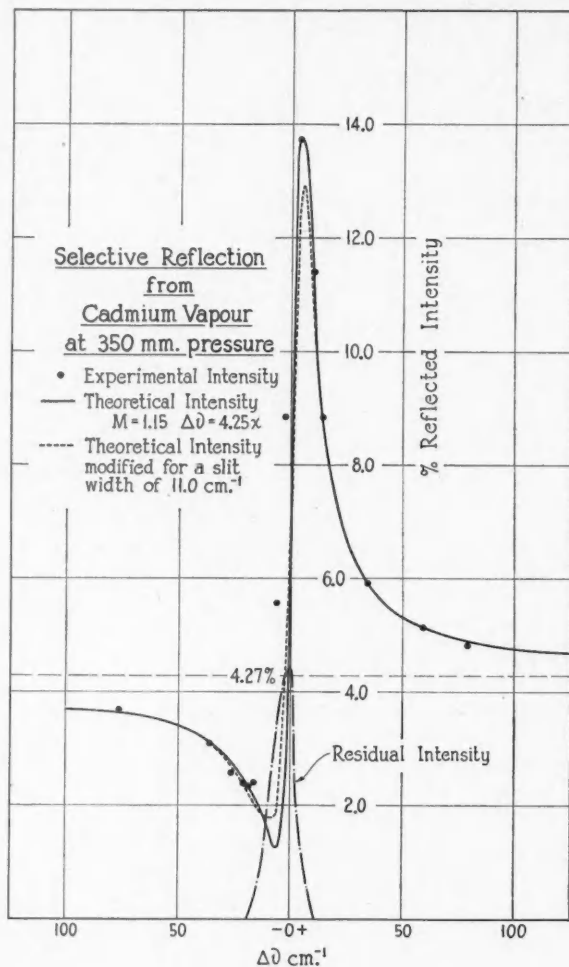


FIG. 10.

was obtained by Kuhn (8) from magnetorotation at the edges of the resonance line, and also by Zemansky (21) from total absorption of the line in cadmium vapor at low pressures. The  $f$ -value obtained from selective reflection

is in fair agreement with this value and is probably rather more accurate. From Column 5 of the table it is seen that the damping constant,  $\gamma$ , is directly proportional to  $\sqrt{N}$  as it was with mercury. The value of  $\gamma$  is about 20 times as great for Cd 2288 Å as for Hg 2537 Å at the same value of  $N$ . The large damping

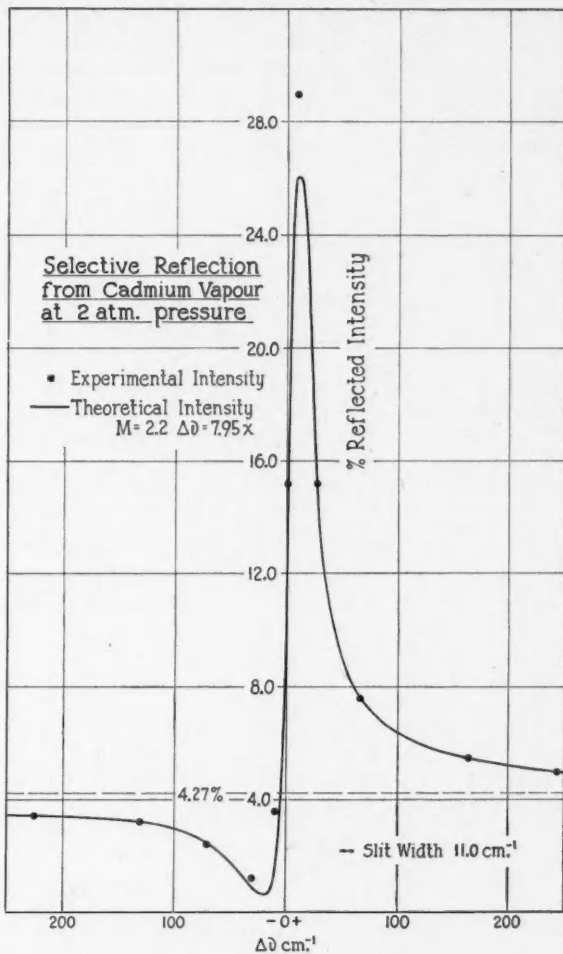


FIG. 11.

constant is chiefly responsible for the great extent of the selective reflection of cadmium, as may be seen from Equations (7).

No shift in  $\nu_0$  was required to obtain a fit between theoretical and experi-

mental contours as was necessary for mercury. A shift of the size predicted by Weisskopf's formula, Equation (9), would have had little effect on the fitting.

The area enclosed by the reflection contour and the straight line representing normal reflected intensity is plotted against  $N$  in Fig. 13. As in the case of mercury the area is directly proportional to  $N$  over a large range of vapor densities. This indicates, as before, the validity of the relationship  $\gamma \propto \sqrt{N}$ . At the highest pressures where it was impossible to determine the full extent of the selective reflection, the measured areas are too small since they do not include the whole pattern. Hence, it is uncertain whether the deviation from the straight line at the higher densities is real.

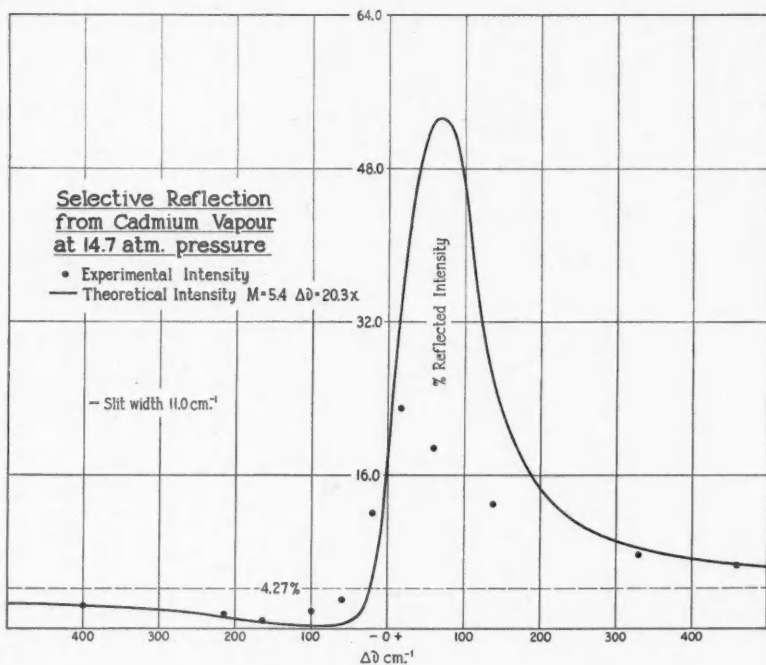


FIG. 12.

For the lower pressures, when the theoretical curve giving the best fit in the wings was subtracted from the experimental curve, a residual intensity was obtained forming a "line" approximately symmetrical about  $\nu_0$  with a half width of about 12 cm.<sup>-1</sup> (Fig. 10). At pressures greater than 1 atm. the residual intensity is scarcely detectable. Some indication of the effect is present in the mercury reflection contours but is of the order of magnitude of the experimental error.

The deviation from the theoretical curve for high vapor pressures of cadmium is of an entirely different nature (Fig. 12). The region of the deviation is much greater and neither the maximum nor the minimum is as pronounced as is required by the theory. No variation of  $f$  and  $\gamma$  can lead to a good fitting of the experimental contour. With increasing pressure above 8 atm. the maximum of the curve begins to fall instead of continuing to rise as the theory predicts.

The results of the present investigation lead to the conclusion that the general features of selective reflection conform to the classical theory of re-

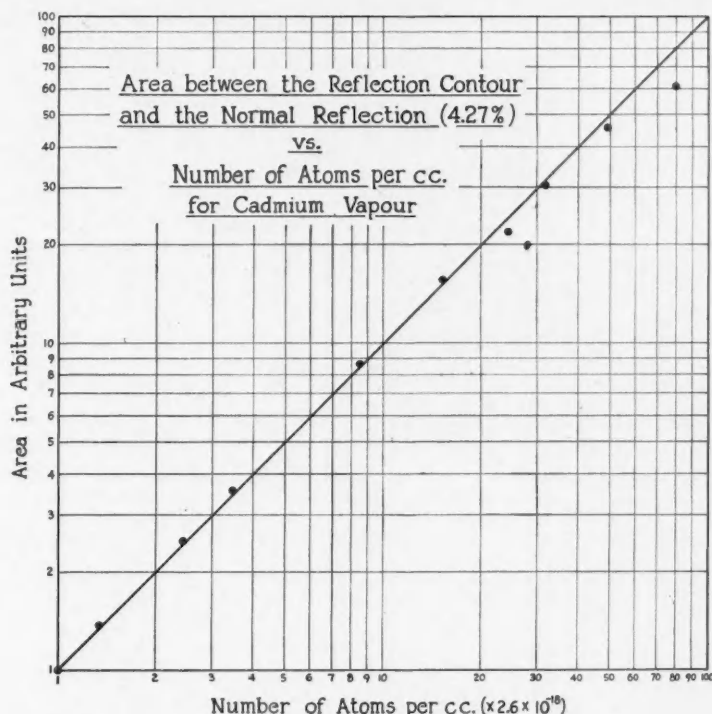


FIG. 13.

flection from an absorbing medium. From the viewpoint of the quantum theory selective reflection must be a coherent scattering process rather than an absorption and re-emission with a finite lifetime of the excited state. The relation  $\gamma \propto \sqrt{N}$  confirms the view that a simple absorption process is not involved although no theoretical explanation of the relationship presents itself. For the Cd 2288 Å line, which has much larger  $f$  and  $\gamma$  values than Hg 2537 Å, deviations from the anomalous dispersion theory are more marked. The residual

intensity observed at lower vapor pressures may be a second type of selective reflection arising from resonance fluorescence in a definite phase relationship with the incident light as deduced by Weisskopf (16). It should be noted that since there are no metastable states near the  $5^1P_1$  state of cadmium the quenching of the resonance fluorescence with increasing vapor pressure should be much less than for Hg 2537 Å. The reason for the marked deviation of the reflection contour from theory at the higher vapor densities is not immediately apparent. A tentative explanation is that the anomalous dispersion equations with a unique value of the resonance frequency,  $\nu_0$ , are no longer applicable when strong coupling exists between the atoms.

### References

1. ALLEN, A. J. and FRANKLIN, R. G. J. Optical Soc. Am. 29: 453. 1939.
2. BURTON, C. V. Phil. Mag. 29: 30. 1915.
3. DITCHBURN, R. W. and GILMOUR, J. C. Revs. Modern Phys. 13: 310. 1941.
4. FERMI, E. R. Atti reale acad. nazl. Lincei, 33: 90. 1924.
5. FURSSOW, V. and WLOSSOW, A. Physik. Z. Sowjetunion, 10: 378. 1936.
6. GARRETT, P. H. Phys. Rev. 40: 779. 1932.
7. HANSEN, J. M. and WEBB, H. W. Phys. Rev. 72: 332. 1947.
8. KUHN, W. Kgl. Danske Videnskab. Selskab, Mat.-fys. Medd. 7: Nr. 12. 1926.
9. MARGENAU, H. Revs. Modern Phys. 22: 348. 1936.
10. MENZIES, A. W. C. Z. physik. Chem. 129: 90. 1927.
11. MITCHELL, A. and ZEMANSKY, M. Resonance radiation and excited atoms, p. 148. Cambridge: The University Press. 1934.
12. RAMACHANDRAN, G. N. Proc. Indian Acad. Sci. A, 25: 266. 1947.
13. RUMP, W. Z. Physik, 29: 196. 1924.
14. SCHNETTLER, O. Z. Physik, 65: 55. 1930.
15. WEBER, S. Commun. Kamerlingh Onnes Lab. Univ. Leiden, 223b: 11. 1933.
16. WEISSKOPF, V. Ann. Physik, 9: 23. 1931.
17. WEISSKOPF, V. Physik. Z. 34: 1. 1933.
18. WEISSKOPF, V. Z. Physik, 75: 287. 1935.
19. WOLFSOHN, G. Z. Physik, 63: 634. 1930.
20. WOOD, R. W. Researches in physical optics. Vol. II. Columbia Univ. Press. 1919.
21. ZEMANSKY, M. Z. Physik, 72: 587. 1931.

## INTEGRATOR-EXPANDER CIRCUITS FOR THE CONTROL OF THE MAXIMUM X-RAY ENERGY FROM THE BETATRON<sup>1</sup>

L. KATZ, A. G. McNAMARA,<sup>2</sup> P. A. FORSYTH, R. N. H. HASLAM,  
AND H. E. JOHNS

### Abstract

The electronic circuits known as an integrator-expander were constructed for the accurate control of the X-ray energy of the University of Saskatchewan betatron. The over-all design and operation of the circuits are discussed. The design of the energy bias control, amplifier, and trigger portions of the circuit is original, and these are described in some detail.

### Introduction

The betatron obtained by the University of Saskatchewan in 1948 was the 22 Mev. Allis-Chalmers machine designed primarily for industrial radiography. No accurate means of energy control is incorporated in this make of betatron. For nuclear research purposes the maximum X-ray energy must be continuously variable over a wide range, and be quite accurately known at all settings.

The so-called integrator method (1, 2, 5) of controlling the maximum X-ray energy from the betatron has been developed at the University of Illinois. The basic principles used by us are the same as those worked out at Illinois. The integrator built at Saskatchewan makes use of circuits which the authors feel lead to particularly stable operation. A signal (voltage) is obtained which is proportional to the instantaneous energy of the accelerated electrons so that expansion of the orbit may be made to coincide with a predetermined electron energy and therefore maximum gamma ray energy.

This method is based on the working principle of the induction electron accelerator as expressed by one of Maxwell's equations,

$$\oint_1 \vec{E} \cdot d\vec{l} = - \iint \frac{\partial \vec{B}}{\partial t} \cdot d\vec{s} .$$

From this it may be shown that the instantaneous energy is proportional to the time integral of the rate of change of flux through the orbit; that is, to the total flux linking the orbit. Since the flux linking the orbit is proportional to the flux linking the main coils, the voltage across the coils will be proportional to the rate of change of flux and, when integrated, will represent the instantaneous energy.

<sup>1</sup> Manuscript received August 19, 1949.

Contribution from the Department of Physics, University of Saskatchewan, Saskatoon, Saskatchewan.

<sup>2</sup> Holder of a Studentship under the National Research Council of Canada, 1948-49.

In the control circuit to be described here, any desired energy may be chosen by selecting a value on a calibrated variable bias control. When the signal voltage reaches this value, a trigger pulse is developed in the succeeding circuits which causes the electron orbit to be expanded with a minimum time delay.

As mentioned above, the over-all method of integration-expansion is that developed at the University of Illinois, the integrator stack and expander circuits being almost identical. The bias, amplifier, and trigger circuits we have designed ourselves with the object of obtaining maximum stability, dependability, and accuracy.

### The Integrator

The integrating network (2, 5) (see Fig. 1) consists of  $R = 10^6$  ohms (twenty 50,000 ohm, 100-w. resistors) and  $C = 0.1 \mu\text{f}$ . The voltage developed across

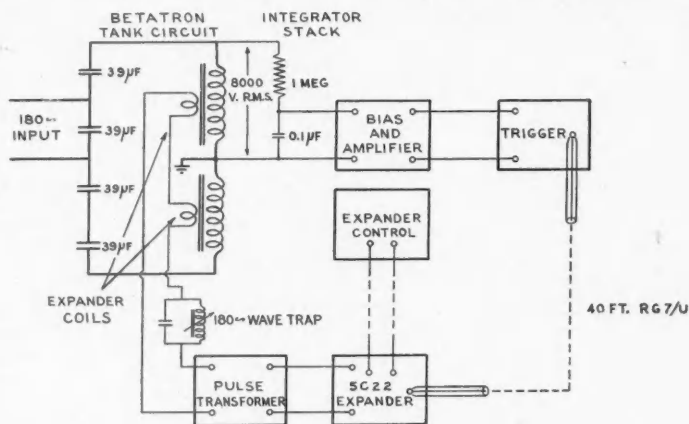


FIG. 1. Block diagram of integrator-expander.

the integrating capacitor is 86 v. at 23.1 Mev. Owing to the large impedance ratio of the integrator components, the 180 cycle magnet voltage is phase shifted almost 90 degrees, lacking only about 31 minutes of angle, and the phase shift is relatively independent of temperature or aging effects in the  $R$  and  $C$  values of the integrator. Actually the phase difference between the magnet current and the integrated voltage is even closer to zero degrees because of the effective resistance of the magnet coils. If the time constants of the coils and the integrator stack were equal, the signal voltage on the integrating capacitor would be exactly in phase with the magnet current. An estimation of the effective resistance of the magnet coils results in a calculated phase angle of 23 minutes. Thus the net phase advance of the integrator voltage ahead of the magnet current is of the order of 8 minutes of angle, which



corresponds to a time difference of about  $2.1 \mu\text{sec.}$  in the crossing of the zero axis. However, it is advantageous to retain this phase advance in order to compensate partially for time lags in the circuits that follow.

### The Bias Circuit and Integrator Amplifier

The first stage of the amplifier (Fig. 2) consists of a cathode follower used as an impedance transformer between the integrator stack and the grid of the following tube. To prevent grid-cathode voltage drift, the plate supply and heaters are stabilized.

The sum of the integrator signal voltage, the cathode follower grid bias, and the voltage on the tap of the Energy Control helipot, appear across the cathode resistor of the follower. Whenever this sum exceeds a fixed value of approximately 105 v., the 9006-diode unclamps and allows the grid of the first amplifier stage to be driven positive. The rate of rise of the input signal at the instant of unclamping is amplified by three stages to produce a pulse rising at least 10 v. per  $\mu\text{sec.}$  when the trigger point is near the axis of an 85 v. sine wave input. The first amplifier stage is a cathode-coupled stage for maximum stability; the following two stages are single-ended pulse amplifiers with their grid biases adjusted to obtain a sharply rising output. All heater voltages are stabilized and all tube voltages are VR-tube stabilized.

The 50,000-ohm Energy Control potentiometer is a 10 turn helipot with linearity of 0.1%. A stabilized reference voltage of approximately 105 v. is applied across this potentiometer. An important feature of the bias circuit is that the selected trigger point is independent of the characteristic curve of the clamping diode or nonlinearities of the cathode follower input-output characteristic. At the instant of unclamping, the cathode follower is always at the same point of its operating curve (approximately 105 v. across the cathode resistor), the diode current reduces to zero, and the current drawn from the reference supply returns to its "zero" value. Hence, assuming that no drifts occur in tube emission, etc., the linearity of the bias circuit depends only on the accuracy of the control potentiometer and the reference voltage.

### The Trigger Circuit

The square wave from the integrator amplifier is differentiated and the positive pulses used to trigger a cathode-coupled single-shot multivibrator which supplies the correct trigger pulse, through a cathode follower driver, to the expander. The pulse delivered by the amplifier has a rate of rise sufficient to reduce jitter in the multivibrator to about  $0.1 \mu\text{sec.}$  The plate load in the output side of the multivibrator is a 13 mh. air-core inductance. When the 75 ma. current flowing through this inductance is cut off, the inductance resonates with the stray capacity of the coil, the diode-clipper filament winding, and the wiring. The 6AL5 diode-clipper removes the oscillation after the first half-cycle. The resulting half sine wave pulse has 350 v. amplitude,  $7 \mu\text{sec.}$  duration,

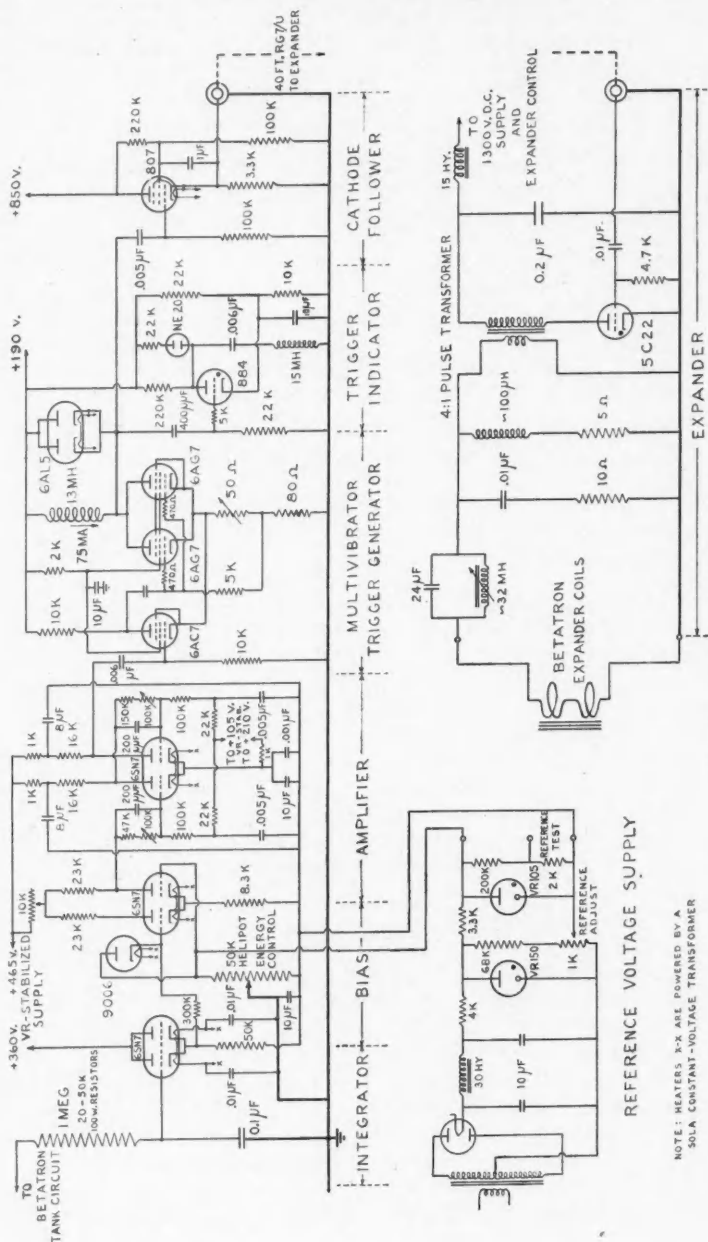


Fig. 2. Integrator-expander circuits.

NOTE: HEATERS ARE POWERED BY A  
SOLA CONSTANT-VOLTAGE TRANSFORMER

and a rate of rise of 250 v. per  $\mu\text{sec}$ . A cathode follower transforms this into a low impedance pulse to drive 40 ft. of coaxial cable and the grid of the 5C22 hydrogen thyatron.

### The Expander

The expander circuits are similar to the University of Illinois' with only a few changes of component values. When the 5C22 hydrogen thyatron is triggered, a 0.2  $\mu\text{f}$ . capacitor which is charged to approximately 3000 v. is discharged through a 4:1 pulse transformer. The load on the pulse transformer is mainly the inductance of the expander coils. The expander coils consist of one turn (10 strands of No. 18 wire) on each pole face, at a radius of 15.9 cm.

The voltage on the 0.2  $\mu\text{f}$ . storage capacitor is obtained from a resonant charging choke and a d-c. voltage supply capable of delivering 200 ma. of direct current at 1300 v. A variac in the primary of the high voltage transformer controls the output.

A wave trap, resonant at 180 cycles, blocks induced voltages in the expander coils from sending large currents through the secondary of the pulse transformer. The  $RL$ -combination (Fig. 2) across the secondary damps out any oscillations that may be set up in the wave trap by shock-excitation. High frequency oscillations superimposed on the expander pulse are by-passed by the  $RC$  shunt across the secondary.

The combination of storage capacitor, pulse transformer, and expander coils produces a half-sine-wave current pulse in the expander coils. The pulse has a duration of 20  $\mu\text{sec}$ . and reaches a peak amplitude of 200 to 350 amp. in 8  $\mu\text{sec}$ ., the actual amplitude depending on the power supply variac setting.

### Circuit Performance and Calibration

Since the integrator amplifier is direct coupled, the jitter in the unclamping instant in terms of input voltage was readily measured and found to be between 0.1 and 0.2 v. Also the "zero trigger" point, or zero energy point on the control dial, may be easily determined. This setting has been found to drift less than 0.1 v. after an adequate warm-up period.

The cathode follower driver for the 5C22 has an output impedance of 160 ohms and delivers a 310 v. pulse with a rise time of 250 v. per  $\mu\text{sec}$ . to the grid of the thyatron. This trigger pulse will reduce the average time jitter in the firing of the 5C22 to the order of 0.01  $\mu\text{sec}$ . (4). Also, the time delay between the triggering of the multivibrator and the 5C22 will be of the order of 0.4  $\mu\text{sec}$ . Owing to the finite rise time of the expander pulse a further variable delay of from 3 to 6  $\mu\text{sec}$ . is added, since expansion occurs at different expander currents for different energy settings.

A discussion of some of these errors in energy calibration appeared in a recent paper by McElhinney *et al.* (5).

A summary of estimated and measured errors in the linear energy scale of our circuits is given in Table I. Corrections which would have to be made for an absolute energy calibration (2) are given approximately in Table II. The correction for the fixed delay of  $2.4 \mu\text{sec.}$  would be at all times less than  $0.05 \text{ Mev.}$  Actually this correction is very nearly compensated by the  $2.1 \mu\text{sec.}$  phase advance of the integrator signal. There is also a variable delay present owing to the finite rise time of the expander pulse. In addition, an energy change is produced by the flux from the expander pulse. Since both the variable time delay and the expander pulse effect are approximately proportional to the initial magnetic field at the time of expansion (5), only small nonlinear corrections to the energy scale should be necessary. McElhinney (5) estimates that the nonlinear corrections from the expander pulse effect are of the order of  $0.02 \text{ Mev.}$

TABLE I  
SUMMARY OF ERRORS IN LINEAR ENERGY SCALE

Source of error	Error	
	$\mu\text{sec.}$	Mev.
Jitter in: amplifier multivibrator 5C22	1 to 2 0.1 0.01	
Total	2.1	0.05
Nonlinearity in expander pulse correction		0.02
Nonlinearities due to delays in circuits		0.03
Error in linear energy scale		0.1 Mev.

TABLE II  
SUMMARY OF INTEGRATOR EXPANDER CORRECTIONS FOR AN ELECTROMAGNETIC CALIBRATION

Source of correction	Correction		
	Fixed delay, $\mu\text{sec.}$	Variable delay, $\mu\text{sec.}$	Correction, Mev.
Amplifier Multivibrator 5C22 Expander	2 ~ 0 0.4	~ 3 to 6	
Totals	+2.4	~ +3 to +6	+0.05 ~ +.08 to +.15
Integrator phase advance Expander pulse	-2.1		-0.05 ~ -.1 to -.2

An absolute electromagnetic calibration (2) of the integrator-expander is possible. However, in view of the number of small but somewhat uncertain

corrections which must be made, it was thought preferable to assume a linear calibration and to use the measured values (3, 5) of the thresholds of several of the better-known nuclear reactions to establish points on this curve. As indicated by Table I, the maximum deviations from a linear energy scale due to jitter and nonlinear corrections should be less than 0.1 Mev. The reactions selected for our calibration were  $C^{12}(\gamma n)C^{11}$  with threshold of 18.7 Mev.,  $Cu^{63}(\gamma n)Cu^{62}$  at 10.9 Mev., and  $Be^9(\gamma n)Be^8$  at 1.67 Mev. (5).

### Acknowledgment

The authors are grateful for the financial assistance from the National Research Council of Canada which made the construction of this apparatus possible.

### References

1. BALDWIN, G. C. and KOCH, H. W. Phys. Rev. 63: 59. 1943.
2. BALDWIN, G. C. and KOCH, H. W. Phys. Rev. 67: 1. 1945.
3. BELL, R. E. and ELLIOTT, L. G. Phys. Rev. 74: 1552. 1948.
4. GLASOE, G. N. and LEBACQZ, J. V. Pulse generators. Vol. 5. Radiation Lab. Series. McGraw-Hill Book Company, Inc., New York. 1948.
5. McELHINNEY, J., HANSON, A. O., BECKER, R. A., DUFFIELD, R. B., and DIVEN, B. C. Phys. Rev. 75: 542. 1949.

## A MORE EXACT FRESNEL FIELD DIFFRACTION RELATION<sup>1</sup>

BY G. A. WOONTON

### Abstract

In general, diffraction relations which were developed for optical purposes have been found to be useful in the prediction of electromagnetic fields due to radiating apertures but, because many radio-optical measurements must be made so close to the aperture that the mathematical approximations in the Fresnel field relation often are invalid, new relations, free from these approximations, must be developed. The optical, Fraunhofer relation has been found to predict the distant field with good accuracy and for this reason the Fresnel field is calculated from the distant field equation by the Fourier transform method. The calculation is found to result in an integral which reduces to Fresnel's integral when the standard optical approximations are made in it. The integral has not been evaluated.

### Introduction

Two types of approximation are present in the calculation of the electromagnetic field in front of a radiating aperture by optical diffraction methods. These are approximations in the fundamental physics of the solution and approximations in the algebraic and trigonometrical processes by which Kirchhoff's general solution is reduced to the solution of a specific problem. The writer, with others (4, 5), has found that for a square aperture as small as 10 wave lengths wide, the field can be predicted with good accuracy by optical diffraction formulae, provided the point at which the field is measured does not lie at an angle of more than 30 or 40 degrees from the normal to the aperture, and provided that the radius vector from the center of the aperture to that point is greater than three or four times the aperture width. From these results it can be inferred that the Kirchhoff solution of the diffraction problem, in spite of its inconsistencies, can be used with success to predict the field of practical radiators, but that trigonometrical and algebraic approximations make the specialized statements of that solution inadequate for use in the region close to the aperture.

The field close to the radiator is particularly interesting in radio-optical measurements. Measuring instruments, such as probes and lenses, are usually placed in the near field, and it is only by a comparison of the predicted with the measured field that the experimenter can estimate the disturbance caused by the measuring instruments. Obstructions in the near field modify distant patterns; an exact knowledge of the Fresnel field is required to predict the effect of the obstruction on the distant field. Apart from these practical considerations, it will not be possible to press the investigation of the inadequacies of the Kirchhoff solution much farther until the near field can be predicted from Kirchhoff's work by equations that are free from extraneous errors. For these and related reasons, optical diffraction formulae, free from mathematical

<sup>1</sup> Manuscript received October 28, 1949.

Contribution from the Department of Physics, McGill University, Montreal, Que.

approximations, are needed for the prediction of the Fresnel field of radiating systems. The analysis which follows applies only to radiating apertures of the linear type, that is, to those with a rectangular aperture and for which the aperture distribution of electric field or potential,  $F(xy)$ , can be expressed as the product of separate distributions in the  $XY$  planes,  $F_1(x)F_{11}(y)$ . The analysis leads to an integral statement of the Fresnel field and this integral, like Fresnel's integral (to which it can be reduced by approximation) has not been integrated, yet, into a closed form by any of the standard methods.

### The Fresnel Field

Experimental evidence shows that standard optical formulae can predict the distant field of a linear radiator but fail in the near field, and, for this reason, it is proposed to calculate the Fresnel field from the distant field in order to take advantage of the relative freedom of the distant field calculation from mathematical approximations.

Define a right-handed rectangular co-ordinate system with its origin at the intersection of the diagonals of a rectangular aperture, its  $X$  and  $Y$  axes perpendicular to the two sides. Let the axes be oriented so that the  $Z$  axis projects into the space where the field is to be predicted. Let the distribution of potential in the aperture be given by the product  $F_1(x)F_{11}(y)$ . At  $z = b$ , along the  $Z$  axis, set up a subsidiary co-ordinate system  $(\xi, \eta)$  with the  $\xi$  and  $\eta$  axes parallel to the  $X$  and  $Y$  axes respectively. The aperture distribution  $F_1(x)F_{11}(y)$  will set up a Fresnel field in the plane of this new co-ordinate system which will be described as  $F_2(\xi)F_{22}(\eta)$  (although in fact each of these must be a function of  $b$  and  $\lambda$  as well as  $\xi$  or  $\eta$ ). The aperture, because of its electric field, will radiate a spherical wave which, by ordinary optical Fraunhofer formulae, can be expressed to close approximation as:

$$\begin{aligned} \phi(x_1y_1z_1) = & \frac{[\cos \theta + 1] \exp \left[ j \left( \omega t - \frac{2\pi R_1}{\lambda} \right) \right]}{R_1} \\ & \times \left\{ \sqrt{\frac{j}{2\lambda}} \int_{-\infty}^{+\infty} F_1(x) \exp \left[ j 2\pi x \frac{\sin \theta_1}{\lambda} \right] dx \right\} \\ & \times \left\{ \sqrt{\frac{j}{2\lambda}} \int_{-\infty}^{+\infty} F_{11}(y) \exp \left[ j 2\pi y \frac{\sin \theta_{11}}{\lambda} \right] dy \right\}, \end{aligned} \quad (1)$$

where  $\phi(x_1y_1z_1)$  may be interpreted as the electric potential at  $P_1(x_1y_1z_1)$ ,  $\omega$  and  $\lambda$  have the significance of the angular velocity and the wave length of the radiated field,  $j$  is the symbol for  $\sqrt{-1}$ ,  $R_1$  is the radius vector from the origin to  $P_1$ ,  $\theta_1$  is the angle between the  $Z$  axis and the projection of the radius vector on the  $XZ$  plane, and  $\theta_{11}$  has the same meaning in the  $YZ$  plane.  $[\cos \theta + 1]$  is the inclination factor, and in it  $\theta$  is defined in the usual manner.

Because the aperture field is not unique, it would have been equally correct to say that the distant field was caused by the Fresnel distribution  $F_2(\xi)F_{22}(\eta)$  in the  $\xi, \eta$  plane. In that case, one would say that a spherical wave was radiated from the point  $(0, 0, b)$  and an equation similar to (1) would be written in which, however, would appear the functions  $F_2(\xi)$  and  $F_{22}(\eta)$  and new polar co-ordinates  $R_2, \theta_2$ , and  $\theta_{22}$ , all appropriate to the new length and angle of the radius vector from  $z = b$  to  $P_1$ .

In order to consider the relation between the two spherical wave fronts, set  $R_1 = R_2 + b$  and, because the expression can be separated into independent functions of the co-ordinates, restrict the attention to the two circular arcs lying in the  $XZ$  plane which represent lines along the two wave fronts radiating respectively from the origin and from  $(0, 0, b)$ . These arcs are of radius  $R_1$  and  $R_2$ . Draw the radius vector  $R_1$  to some point  $P_1$  on the circular arc related to the wave from the origin. It will cut the arc related to the wave front from  $(0, 0, b)$  in another point  $P_2$ . The distance along the radius vector between the two wave fronts  $P_2$  and  $P_1$  can be expressed as

$$\delta \doteq b(1 - \cos \theta) \quad (2)$$

and this expression can be made as accurate as desired by taking  $R_1$  and  $R_2$  large enough, compared to  $b$ ; the same reasoning leads to the use of common angle  $\theta$  in (2) since for  $R_1$  and  $R_2$  very large  $\theta_1 = \theta_2 = \theta$ .

The two wave fronts, because of their separation,  $\delta$ , along the radius vector, are out of phase; the field at  $P_2$  leads the field at  $P_1$  by a factor:

$$\begin{aligned} \exp \left[ j \frac{2\pi}{\lambda} \delta \right] &= \exp \left[ j \frac{2\pi}{\lambda} b(1 - \cos \theta) \right] \\ &= \exp \left[ j \frac{2\pi b}{\lambda} \right] \exp \left[ -b \left\{ \left( \frac{j2\pi}{\lambda} \right)^2 - \left( \frac{j2\pi \sin \theta}{\lambda} \right)^2 \right\}^{\frac{1}{2}} \right]. \end{aligned} \quad (3)$$

No inaccuracy will be introduced by taking the modulus of the field to be the same at  $P_1$  as at  $P_2$  because of the great magnitudes of both  $R_1$  and  $R_2$  compared to  $b$  and the consequent insignificance of  $\delta$ . This information is sufficient to fix the relation between the two integral factors:

$$\int_{-\infty}^{+\infty} F_1(x) \exp \left[ j2\pi x \frac{\sin \theta_1}{\lambda} \right] dx$$

which appeared in Equation (1), and

$$\int_{-\infty}^{+\infty} F_2(\xi) \exp \left[ j2\pi \xi \frac{\sin \theta_2}{\lambda} \right] d\xi$$

which would have appeared if the equation for the wave radiating from  $(0, 0, b)$  had been written. Rewrite (1) so that it expresses the field along the arc on which lies  $P_2$ , that is, the arc associated with the wave radiating from



(0, 0,  $b$ ). This can be done by advancing the phase of all points  $P_1$  to the phase of points  $P_2$ , using (3), by writing  $R_1 = R_2 + b$  in the phase factor  $\exp \left[ j \left( \omega t - \frac{2\pi R_1}{\lambda} \right) \right]$  and by interchanging  $R_1$  with  $R_2$  in the denominator. Equate the rewritten Equation (1) to the Fraunhofer equation (similar to 1) that could have been written for a wave radiating from (0, 0,  $b$ ). After cancelling common factors, the equation appears:

$$Y_1 \exp \left[ -b \left\{ \left( \frac{j2\pi}{\lambda} \right)^2 - \left( \frac{j2\pi \sin \theta}{\lambda} \right)^2 \right\}^{\frac{1}{2}} \right] \int_{-\infty}^{+\infty} F_1(x) \exp \left[ j2\pi x \frac{\sin \theta}{\lambda} \right] dx \\ = Y_2 \int_{-\infty}^{+\infty} F_2(\xi) \exp \left[ j2\pi \xi \frac{\sin \theta}{\lambda} \right] d\xi. \quad (4)$$

The two factors  $Y_1$  and  $Y_2$  are:

$$Y_1 = \sqrt{\frac{j}{2\lambda}} \int_{-\infty}^{+\infty} F_{11}(y) \exp \left[ j2\pi y \frac{\sin \theta_{11}}{\lambda} \right] dy; \\ Y_2 = \sqrt{\frac{j}{2\lambda}} \int_{-\infty}^{+\infty} F_{22}(\eta) \exp \left[ j2\pi \eta \frac{\sin \theta_{22}}{\lambda} \right] d\eta.$$

By restricting this discussion to two circular arcs in the  $XZ$  plane, the angles  $\theta_{11}$  and  $\theta_{22}$  have been fixed at zero and further, since  $Y_1$  and  $Y_2$  in general describe the intensity of two spherical waves along a pair of arcs in the  $YZ$  plane, in the special case under consideration they describe the intensity at the same point and are, therefore, the same constant; consequently  $Y_1$  and  $Y_2$  can be cancelled from Equation (4).

Michelson (2) and other authors have pointed out the reciprocal relation between the aperture distribution and the distant field that it causes, and have justified the calculation of one from the other by the Fourier transform pair relation. Following these authorities, one may regard Equation (4) as a relation between Fourier transforms: hence define

$$\gamma = -\frac{\sin \theta}{\lambda} \quad (5)$$

$$G_1(\gamma) = \int_{-\infty}^{+\infty} F_1(x) \exp [-j2\pi\gamma x] dx \quad (6)$$

$$G_2(\gamma) = \int_{-\infty}^{+\infty} F_2(\xi) \exp [-j2\pi\gamma\xi] d\xi \quad (7)$$

$$G_3(\gamma) = \exp \left[ -b \left\{ \left( \frac{j2\pi}{\lambda} \right)^2 - (j2\pi\gamma)^2 \right\}^{\frac{1}{2}} \right], \quad (8)$$

so that one can rewrite Equation (4) in the form

$$G_2(\gamma) = G_3(\gamma)G_1(\gamma). \quad (9)$$

From the reciprocal property of the transformation it follows that the field  $F_2(\xi)$  (the prediction of which is the objective of this analysis) is given by:

$$F_2(\xi) = \int_{-\infty}^{+\infty} G_3(\gamma)G_1(\gamma) \exp [ + j2\pi\gamma\xi ] d\gamma \\ = \int_{-\infty}^{+\infty} G_1(\gamma) \exp \left[ -b \left\{ \left( \frac{j2\pi}{\lambda} \right)^2 - (j2\pi\gamma)^2 \right\}^{\frac{1}{2}} \right] \exp [ + j2\pi\gamma\xi ] d\gamma. \quad (10)$$

Equation (10) can be transformed to an expression in terms of the aperture field,  $F_1(x)$ , by direct integration or by reference to the tables of Campbell and Foster (1) (see pairs 202 and 867). The transformed integral is

$$F_2(\xi) = \int_{-\infty}^{+\infty} F_1(x) \left( \frac{j2\pi b}{\lambda} \right) \frac{K_1 \left[ j \frac{2\pi}{\lambda} \left\{ (\xi - x)^2 + b^2 \right\}^{\frac{1}{2}} \right] dx}{\pi \{ (\xi - x)^2 + b^2 \}^{1/2}} \quad (11)$$

In this integral  $K_1(\xi, x, \lambda, b)$  is a modified Bessel function of the second kind and first order. It can be written as a Hankel function through the relation

$$K_v(z) = \frac{1}{2} \pi j^{v+1} H_v^{(1)}(jz) = \frac{1}{2} \pi j^{-v-1} H_v^{(2)}(j^{-1}z). \quad (12)$$

and in that form can be separated into real and imaginary parts in terms of the Bessel functions of the first and second kinds.

Equation (11) is very like the simple equation for the Fresnel field in terms of Fresnel's integral. The Bessel function is a phase factor of a somewhat more obscure kind than the simpler exponential function, while the denominator is the distance from an aperture point  $x$  to a field point  $\xi$ . The whole expression directs the user to find the potential at a point  $\xi$  by adding up, in a particular way, elements  $F_1(x)dx$  in the aperture, having due regard for the phase and amplitude changes suffered in transmission from  $x$  to  $\xi$ . Had the problem been solved for the surface of a sphere, instead of, for the arc of a circle, a function  $F(\xi, \eta)$  would have been predicted at a point in the  $\xi, \eta$  plane as the product of two integrals each similar to that in (11) except for the appropriate change in the variables. The real and imaginary parts into which it can be split are reminiscent of Fresnel's  $C$  and  $S$  functions. Because the Bessel functions, of which the real and imaginary parts are integrals, oscillate, it appears that the integral (11) will oscillate in phase and amplitude and that in fact, if the integrals were known, a curve, which would bear a relation to Cornu's spiral could be constructed to predict these quantities.

The standard development of the Fresnel field in terms of the Fresnel's integral makes use of the following approximations: it is assumed that distances

between any aperture point  $x$  and any field point can be taken as  $b$  in the calculation of the modulus of the expression but that in the phase term a second approximation is necessary. The second approximation is obtained from a binomial expansion of the correct expression for the distance between  $x$  and  $\xi$ :

$$r = \left\{ b^2 + (\xi - x)^2 \right\}^{\frac{1}{2}} \div b + \frac{1}{2} \frac{(\xi - x)^2}{b} \quad (13)$$

so that the phase term is written:

$$\exp \left[ -\frac{j2\pi b}{\lambda} \right] \exp \left[ -\frac{j\pi}{b\lambda} (\xi - x)^2 \right]. \quad (14)$$

This development is given in detail by Slater and Frank (3, pp. 180-187). Equation (11) can be verified by showing that with the same type of approximation, it reduces to the Fresnel's integral statement of the field. Assume that  $b$  is large compared to  $\lambda$ , so that the argument of the Bessel function must be large and the approximation:

$$K_0(z) \div \frac{\pi}{2} \sqrt{\frac{2}{\pi z}} \exp(-z) \quad (15)$$

is justified. That is:

$$\left( j \frac{2\pi b}{\lambda} \right) \frac{K_1 \left[ j \frac{2\pi}{\lambda} \left\{ (\xi - x)^2 + b^2 \right\}^{\frac{1}{2}} \right]}{\pi \left\{ (\xi - x)^2 + b^2 \right\}^{1/2}} \div b \sqrt{\frac{j}{\lambda}} \frac{\exp \left[ -j \frac{2\pi}{\lambda} \left\{ (\xi - x)^2 + b^2 \right\}^{\frac{1}{2}} \right]}{\left\{ (\xi - x)^2 + b^2 \right\}^{3/4}}. \quad (16)$$

Assume, next, that as in (13),  $b$  is large when compared with  $(\xi - x)$  so that in the exponential function of (16) the argument can be approximated by two terms of the binomial expansion and in the denominator  $(\xi - x)^2$  can be neglected in comparison to  $b^2$ . With these further approximations (11) becomes:

$$F_2(\xi) \div \exp \left[ -j \frac{2\pi b}{\lambda} \right] \sqrt{\frac{j}{b\lambda}} \int_{-\infty}^{+\infty} F_1(x) \exp \left[ -j \frac{\pi}{b\lambda} (\xi - x)^2 \right] dx. \quad (17)$$

This approximate form is the same as that which is ordinarily obtained from the simple theory. The factor  $\sqrt{\frac{j}{b\lambda}}$  is correct in this case since it must be multiplied by another similar factor, which is carried by the function giving the variation with  $y$ , when the complete expression is written. Before Equation (1) was written, the expression was approximated in the usual way by removing the inclination factor from under the integral sign; this approximation permitted the inclination factor to disappear by cancellation in Equation (4). It should now be brought back and with it the factor  $\frac{1}{2}$  by multiplying the right hand sides of Equations (10), (11), and (17) by  $\frac{(1 + \cos \theta)}{2}$ , outside integral sign, to give equations which are as correct as can be obtained, without introducing new complexities.

### References

1. CAMPBELL, G. A. and FOSTER, R. M. Fourier integrals for practical applications. Bell Telephone Monograph, B-584. 1931.
2. MICHELSON, A. A. Phil. Mag. 9: 506. 1905.
3. SLATER, J. C. and FRANK, N. H. Electromagnetism. McGraw-Hill Book Company Inc., New York. 1947.
4. WOONTON, G. A., HAY, D. R., and VOGAN, E. L. J. Applied Phys. 20: 71. 1949.
5. WOONTON, G. A. and TILLOTSON, J. G. Can. J. Research, A, 25: 315. 1947.

## EFFECT OF THE ILLUMINATION OF THE NEGATIVE ON THE RESOLVING POWER OF A PROJECTION PRINT

By P. A. TATE

### Abstract

Axial measurements have been made of the resolving power of photographic projection printing systems. Besides the usual diffuse and specular systems a third system was considered in which the aperture of the projection lens is not entirely filled by the image of the source. If the relative aperture of this system is calculated considering the source image as the entrance pupil of the lens, then at small relative apertures this system has greater resolving power than the other systems. However, there is no advantage in using the third system at small relative apertures. At large to moderate relative apertures there are only very slight differences among the three systems. Diffusion screens placed in a condenser enlarging system may cause considerable reduction in resolving power if the lens was not previously filled by the image of the source. This effect, and also the high contrast that is very frequently present, are thought to be the origin of references in the literature to sharper pictures obtainable with condenser enlarging systems.

### Introduction

There are two extreme types of enlarging systems that may be termed "diffuse" and "specular". In the diffuse enlarging system the negative is illuminated by a large diffuse source emitting light in all directions. In the specular system the light is directed exclusively towards the lens through the negative by some optical device. An example of each of these types of illumination is shown in Fig. 1. A great many enlargers employ systems which are neither completely diffuse nor completely specular.

The properties of diffuse and specular systems differ in several important respects. In the diffuse system the lens is always completely flooded with light. The effective printing density of the negative is approximately diffuse density (5). The amount of light available at the printing plane is relatively low owing to the large amount of light which falls outside of the lens and to absorption of light in the diffusing screen.

The lens of a specular enlarging system may not be completely flooded with light; e.g., in a condenser enlarger if the source image is smaller than the entrance pupil of the projection lens. Specular density is effective in determining the tones of the image in the printing plane (5). Specular systems can be made much more efficient than diffuse systems from the standpoint of light available on the photographic paper.

Tuttle (6) has studied the problems arising from the differences in behavior of specular and diffuse systems, particularly regarding tone reproduction. He has discussed the change in contrast that accompanies a change in the diffusion characteristics of an enlarger and compared the effective speeds of specular and

<sup>1</sup> Manuscript received November 1, 1949.

Contribution from the Division of Physics, National Research Laboratories, Ottawa, Canada. Issued as N.R.C. No. 2077.

diffuse systems. Information is also given on the effectiveness of diffusion to reduce graininess and to minimize contrast of scratch images in the final print.

It has been mentioned in the literature (2, p. 430) that specular enlarging systems give sharper pictures than are obtainable with diffuse systems; it is not clear whether the comparisons have been made under like conditions of effective relative aperture and print contrast for each type of system. Recently this question has become of greater interest with the appearance on the market of lamps with very small and uniformly bright luminous areas. Claims have been made (1) for these lamps that their use in optical systems can produce

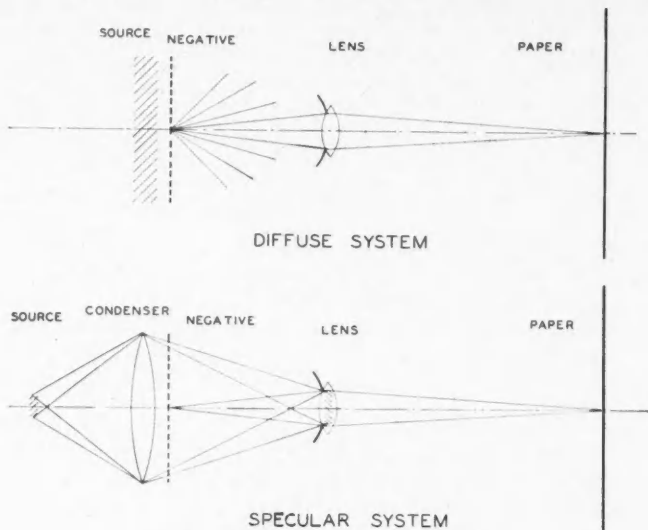


FIG. 1. *Two types of negative illumination.*

results of great resolution and depth of focus. Any exact information on the relative merits of diffuse and different kinds of specular enlarging systems is therefore distinctly useful.

Practical condenser enlargers usually employ tungsten filament lamps in clear bulbs as the light source. Most enlargers with large frosted bulbs and condensing lenses are closer to diffuse systems than truly specular systems. Because of the irregular shape of a clear tungsten source a circular lens aperture can never be completely filled by the source image. We see then that enlargers actually in use are of three types, or combinations of three types: ordinary diffuse, ordinary specular and specular in which the image of the source covers only a portion of the projection lens aperture.

In the last system the resolution and depth of focus depend on the distribution of light in the projection lens. We shall use the terms "relative aperture

of the diaphragm" and "relative aperture of the source image" to describe the illumination of the projection lens in discussions of this system. The relative aperture of the diaphragm is the normal meaning of the term "relative aperture", i.e., the ratio of the diameter of entrance pupil of the projection lens to the focal length of the lens. The relative aperture of the source image will be defined as equal to the relative aperture of the diaphragm when the diaphragm just surrounds the source image. The corresponding terms "aperture of the diaphragm" and "aperture of the source image" will also be used. Provided that the source is a uniform disk the relative aperture of the source image largely determines the illumination in the printing plane. If there were no light outside the source image then the relative aperture of the source image would be the only quantity needed to estimate the performance of a system of this type. However, this condition can never be completely satisfied because there is always some light scattered outside the source image from imperfect condenser surfaces and from the negative. Thus, both the relative aperture of the diaphragm and the relative aperture of the source image are required to describe a condenser enlarging system with an unfilled lens aperture.

Condenser enlargers are frequently used with a certain amount of diffusion introduced into the system. Reports are sometimes seen that this practice decreases the resolution of the condenser system. It was thought desirable to find the extent of the change of resolution in a number of representative lenses when diffusing screens are introduced into a condenser system in which an image of the source smaller than the aperture is formed in the projection lens. This has been done and is described in Section II of this paper.

## I. Comparison of Enlarging Systems

### EXPERIMENTAL METHODS

The axial resolving powers of three types of enlarging systems were compared under controlled conditions. The comparison was made for one diffuse system and two types of specular systems.

The three systems were:

- (A) A diffusely illuminated system.
- (B) A condenser system with a uniform diffusely emitting source imaged on the diaphragm of the enlarging lens. The source was just large enough to cover the lens aperture at its widest opening. Stopping down was provided by the projection lens iris.
- (C) A condenser system with a uniform diffuse source imaged in the enlarging lens as in (B). The lens was kept at its maximum diaphragm opening and stopping down was accomplished by reducing the size of the source and therefore of its image. System (C) of a given relative aperture of the source image was compared with Systems (A) and (B) at an equal relative aperture determined, of course, by the diaphragm.

The enlarging apparatus was mounted horizontally as shown in the photograph Fig. 2. A diffusely emitting light source was made from a dense piece of opal glass, illuminated from behind, and masked off to the right size with a sheet of thin brass. The size of the hole in the brass mask was selected to give an image of the required size at the projection lens. A gunsight lens of high quality

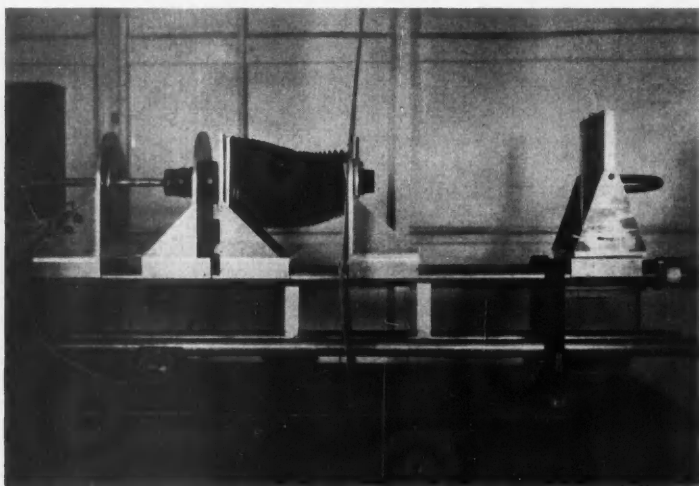


FIG. 2. Photograph of enlarging apparatus

was used as a condenser lens to provide this image. The effect of complete diffuse illumination was obtained by putting a piece of dense flashed opal glass between the condenser lens and the test object. Adjustment was provided for squaring-on the lenses, negative holder, and paper holder. Accurately known displacements of the paper holder could be made with a micrometer advancing screw for focusing.

### Photographic Details

In the position of the negative a high contrast, high resolution bright annulus type (3) resolving power test object was placed at the center of the field. Suc-

TABLE I

Step	Lines per millimeter
18	8.3
19	9.2
20	10.3
21	11.7
22	12.6
23	13.8
24	15.7



cessive steps on the test object increased in size in the nominal ratio  $1: \sqrt[3]{2}$ . The resolving power test object was surrounded by a step tablet of the same emulsion for control purposes. The degree of magnification of all enlarging systems was kept at  $1.8\times$ . Fig. 3 shows a sample enlarged print of the test object. Prints were made on Kodabromide F1 paper and were unferrotyped.

Table I gives the calibration of the resolving power graticule in lines per millimeter on the enlarged print as defined in reference (3).

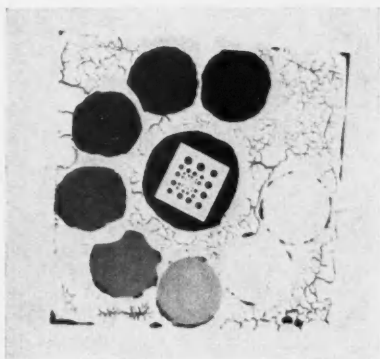


FIG. 3. Enlarged print of the resolving power target and step tablet.

Development was for 90 sec. in D-72 diluted 1:4. Brush development was employed with other precautions usual in sensitometry.

Prints made with all types of enlarging systems had the same contrast. It was possible to achieve this because a very fine grain, and hence low scattering, emulsion (Kodak 548-G) was used for the test object, and the density difference between test object annuli and the background was large enough to take in practically the whole scale of the paper. The condition of constant final contrast is essential to valid comparison of enlarging systems.

### Results and Discussion

In Fig. 4 the curves compare (A) diffuse illumination, (B) condenser illumination with a flooded aperture, and (C) condenser illumination with a small image in the center of the open diaphragm. Systems (A) and (B) having a given relative aperture were compared with System (C) having an equal relative aperture of the source image. The aperture of the diaphragm in System (C) was kept constant at  $F/4.5$  for these curves. All resolution figures are those of the focal position determined by maximum axial resolution. No significant change of focus with stopping down or diffusion was found for any lens. The resolving power is given in steps resolved on the sixth-root-of-two test object and is therefore on a logarithmic scale. Relative apertures are also plotted on

a logarithmic scale. No significant differences appear among the three systems down to an aperture of about  $F/16$  although System (C) seems to have somewhat lower resolution than the others. Beyond an aperture of the source image of  $F/16$  System (C) seems to be considerably superior to the other systems to the extent of three steps or more.

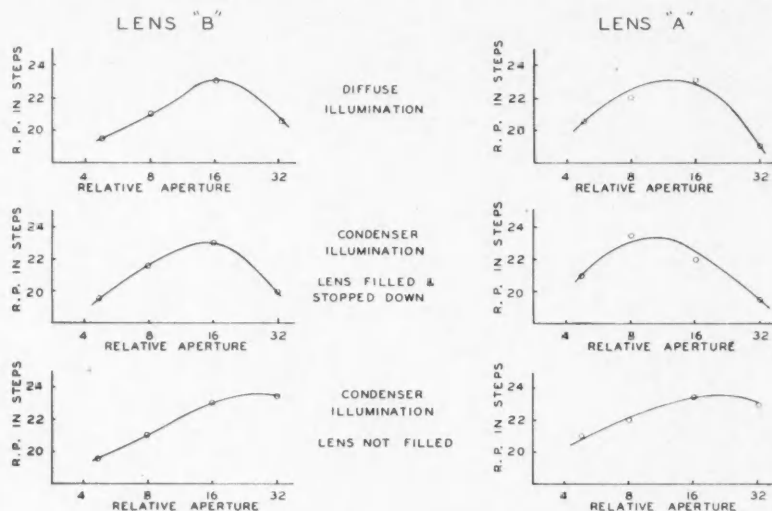


FIG. 4. Axial resolving powers of three different enlarging systems compared.

The failure of the resolving power to drop at small relative apertures of the source image in System (C) is unexpected because, except for the absence of a physical diaphragm around the source image, System (C) is optically similar to System (B) in which a decrease in resolving power takes place. The difference between (B) and (C) can arise only from the small amount of extra light admitted by the open diaphragm of case (C). This light was found to be about 10 or 15% of the total light of System (B). A series of resolving power determinations were made with a lens used in System (C) in which the relative aperture of the diaphragm was reduced in successive steps, thus progressively shutting off the extra light around the source image.

Fig. 5 shows the result of closing down the diaphragm of a system of Type (C) having an aperture of the source image of  $F/32$  to produce finally one of Type (B). Resolving power is noticeably reduced at apertures of the diaphragm of  $F/16$  and smaller. The change is everywhere gradual and investigation showed no sudden changes as the aberrational fringe about the source image was cut off.

An explanation for the behavior of System (C) can be given. It is probably true to say that the image in this system consists of an imperfect image resulting

from the diffraction effects of a small aperture combined with a fainter, more perfect image formed by light from the condenser and graticule surfaces passing through the regions of the lens aperture at which the lens develops its greatest resolving power. Because the test object was of high contrast, reduction in image contrast affected resolution only slightly (4, p. 850) and the final combined image assumed for System (C) was representative of the good image rather than the poor one. A slightly smaller resolving power for System (C)

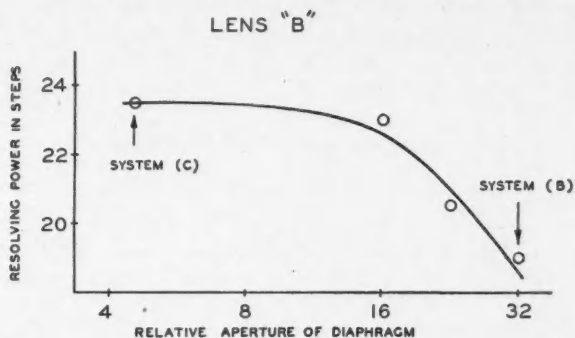


FIG. 5. Variation of resolution as diaphragm in System (C) is closed down to smaller relative apertures. Aperture of the source image is  $F/32$  throughout.

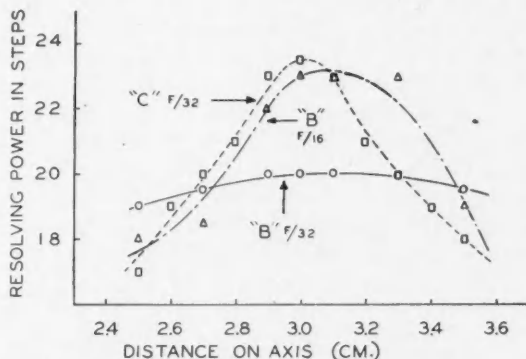


FIG. 6. Resolution through the focal range for Systems (B) and (C).

than (A) or (B) at moderate relative apertures of the source image may also be explained on the basis of the two types of images.

Further confirmation of the above view was had from a comparison of the curves of resolution through the focal range in Systems (B) and (C) shown in Fig. 6. The curves for Systems (B) and (C) at  $F/32$  differ markedly. Depth of focus in System (B) is very great and the curve is typical of normal systems

of this type at small relative aperture. On the other hand for System (C) the curve has a much sharper peak showing that the cone of light affecting resolution is broader in this case. It corresponds, in fact, more closely to the resolution curve for System (B) at  $F/16$  which is included in the figure for comparison.

The depth of focus found for System (C) is not equivalent to that usually obtained with systems of such small relative aperture and in extreme out of focus positions the resolving power drops below that of System (B) at the same relative aperture and focal position. No greater depth of focus therefore may be had by using small sources in the System (C) than by using System (B) at larger apertures.

## II. Decrease in Resolving Power

### EXPERIMENTAL METHODS

Experiments were made to determine the extent of the decrease in axial resolving power that takes place when diffusing screens are introduced into a condenser system in which the projection lens is not completely filled by the source. The experimental system reproduced that of a practical enlarger in which the projection lens was rather greatly stopped down by the size of the source image.

Apparatus very much the same as that already described was used. The light source in this case was either a 3 c.p. or a 32 c.p. clear lamp, depending on the time of exposure required. These two lamps had filaments of very nearly the same maximum dimensions and gave the same results in similar systems. Each source image was adjusted so that its maximum dimension covered a portion of the lens corresponding to an aperture of  $F/16$ , although the lens was set at its largest diaphragm opening. Thus the system was of Type (C) defined in the

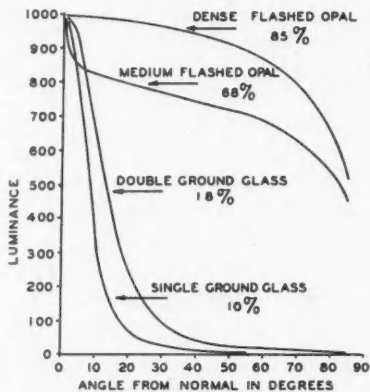


FIG. 7. Luminance-angle curves for four diffusers as seen by a 928, blue sensitive, phototube.

first part of this paper but differed from the system previously studied in two respects. The source was not a uniform diffuse disk as before but a filament of irregular shape, and the system was used only at large relative aperture where the resolving power effects peculiar to System (C) are not encountered.

Four different types of diffusive screens were interposed between the condenser and the test object. They were made of glass ground on one and on both sides, a medium and a dense flashed opal. Luminance-angle curves as seen by a 926 photocell for the four varieties are shown in Fig. 7. To each was assigned a degree of diffusion, "diffusion efficiency" (7), defined as the ratio of the area under the luminance-angle curve to the area under the corresponding Lambert's law curve. There are obvious difficulties to any attempt to describe the properties of a diffuser by one number, but this is easy to calculate and gives a good comparison between diffusers of the same type.

Photographic details were the same as in the previous set of experiments.

### Results and Discussion

Curves of resolving power taken through the focus for an enlarging lens used with different diffusers are shown in Fig. 8. The curves vary but slightly in shape with different degrees of diffusion and except for zero diffusion (specular illumination) are very similar. No change in focus (maximum resolution) can be noticed in these curves. While the peak of resolution in the diffuse case is a little broader than for specular illumination, the latter gives good resolution over a larger range, and from this point of view may be said to have greater depth of focus.

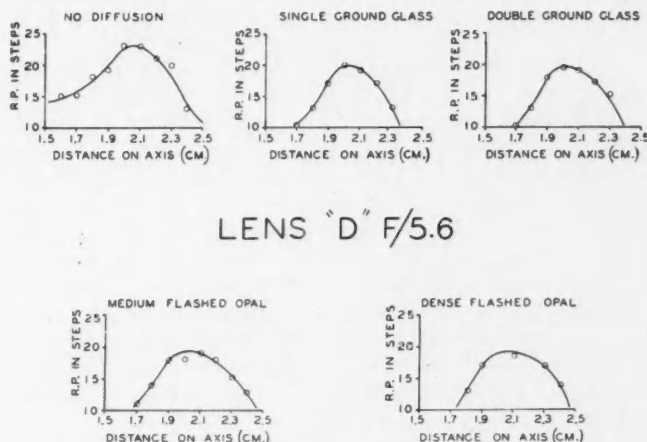


FIG. 8. Axial resolving power vs. distance from the lens (plus an undetermined constant) for several diffusers. Aperture unfilled by source image.

In Fig. 9 the maximum axial resolving power for four lenses is shown plotted against the diffusion efficiency of the diffusing screen behind the test object. The curves all drop rapidly at low values of diffusion and reach quickly a constant resolving power. This may be explained by the fact that initially only the central portion of the lens is working and resolution drops as light is diffused over the outer and less well corrected portions of the lens aperture. After a considerable amount of light has been diffused over the lens aperture a further increase in diffusion does not decrease resolution any more from this cause but only contributes to light producing veiling glare.

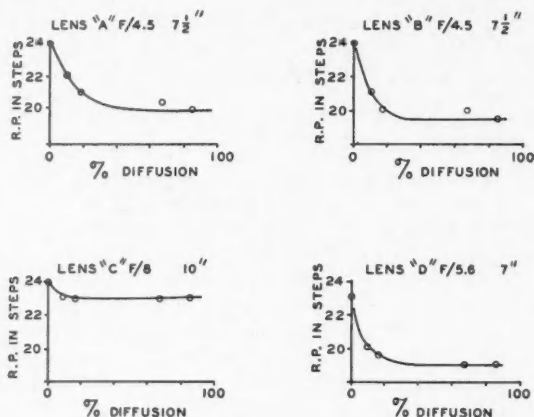


FIG. 9. Axial resolving power vs. diffusion efficiency for an unfilled aperture.

### Conclusions

Provided that the contrast of the final print is kept constant there is no significant difference in resolving power obtainable at large or moderate apertures for the three different types of enlarging systems studied. This result was obtained with a high contrast target, but the result applies with even more strength for low contrast detail. It should be noted that it may not always be possible to achieve the same print contrast throughout the tone range in different systems. At very small relative apertures of the source image the System (C) is distinctly superior in resolving power to Systems (A) and (B) used at equal relative apertures. The value of its superiority is nullified by the fact that at least as great resolving power may be had with Systems (A) and (B) working at larger relative apertures, and also because no increase in depth of focus is achieved with System (C) over that of the same lens used conventionally at moderate relative aperture.

Small amounts of diffusion applied to a condenser enlarger system result in a rapid decrease in resolving power if the full aperture of the enlarging lens is

not already utilized. Probably the extra sharpness achieved with pure condenser systems has been due to the stopping-down effect of an unfilled lens aperture and also the increased contrast that may be had with these systems.

### Acknowledgment

The author wishes to express his thanks to Dr. L. E. Howlett of this laboratory for proposing the problem. Thanks are also due to Mr. W. G. Neville for making many of the prints.

### References

1. BUCKINGHAM, W. D. and DEIBERT, C. R. J. Soc. Motion Picture Engrs. 47: 376. 1946.
2. HENNEY, K. and DUDLEY, B. Handbook of photography. McGraw-Hill Book Company, Inc., New York. 1939.
3. HOWLETT, L. E. Can. J. Research, A, 24: 15. 1946.
4. MEES, C. E. K. The theory of the photographic process. The Macmillan Company, New York. 1942.
5. TUTTLE, C. J. Optical Soc. Am. 24: 272. 1934.
6. TUTTLE, C. J. Optical Soc. Am. 24: 279. 1934.
7. TUTTLE, C. and YOUNG, D. A. J. Soc. Motion Picture Engrs. 19: 842. 1932.

ISOTOPE SHIFT IN THE RESONANCE LINES OF ZINC<sup>1</sup>BY M. F. CRAWFORD, W. M. GRAY,<sup>2</sup> F. M. KELLY,<sup>3</sup> and A. L. SCHAWLOW

## Abstract

The isotopic structures of the Zn I resonance lines 2139 Å ( $4s^2 1S_0 - 4s4p^1P_1$ ) and 3076 Å ( $4s^2 1S_0 - 4s4p^3P_1$ ) excited in an atomic beam source have been resolved with a Fabry-Perot etalon. Shifts in  $\text{cm}^{-1}$  relative to the  $\text{Zn}^{64}$  component are +0.016 and +0.033 in 2139 Å, and +0.023 and +0.046 in 3076 Å for  $\text{Zn}^{66}$  and  $\text{Zn}^{68}$ , respectively. When the normal mass shifts are subtracted, the residual shifts for  $\text{Zn}^{66}$  are +0.010 (2139 Å) and +0.030  $\text{cm}^{-1}$  (3076 Å). The field effect theory of isotope shift predicts equal shifts and the specific mass effect predicts unequal shifts for the  $^1P$  and  $^3P$  levels. Therefore the difference of these residuals is a specific mass effect. The difference has the sense predicted by the specific mass theory and its value, 0.020  $\text{cm}^{-1}$ , is a large fraction of the observed shifts. Thus the specific mass effect must be taken into account before the field effect theory can be used to obtain nuclear properties from isotope shifts in intermediate elements.

## Introduction

Two causes of isotope shift in atomic spectra have been recognized, the mass effect and the field effect. The mass effect consists of two parts, the normal and the specific. The normal effect, which is present in all spectra, is easily calculable and decreases, rapidly at first, as the atomic weight increases. The specific effect, which was first treated by Hughes and Eckart (14), is present in spectra of atoms with more than one electron. It is much more difficult to evaluate precisely than the normal effect.

The contributions of the specific mass effect to isotope shifts have been evaluated theoretically for transitions in the spectra of lithium (14), neon (6), magnesium (23), boron (19), and helium (1, 8, 12, 17). For about half the transitions considered there is fair agreement with experiment, but for the other half the agreement is poor. It is probable that the cases of disagreement between theory and experiment in the spectra of neon and magnesium are due to the use of wave functions that are not sufficiently precise for an accurate evaluation of the integrals. He I affords the best test of the theory since there is at most one integral for each configuration and it can be accurately evaluated. For the singlet transitions (12), the discrepancy between the observed and predicted shifts is 4% on the average and in no case is it greater than 9%. Discrepancies as large as 30% are found for the triplet transitions, but these discrepancies may be partly related to the fact that the triplet fine structure splittings appear to be different for the two isotopes. Thus the He I results confirm the Hughes-Eckart theory as a first approximation, but also indicate that the omission of the electron spin interaction in the potential function may be partially responsible for the residual discrepancies.

<sup>1</sup> Manuscript received August 23, 1949.

Contribution from the McLennan Laboratory, University of Toronto, Toronto, Ont.

<sup>2</sup> Holder of a Fellowship from the Research Council of Ontario. Now at University of Reading, Reading, England.

<sup>3</sup> Holder of a Fellowship under the National Research Council of Canada.



The field effect (5, 9, 20, 21) has been used to explain isotope shifts in the spectra of the heavier elements. Here the normal mass effect is negligible and the field effect gives a consistent explanation (11) of the observed shifts.

No satisfactory explanation has been advanced for isotope shifts in elements of intermediate atomic number. Among the lightest elements there is a general decrease in the magnitudes of the specific mass shifts with increasing atomic number. This has led to the tacit assumption on the part of some authors that the specific mass effect is negligible in all but the lightest elements. Isotope shifts observed in Cu I and Zn II have been assigned (22) to levels as if they were due to the field effect. But the shifts are in the opposite sense to those predicted, if the nucleus of the heavier isotope occupies the greater volume. This inconsistency raises the question whether the specific mass effect may be important in the intermediate elements, as suggested by Bartlett and Gibbons (6). Since the number of integrals contributing to the energy level shifts increases with increasing atomic number, this may well be the case in spite of the decreasing factor  $(1/M_1 - 1/M_2)$ , where  $M_1$  and  $M_2$  are the nuclear masses of the two isotopes.

The specific mass effect in any given transition cannot be estimated without an involved calculation. But it is possible in certain cases by comparing the shifts of a pair of lines to determine the importance of the specific mass effect without a detailed calculation. Such a pair is the resonance lines of zinc, 2139 Å ( $4s^2^1S_0 - 4s4p^1P_1$ ) and 3076 Å ( $4s^2^1S_0 - 4s4p^3P^1$ ). Since these lines have upper levels belonging to the same configuration and a common lower level, they should have the same field effect shifts, as the field effect shift of either a  $4p_{1/2}$  or a  $4p_{3/2}$  electron is very small relative to that of a  $4s$  electron. The specific mass theory, however, predicts that the shifts of the lines should differ by an amount depending only on  $C(4p, 4s)$ , one of the integrals contributing to the shifts of the upper levels (6).

### Experimental

The resonance lines of Zn I were excited in an atomic beam source and resolved with a Fabry-Perot interferometer. The crystalline quartz optical flats of the interferometer were coated with aluminum by rapid evaporation (10). The interferometer was placed between the collimator lens and the prism of a fast spectrograph in which an off-axis paraboloidal mirror is used as the camera objective. The source and spectrograph will be described in detail in forthcoming publications.

The intercombination resonance line (3076 Å) was photographed on Ilford Ordinary and Eastman 103-0 plates. For the singlet resonance line (2139 Å) Ilford QI plates were used.

### Results

The line 3076 Å was resolved without difficulty by a 40 mm. etalon and a 55 mm. etalon. This line is not strongly absorbed in the atomic beam. The density of the beam was therefore made as high as possible without spoiling

the collimation by collisions. No interference was experienced from the second member of the sharp triplet series (3072Å) since the intensity of this triplet in the atomic beam source is negligible compared to that of 3076Å.

The structure of 3076Å consists of three components, the strongest having the lowest frequency and the weakest the highest frequency. The relative intensities of the three components were measured by calibrating the plates with stepped-slit continuous spectra of a hydrogen lamp. The density contours were obtained with a Leeds and Northrup microphotometer. The peak intensity of each component was determined and corrected by subtracting the intensity contributions of the other two components. These corrections were small for the 55 mm. pattern in which the components were well separated. The measured intensities were in good agreement with the relative abundances (13, 15) of  $\text{Zn}^{64}$ ,  $\text{Zn}^{66}$ , and  $\text{Zn}^{68}$ . The separations of the components of 3076Å relative to the  $\text{Zn}^{64}$  component are  $+0.023 \pm 0.001$  for  $\text{Zn}^{66}$  and  $+0.046 \pm 0.001$   $\text{cm}^{-1}$  for  $\text{Zn}^{68}$ .

On the more strongly exposed 40 mm. patterns a weak fringe is observed and is attributed to  $\text{Zn}^{67}$  which has a nuclear moment. The  $\text{Zn}^{67}$  line should have three components with the separations of the hyperfine structure states of  $4s4p\ ^3P_1$ . These separations have been determined by Lysheide and Rasmussen (16) and confirmed by Arroe (2) from the structures of other lines of Zn I. The observed fringe is due to overlapping of adjacent orders of the two outer components of  $\text{Zn}^{67}$ .

The line 2139Å was difficult to resolve because of the strong self-absorption in the atomic beam. Broadening of the components and even partial reversal were observed when the density of the beam was high. The half-widths of the components of this line were made sufficiently small to permit resolution by reducing the density of the highly collimated beam. Under this condition exposures of three to four hours were necessary, even with thinner aluminum films in the etalon. Exposures with a 3 mm. spacer showed that the instrumental width of the fringes corresponded to an effective reflection coefficient of 0.6 at 2139Å. With these films the structure of the line was just resolved using a 73 mm. spacer.

The wave-number separations of the components of 2139Å relative to the  $\text{Zn}^{64}$  component are  $+0.016 \pm 0.002$  for  $\text{Zn}^{66}$  and  $+0.033 \pm 0.002$   $\text{cm}^{-1}$  for  $\text{Zn}^{68}$ . These values include corrections of  $+0.002$  and  $+0.003$ , respectively, for the overlap of the components.

Each of the lines 2139Å and 3076Å has three equally spaced components due to  $\text{Zn}^{64}$ ,  $\text{Zn}^{66}$ , and  $\text{Zn}^{68}$ . The structure observed for 3076Å disagrees in magnitude and in sense with that estimated by Billeter (7) from a study of the absorption by zinc vapor in a magnetic field. Billeter's method was indirect and did not give an accurate determination of the structure. He did not determine the sense of the shift, but assigned it by analogy to the shifts observed in the  $6s^2\ ^1S_0 - 6s6p\ ^3P_1$  transition in Hg I. Auslander (3, 4), in an experiment similar to Billeter's, was unable to detect any structure in 2139Å.

### Discussion

In the following the separations between the  $\text{Zn}^{64}$  and  $\text{Zn}^{66}$  components alone will be discussed. Everything said applies to the separations between the  $\text{Zn}^{64}$  and  $\text{Zn}^{66}$  components except that they are half as great. Shifts are considered positive when the component due to the heavier isotope has the higher wave number.

TABLE I  
ISOTOPE SHIFTS IN THE  $\text{Zn I}$  RESONANCE LINES

	Observed shift	Normal mass shift	Residual shift
2139Å	+0.033	+0.023	+0.010 $\text{cm.}^{-1}$
3076Å	+0.046	+0.016	+0.030 $\text{cm.}^{-1}$

In Table I are shown the observed isotope shifts together with the normal mass shifts and the residual shifts found by subtracting the latter from the former. Since the field effect theory predicts equal shifts for the two lines with the sense opposite to that of the observed residual shifts, it cannot be the sole cause of these shifts. On the specific mass theory the difference,  $0.020 \pm 0.003 \text{ cm.}^{-1}$ , between the residual shifts corresponds to a single integral,  $C(4p, 4s)$  in the notation of Bartlett and Gibbons (6). The observed difference has the sense given by the theory and must therefore be regarded as a specific mass effect. As it is comparable in magnitude to the observed shifts, it follows that the specific mass effect makes an important contribution to the observed shifts and cannot be neglected in considering isotope shifts for elements of intermediate atomic numbers.

A rough calculation of the field effect shift between  $\text{Zn}^{68}$  and  $\text{Zn}^{64}$  in the resonance lines leads to the value  $-0.03 \text{ cm.}^{-1}$  on the assumption that the charge is uniformly distributed in the nucleus and that the radius of a nucleus is proportional to the cube root of the mass. This value is probably an upper limit since the isotope shifts in heavier elements are smaller than that predicted by the field effect theory for this model of the nucleus (11). Since the field effect also is of the same order of magnitude as the observed shifts, but in the opposite sense, the observed residual shifts must be regarded as the resultants of both the field effect and the specific mass effect.

The average of the residual shifts of the resonance lines is  $0.020 \text{ cm.}^{-1}$ . If the field effect is about  $-0.03 \text{ cm.}^{-1}$ , the average specific mass shift must be about  $+0.05 \text{ cm.}^{-1}$ . Since the integral  $C(4p, 4s)$  cancels out in the average of the residual shifts of the two resonance lines,  $+0.05$  is an approximate measure of the specific mass effect that corresponds to the following sum of integrals (6),  $C(4p, 1s) + C(4p, 2s) + C(4p, 3s) + 10C(3d, 4p) - 3C(2p, 4s) - 3C(3p, 4s)$ .

The experimental proof of the importance of the specific mass effect in  $\text{Zn I}$  has a bearing on the interpretation of the isotope shifts observed for other intermediate elements and the change of the sense of the isotope shift with

increasing atomic number. Schüler and Westmeyer (22) have compared the shifts in corresponding lines of Cu I, Zn II, Cd II, and Hg II arising from the transitions between the levels of the configurations  $d^9s^2$  and  $d^{10}p$ . In all these spectra the observed shifts have been arbitrarily assigned to the  $d^9s^2$  configuration by analogy with Hg II where the field effect alone will qualitatively explain the shifts. This assignment of shifts leads to the result that the electrons of the  $d^9s^2$  configuration are more firmly bound in the heavier isotopes of copper and zinc. If this result is interpreted on the basis of the field effect alone, the nucleus of the heavier isotope has the smaller volume. This conclusion is now questionable in the light of the relatively large specific mass effect established in Zn I. In Cd II the sense of the shift in the  $d^9s^2$  configuration is that predicted by the field effect theory and is opposite to that in Cu I and Zn II.

It is possible to explain the sense of the shift in Cu I and Zn II. The specific mass shifts for both the  $d^{10}p$  and  $d^9s^2$  configurations result in the energy levels of the heavier isotope lying higher. This is the same sense as the field effect shift so that here the two effects are additive. The  $d^{10}p$  configuration contains no  $s$  electron and will have negligible field effect shift. The  $d^9s^2$  configuration, with two  $s$  electrons, has a larger field effect shift. Thus if one assumes that the specific mass shift for the  $d^{10}p$  configuration is larger than the sum of the specific mass and the field effect shifts of the  $d^9s^2$  configuration the sense of the observed line shifts is explained.

Since the field effect shift increases with increasing atomic number and the specific mass effect probably decreases owing to the factor  $(1/M_1 - 1/M_2)$ , the sense of the shift in these transitions may be expected to change with increasing nuclear charge. The changed sense is observed in Cd II. However, the data available are not sufficient to verify this suggestion. To establish such an explanation the shifts in the levels relative to a datum of zero shift for ionization must be determined uniquely by measuring the shifts in a large number of lines.

The discovery of a relatively large specific mass effect in the Zn I intercombination resonance line has a bearing on Mrozowski's conclusion (18) that there is evidence of a "pure nuclear", or field effect isotope shift in the band spectrum of ZnH. The specific mass effect is not negligible as assumed by Mrozowski and possibly could account for the small residual shift ( $0.007 \text{ cm}^{-1}$ ) attributed by him to a pure nuclear effect.

The magnitudes of field effect shifts give information about the nucleus (11), but, as shown by the results of this investigation, these cannot generally be determined for the intermediate elements without numerical calculations of the specific mass shifts. The nature of the integrals that must be evaluated is such that precise values can only be obtained when very accurate wave functions are used. Until accurate integrals are available the prospect of getting significant information about nuclei of intermediate mass from the magnitudes of isotope shifts is not good.

## References

1. ANDREW, A. and CARTER, W. W. Phys. Rev. 74: 838. 1948.
2. ARROE, O. H. Phys. Rev. 74: 1263. 1948.
3. AUSLANDER, J. Helv. Phys. Acta, 11: 562. 1938.
4. AUSLANDER, J. Helv. Phys. Acta, 12: 168. 1939.
5. BARTLETT, J. H. Nature, 128: 408. 1931.
6. BARTLETT, J. H. and GIBBONS, J. J. Phys. Rev. 44: 538. 1930.
7. BILLETER, W. Helv. Phys. Acta, 7: 524. 1934.
8. BRADLEY, L. C. and KUHN, H. Nature, 162: 412. 1948.
9. BREIT, G. Phys. Rev. 42: 348. 1932.
10. CRAWFORD, M. F., GRAY, W. M., SCHAWLOW, A. L., and KELLY, F. M. J. Optical Soc. Am. 39: 888. 1949.
11. CRAWFORD, M. F. and SCHAWLOW, A. L. Phys. Rev. 76: 1310. 1949.
12. FRED, M., TOMKINS, F. S., and BRODY, J. K. Phys. Rev. 75: 1772. 1949.
13. HESS, D. C., INGRAM, M. G., and HAYDEN, R. J. Phys. Rev. 74: 1531. 1948.
14. HUGHES, D. S. and ECKART, C. Phys. Rev. 36: 694. 1930.
15. LELAND, W. T. and NIER, A. O. Phys. Rev. 73: 1206. 1948.
16. LYSHEDE, J. M. and RASMUSSEN, E. Z. Physik. 104: 434. 1937.
17. MANNING, T. P. Phys. Rev. 76: 173. 1949.
18. MROZOWSKI, S. Phys. Rev. 58: 597. 1940.
19. OPECHOWSKI, W. and DEVRIES, D. A. Physica, 6: 913. 1939.
20. RACAH, G. Nature, 129: 723. 1932.
21. ROSENTHAL, J. E. and BREIT, G. Phys. Rev. 41: 459. 1932.
22. SCHÜLER, H. and WESTMEYER, H. Z. Physik, 82: 685. 1933.
23. VINTI, J. P. Phys. Rev. 56: 1120. 1939.

FORBIDDEN TRANSITIONS IN DIATOMIC MOLECULES<sup>1</sup>I. THE QUADRUPOLE ROTATION-VIBRATION SPECTRUM OF H<sub>2</sub>

BY G. HERZBERG

## Abstract

Four lines of the 2-0 band and four lines of the 3-0 band of the quadrupole rotation-vibration spectrum of H<sub>2</sub> have been observed and measured using effective absorbing paths of 10 to 50 km. atm. From this spectrum improved values of the rotational and vibrational constants of H<sub>2</sub> in its electronic ground state have been obtained.

## A. Introduction

The possible transitions between the various energy levels of diatomic molecules are determined by well known selection rules.\* These selection rules depend on the type of radiation considered (electric dipole, magnetic dipole, electric quadrupole radiation, etc.) and on the coupling conditions in the molecule. By far the strongest transitions are those corresponding to an alternating electric dipole moment of the molecule, and usually Hund's cases (a) or (b) are good approximations to the coupling conditions. Transitions violating the selection rules holding under these conditions are designated as forbidden transitions.

Three types of forbidden transitions may be distinguished:

(1) Those that violate a selection rule that holds only in a certain approximation or for certain coupling conditions; for example, the rule that states of different multiplicity do not combine with one another ( $\Delta S = 0$ );

(2) Those that violate a selection rule that holds rigorously for electric dipole radiation; they may occur weakly as *magnetic dipole* or *electric quadrupole radiation*;

(3) Those that violate a rigorous selection rule but occur on account of the presence of external fields or at elevated pressures (*enforced dipole radiation*).

Several examples of each of these three types of forbidden transitions have been found.\* Some of these occur in absorption in the earth's atmosphere, others in emission in the spectrum of the night sky; still others are suspected to play a role in the spectrum of the night sky and in the spectra of planets. A further study of these forbidden transitions may therefore be expected to shed more light on the problem of the upper atmosphere of the earth and of planetary atmospheres. In addition such studies will lead to a better understanding of the operation of the selection rules, of the electronic structure of the particular molecules, and to a more precise determination of certain impor-

<sup>1</sup> Manuscript received November 22, 1949.

Contribution from the Division of Physics, National Research Laboratories, Ottawa, Canada. Issued as N.R.C. No. 2086.

\* See, for example, Herzberg (9).

tant molecular constants. On the basis of such considerations a series of investigations of forbidden transitions in diatomic molecules has been initiated.

The present first paper in this series deals with the quadrupole rotation-vibration spectrum of  $H_2$ .\* A second paper will deal with the forbidden near-ultraviolet bands of  $O_2$ . Further work on other molecules is being prepared.

### B. Theoretical Considerations

It is well known that the occurrence of ordinary infrared vibration spectra of diatomic molecules depends on the presence of a permanent dipole moment. For homonuclear molecules the dipole moment is zero and therefore no dipole vibration spectrum can occur. This conclusion may be verified in the energy level diagram of Fig. 1 by noting that the transitions with  $\Delta J = \pm 1$  would

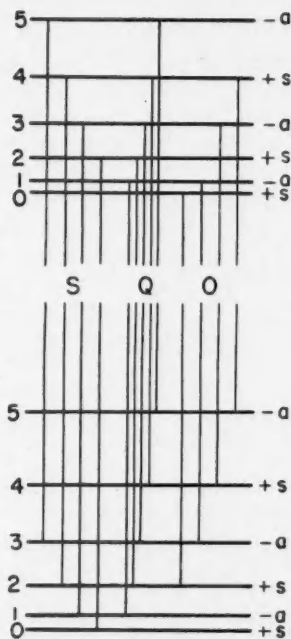


FIG. 1. Energy level diagram for the quadrupole rotation-vibration spectrum of a homonuclear molecule.

violate the rule that symmetric rotational levels do not combine with anti-symmetric ones while transitions with  $\Delta J = 0$  would violate the parity rule (positive rotational levels combine only with negative ones). Since no other  $\Delta J$  values are allowed for dipole radiation it follows that the dipole vibration

\*For preliminary notes on this work see Herzberg (7, 8).



spectrum is rigorously forbidden. However, as was pointed out several years ago (6), since homonuclear molecules may have a quadrupole moment, a quadrupole vibration spectrum may occur.

The selection rules for quadrupole radiation are

$$\Delta J = 0, \pm 1, \pm 2 \quad (1)$$

with the restriction that  $J' + J''$  must be at least 2, and the rule

$$+ \longleftrightarrow +, - \longleftrightarrow -, + \longleftrightarrow - \quad (2)$$

where  $\longleftrightarrow$  stands for "does not combine with". On the basis of these selection rules and the additional general rule that symmetric do not combine with antisymmetric rotational levels it is immediately seen from Fig. 1 that only the three branches with  $\Delta J = +2, 0, -2$  can occur. According to the international nomenclature these branches are designated as *S*, *Q*, and *O* branches. The first lines in these branches are those with  $J = 0, 1$ , and 2 respectively.

In the case of the  $H_2$  molecule James and Coolidge (10) have made more detailed calculations of the variation of the quadrupole moment with internuclear distance and have predicted the relative and absolute intensities of the 1-0, 2-0, and 3-0 infrared vibration bands. According to them the integrated absorption coefficients of the first lines of the *S* branches of these bands are in the ratios  $8.1 \times 10^{-9}$ ,  $7.3 \times 10^{-9}$ , and  $1.5 \times 10^{-9}$  respectively to the first line of the *R* branch of the (allowed) fundamental of HCl. According to Herzberg (6) this means that the minimum path lengths required for the  $H_2$  quadrupole bands are 2.5, 2.7, and 13.0 km. atm. respectively, assuming a temperature of 150°K. (at room temperature the minimum path lengths would be slightly higher). It may be noted that the intensity decreases in the series 1-0, 2-0, 3-0 much more slowly than for ordinary dipole vibration spectra, for example that of HCl. This is due partly to the fact that the absorption coefficient for quadrupole radiation is proportional to  $\nu^3$  rather than  $\nu$  as for dipole radiation and partly to the unusually large mechanical and electrical anharmonicity of the  $H_2$  molecule.

James and Coolidge have also given theoretical expressions for the line strengths of the individual lines. They are (disregarding the intensity alternation due to the nuclear spin):

$$\text{for } \Delta J = +2 \text{ (S branch): } S_J^S = \frac{(J+1)(J+2)}{(2J+3)} \quad (3)$$

$$\text{for } \Delta J = 0 \text{ (Q branch): } S_J^Q = \frac{2J(J+1)(2J+1)}{3(2J-1)(2J+3)} \quad (4)$$

$$\text{for } \Delta J = -2 \text{ (O branch): } S_J^O = \frac{J(J-1)}{(2J-1)} \quad (5)$$

It is easily seen on the basis of these formulae that the intensity within each branch follows a course similar to that in ordinary infrared bands. However,



in the case of  $H_2$  because of the small moment of inertia the intensity maxima are expected at the first or second line of each branch.

With the long optical path recently obtained by multiple traversals (2) it appeared possible to surpass the minimum absorbing paths required for obtaining the quadrupole rotation-vibration spectrum of  $H_2$ . Therefore an attempt was made to photograph this spectrum. Some more general interest attaches to this problem since up to now no case of quadrupole radiation had been found in molecules and no case of quadrupole *absorption* for any atomic system; all previously established cases of quadrupole radiation were observed in emission (e.g., the auroral green line).

### C. Observed Spectrum

The large absorption tube described in more detail in a previous publication (2) is 22 m. long and has a diameter of 25 cm. Using White's method the light from the filament of a small lamp can be made to traverse the tube up to 240 times, depending on the quality of the mirrors and the spectral region to be photographed. Thus an actual path length of 5300 m. can be obtained. By increasing the pressure to 10 atm. an effective path length of 53 km. atm. can be reached which is well above the minimum path length predicted for the 3-0 band of the quadrupole spectrum of  $H_2$ .

The absorption tube was therefore filled with  $H_2$  to a pressure of about 9 atm. and the spectrum in the region of the 3-0 band (8000 to 8600 Å), for about 240 traversals, was taken in the second order of the 21 ft. grating spectrograph at Yerkes Observatory. Absorption lines were indeed found near four of the predicted wave lengths which were expected to be the strongest. However, since there is a fairly strong  $H_2O$  band in the same spectral region and since the  $H_2$  lines do not form an obvious band but are some 200 Å apart from one another it is necessary to compare the spectrum obtained in  $H_2$  with one in air, both containing water vapor. This comparison is illustrated in Fig. 2a for three of the lines of the 3-0  $H_2$  band. The reality of the  $H_2$  lines is clearly demonstrated by this comparison.

In the region of the 2-0 band (11300 to 12400 Å) the plate sensitivity is so low that only 100 or even fewer traversals could be used. Fortunately the 2-0 band is stronger than the 3-0 band (see above) and there is no difficulty in observing it even though again a strong  $H_2O$  band occurs in this region. Fig. 2b shows three of the four observed lines obtained in the first order of the 21 ft. grating.

Table I lists the wave lengths and wave numbers of the eight lines that were found. All but  $S(0)$  and  $S(2)$  of the 2-0 band and  $S(2)$  of the 3-0 band were measured on two or more plates. Second and third order iron lines were used as standards, and the vacuum correction was calculated using the index of refraction data of Barrell and Sears (1).

It is noteworthy that the  $H_2$  lines are appreciably sharper than the accompanying  $H_2O$  lines and in fact as sharp as the slit width and resolution of the spectrograph will allow, in spite of the comparatively high pressure of 5 to 10 atm. No systematic investigation of the pressure dependence of the  $H_2$  absorption was made but a qualitative comparison of exposures made at different pressures indicates a variation with the first power rather than the square of the pressure.

TABLE I  
QUADRUPOLE ROTATION-VIBRATION LINES OF  $H_2$

Designation	$\lambda_{\text{air}}$	$\nu_{\text{vac}}$ (observed)	O-C <sub>1</sub>	O-C <sub>2</sub>
2-0	$\left\{ \begin{array}{l} Q(1) \\ S(0) \end{array} \right.$	$\left\{ \begin{array}{l} 12379.90_4 \\ 11892.49_3 \end{array} \right.$	$\left\{ \begin{array}{l} 8075.39_8 \\ 8406.36_1 \end{array} \right.$	$\left\{ \begin{array}{l} +2.598 \\ +2.427 \end{array} \right.$
	$\left\{ \begin{array}{l} S(1) \\ S(2) \end{array} \right.$	$\left\{ \begin{array}{l} 11618.97_4 \\ 11379.22_4 \end{array} \right.$	$\left\{ \begin{array}{l} 8604.25_4 \\ 8785.54_0 \end{array} \right.$	$\left\{ \begin{array}{l} +2.343 \\ +2.166 \end{array} \right.$
				$\left\{ \begin{array}{l} +0.014 \\ -0.028 \\ +0.018 \\ -0.003 \end{array} \right.$
3-0	$\left\{ \begin{array}{l} Q(1) \\ S(0) \end{array} \right.$	$\left\{ \begin{array}{l} 8497.491 \\ 8272.686 \end{array} \right.$	$\left\{ \begin{array}{l} 11764.94_3 \\ 12084.65_1 \end{array} \right.$	$\left\{ \begin{array}{l} +3.908 \\ +3.766 \end{array} \right.$
	$\left\{ \begin{array}{l} S(1) \\ S(2) \end{array} \right.$	$\left\{ \begin{array}{l} 8150.680 \\ 8046.438 \end{array} \right.$	$\left\{ \begin{array}{l} 12265.54_3 \\ 12424.44_2 \end{array} \right.$	$\left\{ \begin{array}{l} +3.534 \\ +3.293 \end{array} \right.$
				$\left\{ \begin{array}{l} -0.012 \\ +0.022 \\ -0.009 \\ +0.001 \end{array} \right.$
	$\text{\AA}$	$\text{cm.}^{-1}$	$\text{cm.}^{-1}$	$\text{cm.}^{-1}$

#### D. Rotational and Vibrational Constants of $H_2$ in its Ground State

The observed wave numbers of the  $H_2$  quadrupole lines deviate slightly but systematically from those calculated from the data derived by Jeppesen (11), Urey, Teal, and MacWood (14, 13), from the ultraviolet spectrum and the Raman spectrum. These deviations are given in the fourth column (O-C<sub>1</sub>) of Table I. The reason for these deviations lies partly in the much lower wave number accuracy in the ultraviolet compared to the photographic infrared ( $0.1 \text{\AA}$  corresponds to  $6.9 \text{ cm.}^{-1}$  at  $1200 \text{\AA}$  and  $0.069 \text{ cm.}^{-1}$  at  $12000 \text{\AA}$ ) and partly in the lack of reliable standards in the ultraviolet which may lead to rather large systematic errors.

The vibrational and rotational energy of a diatomic molecule (in  $\text{cm.}^{-1}$  units) is given by

$$T(v, J) = G(v) + F_v(J), \quad (6)$$

where

$$G(v) = \omega_e(v + \frac{1}{2}) - \omega_e x_e(v + \frac{1}{2})^2 + \omega_e y_e(v + \frac{1}{2})^3 + \dots \quad (7)$$

$$F_v(J) = B_v J(J+1) - D_v J^2(J+1)^2 + H_v J^3(J+1)^3 + \dots \quad (8)$$

$$B_v = B_e - a_e(v + \frac{1}{2}) + \gamma_e(v + \frac{1}{2})^2 + \dots \quad (9)$$

$$D_v = D_e + \beta_e(v + \frac{1}{2}) + \dots \quad (10)$$

with the usual meanings for the various symbols.

Unfortunately the eight quadrupole lines measured are not sufficient to determine all the vibrational and rotational constants independently. Nor is

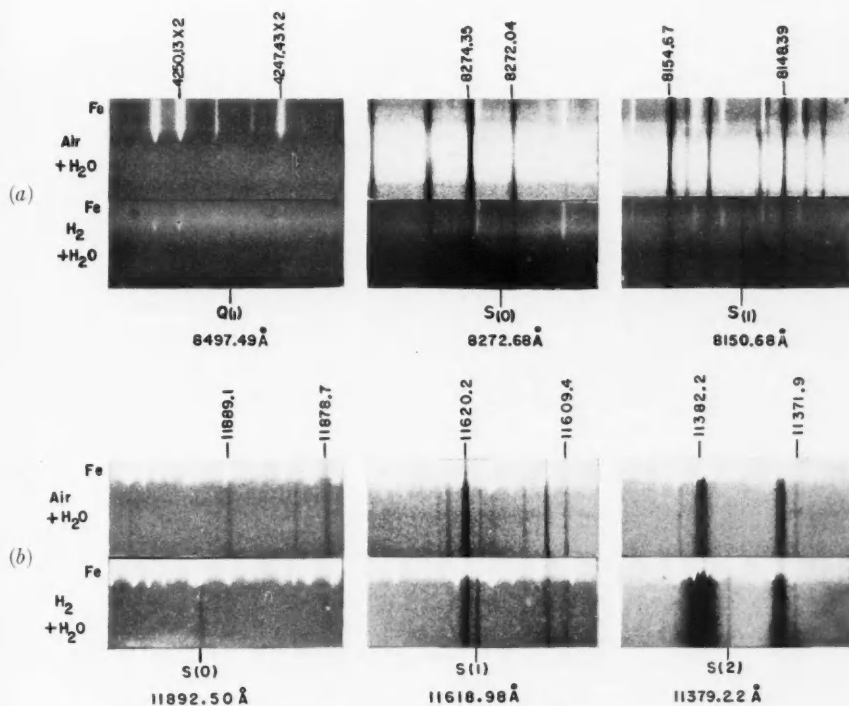


FIG. 2. Spectrograms of several lines of the quadrupole spectrum of H<sub>2</sub>.

(a) the 3-0 band (second order of 21 ft. grating, equivalent path 45 km. atm., exposure time 60 min.)

(b) the 2-0 band (first order of 21 ft. grating, equivalent path 12 km. atm., exposure time 10 to 40 hr.)

In each case the bottom strip shows the spectrum obtained with hydrogen, the top strip that obtained with air, both containing some water vapor.



it possible to determine the rotational constants by the usual method of combination differences. An estimate of the consistency of the data can be obtained by evaluating the differences of corresponding lines in the two bands (i.e.  $S_{v=3}(1) - S_{v=2}(1)$ , etc.). These differences equal the differences of corresponding rotational levels (of equal  $J$ ) in the two vibrational levels  $v = 3$  and  $v = 2$  and according to Equations (6) and (8) are given by

$$T(3, J) - T(2, J) = \Delta G_{2\frac{1}{2}} - (B_2 - B_3)J(J+1) + (D_2 - D_3)J^2(J+1)^2 - \dots \quad (11)$$

where  $\Delta G_{2\frac{1}{2}} = G(3) - G(2)$  and where  $J$  refers here to the upper state of the line considered. In Fig. 3 these differences [after addition of  $2.7J(J+1)$  in order to take out most of the slope] are plotted against  $J(J+1)$  as circles. The slope of the line thus obtained near  $J = 0$  added to  $2.7$  gives  $B_2 - B_3$  while

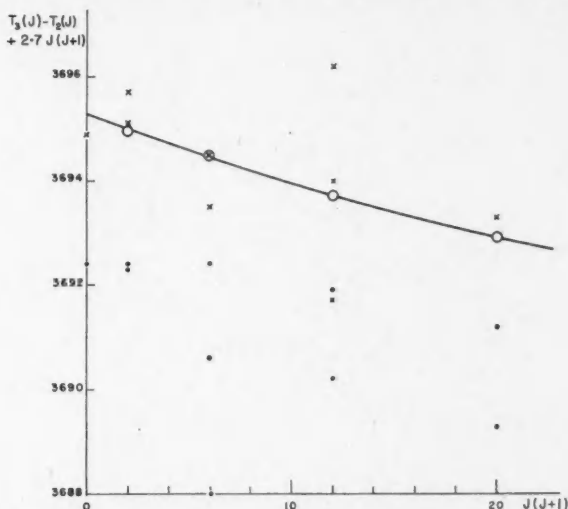


FIG. 3. Energy differences of corresponding rotational levels with  $v = 3$  and  $v = 2$  as obtained from the quadrupole spectrum (O) and from the ultraviolet Lyman bands (x) and Werner bands (•) of hydrogen.

the deviation from a straight line is due to the quartic term. Using Urey and Teal's  $D_v$  values and a  $B_2 - B_3$  value corresponding to the final  $B_v$  values (see below) the full-line curve in Fig. 3 is obtained which represents the observed values (circles) very satisfactorily.

The same differences  $T(3, J) - T(2, J)$  can also be obtained from the ultraviolet Lyman and Werner bands measured by Jeppesen (11). Using the  $P$  and  $R$  branches of the 1-2 and 1-3 Lyman bands and the  $P$ ,  $Q$ , and  $R$  branches of the 0-2 and 0-3 Werner bands and plotting against the  $J$  value of the lower state the points represented by small crosses and dots respectively in Fig. 3 are obtained. It is seen that these points show considerable scatter. Moreover

the points derived from the Werner bands deviate systematically from those derived from the Lyman bands by an amount of the same order as the o-c<sub>1</sub> values in Table I.

The method adopted to improve the vibrational and rotational constants of H<sub>2</sub> on the basis of the measurements of the quadrupole spectrum was as follows: The individual lines were expressed in terms of the band origins  $\nu_{2-0}$  and  $\nu_{3-0}$  and the rotational constants  $B_2, B_3, D_2, D_3$  and  $H_2 \approx H_3 \approx H_e$ , for example

$$S_{v=2}(1) = \nu_{2-0} + 12B_2 - 144D_2 - 2B_0 + 4D_0 + 1720H_e.$$

Using this and seven similar equations for the other observed quadrupole lines and substituting the values of  $D_0, D_2, D_3, H_e$  from Urey and Teal (14) a least squares solution for  $\nu_{2-0}, \nu_{3-0}, B_0, B_2, B_3$  was carried out. The values obtained for these constants and the values of  $\omega_e, \omega_e x_e, \omega_e y_e, B_e, a_e$ , and  $\gamma_e$  derived from them are listed in the last column of Table II. The preceding column of Table

TABLE II  
ROTATIONAL AND VIBRATIONAL CONSTANTS OF H<sub>2</sub> IN ITS GROUND STATE

	From the ultraviolet spectrum	From the quadrupole spectrum
$B_0$	59.331 cm. <sup>-1</sup>	59.318 cm. <sup>-1</sup>
$B_2$	53.506 "	53.480 "
$B_3$	50.673 "	50.635 "
$B_e$	60.848 "	60.809 "
$a_e$	3.0670 "	2.993 "
$\gamma_e$	0.06840* "	0.0247 "
$D_e$	0.04648 "	Taken over
$\beta_e$	-0.00134 "	
$H_e$	$5.18 \times 10^{-5}$ "	
$\nu_{1-0}$	4160.2† "	
$\nu_{2-0}$	8084.44 "	
$\nu_{3-0}$	11778.34 "	8087.05 <sub>0</sub> "
$\omega_e$	4405.30 "	11782.31 <sub>0</sub> "
$\omega_e x_e$	125.325 "	4395.24 "
$\omega_e y_e$	+1.9473‡ "	117.99 <sub>0</sub> "
$r_e$	$0.74142 \times 10^{-8}$ cm.	+0.29 <sub>3</sub> "
$k_e$	$5.76007 \times 10^8$ dynes/cm.	$0.74166 \times 10^{-8}$ cm.
		$5.7337_7 \times 10^8$ dynes/cm.

\*Based on a four term formula with  $-0.0065(v + \frac{1}{2})^2$  as the last term.

†From the Raman spectrum [Teal and MacWood (13)].

‡Based on a four term formula with  $\omega_e x_e = -0.11265$ .

II contains the corresponding constants of Urey, Teal, and MacWood (13, 14). As a check, using the new set of constants the positions of the individual quadrupole lines were calculated. The deviations from the observed values are listed under o-c<sub>2</sub> in Table I. Considering that only five constants were determined from the eight lines, the agreement of the observed and calculated values within  $\pm 0.02$  cm.<sup>-1</sup> must be considered significant and indicates that the new constants represent a genuine improvement. An even better agreement might have been expected if it were not for the fact that all the lines except  $S(1)$  are rather weak and difficult to measure.

The constants  $D_e, \beta_e$ , and  $H_e$  used here were obtained by Jeppesen (11), and Urey and Teal (14) from their values of  $B_e, a_e, \omega_e, \omega_e x_e$  by means of theoretical

formulae and not by direct determination from the combination differences.\* When the new constants of Table II are substituted in the same formulae for  $D_e$ ,  $\beta_e$ , and  $H_e$  the following values are obtained

$$D_e = 0.04656, \beta_e = -0.00180, H_e = 5.016 \times 10^{-5}$$

of which the first two deviate rather more than expected from the original set of constants. Using these constants for a second least squares solution for  $\nu_{2-0}$ ,  $\nu_{3-0}$ ,  $B_0$ ,  $B_2$ ,  $B_3$  yields values that give a much poorer representation of the quadrupole lines (deviations  $\pm 0.05$  instead of  $\pm 0.02$ ) and this would be still worse in the next higher approximation. Therefore the  $D_e$ ,  $\beta_e$ , and  $H_e$  values of Urey and Teal (14) are considered preferable. As shown by Dunham (4) a breakdown of the theoretical formulae for  $D_e$ ,  $\beta_e$ , and  $H_e$  may be expected particularly for a molecule like  $H_2$  for which  $B_e^2/\omega_e^2$  is especially large. Moreover it must be remembered that the  $B_e$  and  $\omega_e$  values given here are based on only three  $B_v$  and  $\Delta G_{v+1}$  values with low  $v$  respectively which indicate a positive curvature of the  $B_v$  and  $\Delta G$  curves while for higher  $v$  values a negative curvature is certainly present.

While it is considered that the new rotational and vibrational constants are superior for a representation of the first four vibrational levels, they are definitely not applicable to the higher vibrational levels. It must also be emphasized that the impossibility of a direct determination of the  $D_v$  values introduces an appreciable uncertainty into the  $B_v$  values. The  $\Delta G$  values are much less affected by this uncertainty.

The old and new values for the force constant  $k_e$  and the internuclear distance  $r_e$  [using modern conversion factors, see Herzberg (9)] are included in Table II.

### E. Discussion

Shortly after the preliminary announcement of the above results, Crawford, Welsh, and Locke (3, 15) reported the observation of the fundamentals (1-0 transitions) of  $N_2$ ,  $O_2$ , and  $H_2$  in absorption at high pressure. This absorption is clearly due to induced dipole radiation since it varies with the square of the pressure. In agreement with this interpretation the line-width is of the order of  $250 \text{ cm}^{-1}$ . In contrast the line-width of the  $H_2$  lines here observed is as small as the resolving power of the spectrograph used permits, that is, smaller than  $0.05 \text{ cm}^{-1}$  even at 10 atm. pressure. Such a small line-width is expected for quadrupole radiation. This together with the fact that the intensity of absorption is close to the predicted value leaves no doubt that the spectrum here reported is a genuine quadrupole rotation-vibration spectrum.†

Since the absorbing path used here is considerably larger than that used by Crawford, Welsh, and Locke at the same pressure (10 atm.) one might have expected to find the induced dipole spectrum in addition to the quadrupole

\*Fig. 3 shows that the scatter of the ultraviolet measurements is much too large for such a direct determination.

†The original suggestion of Crawford, Welsh, and Locke (3) that the spectrum here considered is an induced dipole spectrum was withdrawn in their second note (15). The similar suggestion by Mizushima (12) has also been withdrawn (private communication).

spectrum. No evidence of broad absorption bands underlying the observed lines was found although this is difficult to ascertain on account of the varying plate sensitivity in the photographic infrared. The absence of the overtones of the induced dipole spectrum is, however, not surprising if it is remembered that some of the reasons for the slow decrease of intensity in the series of quadrupole bands do not apply to dipole bands.

The first discussion of the  $H_2$  quadrupole spectrum (6) was made with a view to detecting the large amounts of  $H_2$  assumed to be present in the atmospheres of the major planets. The knowledge now obtained of the correct wave lengths and of the intensity of absorption should help in solving the problem of  $H_2$  in planetary atmospheres. Unfortunately planetary spectra thus far available have a much lower resolution than the laboratory spectra used here and do not show the quadrupole lines. Since the  $H_2$  lines are very sharp the amount of  $H_2$  used here can be considered as an upper limit to the amount of  $H_2$  in planetary atmospheres only if the same resolution is employed.

It would be interesting to ascertain whether similar quadrupole rotation-vibration spectra are observable for  $O_2$ ,  $N_2$ , and other diatomic molecules. However it would be difficult to predict the intensities of these spectra. At any rate the decrease of intensity in the series of overtones would be expected to be faster and since the fundamentals would be practically unobservable because of overlapping by the dipole transitions of  $H_2O$  and  $CO_2$  it seems likely that much longer absorbing paths are required than for  $H_2$ . In the case of  $N_2$ , Goldberg (5) has looked for the 2-0 band in the solar spectrum taken at very low sun with an equivalent path of about 50 km. atm. but did not find any absorption.

### Acknowledgments

The experimental part of this investigation was carried out at the Yerkes Observatory. Grateful thanks are due to the authorities of Yerkes Observatory for making this work possible. This investigation could not have been carried out if it had not been for the superior quality of the mirrors made by Mr. Fred Pearson in the Optical Shop of Yerkes Observatory.

### References

1. BARRELL, H. and SEARS, J. E. *Trans. Roy. Soc. (London)*, A, 238: 1. 1939.
2. BERNSTEIN, H. J. and HERZBERG, G. *J. Chem. Phys.* 16: 30. 1948.
3. CRAWFORD, M. F., WELSH, H. L., and LOCKE, J. L. *Phys. Rev.* 75: 1607. 1949.
4. DUNHAM, J. L. *Phys. Rev.* 41: 721. 1932.
5. GOLDBERG, L. Private communication.
6. HERZBERG, G. *Astrophys. J.* 87: 428. 1938.
7. HERZBERG, G. *In Atmospheres of the earth and planets*, edited by G. P. Kuiper, p. 346. University of Chicago Press. 1949.
8. HERZBERG, G. *Nature*, 163: 170. 1949.
9. HERZBERG, G. *Molecular spectra and molecular structure. I. Spectra of diatomic molecules*. 2nd ed. D. Van Nostrand Company, Inc., New York. 1950.
10. JAMES, H. M. and COOLIDGE, A. S. *Astrophys. J.* 87: 438. 1938.
11. JEPPESEN, C. R. *Phys. Rev.* 44: 165. 1933.
12. MIZUSHIMA, M. *Phys. Rev.* 76: 1268. 1949.
13. TEAL, G. K. and MACWOOD, G. E. *J. Chem. Phys.* 3: 760. 1935.
14. UREV, H. C. and TEAL, G. K. *Rev. Modern Phys.* 7: 34. 1935.
15. WELSH, H. L., CRAWFORD, M. F., and LOCKE, J. L. *Phys. Rev.* 76: 580. 1949.



## A SATURATED CORE RECORDING MAGNETOMETER<sup>1</sup>

BY D. C. ROSE AND J. N. BLOOM

### Abstract

A recording magnetometer operating on the saturated core inductor principle has been constructed. An inverse feed-back system supplies a current to neutralize the field being measured. The neutralization is such that the sensitive element is maintained within 2 or 3 gammas of zero field. The feed-back current is measured by a recording milliammeter. Using a feed-back coil of suitable dimensions, the record gives a direct measure of the field.

### Introduction

In this instrument the saturated core method of measuring small magnetic fields has been adopted to make a recording instrument of high accuracy and stability. The instrument is absolute, in that the field is calculated from the current in a coil of known dimensions. Though the instrument was developed to record variations in the earth's magnetic field, it should be useful for any problem where fields from a few gammas to a few hundred gammas are to be measured.

The saturated core method was applied as early as 1931 for measuring fields, and was used in a magnetic compass (3). It was developed by Vacquer, Simon, and Hull (5) as an airborne instrument. During the recent war the principle was used extensively in a magnetic detector for various applications, for example, the U.S. Navy Magnetic Airborne Detector.

### Principle of Operation

The sensitive element of the instrument consists of a strip of high permeability alloy such as permalloy or  $\mu$ -metal. The strip used in this instrument is 0.006 in. thick, about  $2\frac{1}{2}$  in. long, and  $1/8$  in. wide. A wide variation in these dimensions makes little difference in the sensitivity provided the coils are suitably designed. This strip of permalloy is excited by an alternating field of sufficient strength to be well over saturation on the peak of each half cycle. The excitation is supplied by a coil about equal in length to the strip. Fig. 1 shows a sketch of the sensitive element of the instrument. The inner coil is the exciting coil, the outer being for inverse feedback.

If the permalloy strip is excited by an alternating voltage of pure wave form, the resulting current wave will be distorted by the shape of the B-H curve. If there is no field other than the exciting field, the distorted wave will be symmetrical on the + and - sides of the zero axis, so will contain only odd harmonics. If the instrument is in an external field (the earth's field or the field to be measured) the exciting voltage will saturate the core more easily in one

<sup>1</sup> Manuscript received November 9, 1949.

Contribution from the Division of Physics, National Research Laboratories, Ottawa, Canada.  
Issued as N.R.C. No. 2081.

direction than in the other. The wave form then will not be symmetrical about the zero axis and will contain even harmonics the strength of which is a function of the external field to be measured.



FIG. 1. Schematic diagram of sensitive element.

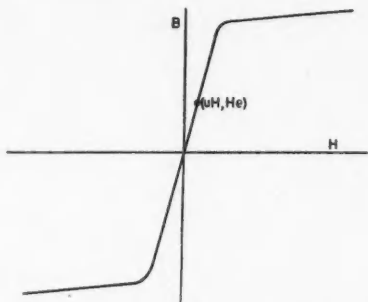


FIG. 2. The  $B$ - $H$  curve, idealized with no hysteresis.

This can be shown analytically. If one considers the ideal case where the hysteresis loop has no area, and the curve has corresponding equal values in the first and third quadrants, the magnetization curve (Fig. 2) can be represented by an equation in the form of a power series

$$B' = a_1 H' + a_3 H'^3 + a_5 H'^5 + \dots, \text{ etc.}$$

Applying a small external field (so small that it is on the linear part of the  $B/H$  curve) is equivalent to shifting the axis an amount

$$B' = B + uH_e$$

$$H' = H + H_e, \text{ where } H_e \text{ is the small external field.}$$

$H$  is applied as a sinusoidal magnetizing force  $H_0 \sin \omega t$ , so the equation becomes

$$\begin{aligned} B + uH_e &= a_1(H_0 \sin \omega t + H_e) \\ &+ a_3(H_0 \sin \omega t + H_e)^3 \\ &+ a_5(H_0 \sin \omega t + H_e)^5 + \dots, \text{ etc.} \end{aligned}$$

This equation may be reduced to the form

$$B = -uH_e + P_0 + P_1 \sin \omega t + P_2 \cos 2\omega t + P_3 \sin 3\omega t + \dots$$

where the  $P$ 's are power series in  $H_0$  and  $H_e$ . The  $P$ 's with even subscripts have no terms which do not depend on  $H_e$ . The problem then is to select an even harmonic or group of harmonics, and a measure of the amplitude of these

gives a measure of  $H_e$ . Experience shows that when the second harmonic is chosen the intensity of this harmonic is roughly proportional to  $H_e$  over a considerable range.

In our instrument the field is measured by amplifying the second harmonic, rectifying it to a direct current, and feeding it back through the outer coil (Fig. 1). The outer coil is of known dimensions and is sufficiently long to give a reasonably uniform field over the length of the permalloy strip. The feed back neutralizes the external field  $H_e$  and, if the feed-back constant is sufficiently high to leave the residual field negligibly small, the field is measured by the current and dimensions of the feed-back coil. There are two well known ways of selecting appropriate even harmonics. In the first only filters are used. In the second two strips of  $\mu$ -metal are used instead of one. These are placed side by side, each with an exciting coil, connected in opposition. A pickup coil on each connected in series, or one coil surrounding both, will pick up the harmonics not balanced out by the opposition connection of the primaries. Both methods are practical, but in the instrument described here the method wherein the second harmonic is separated by high quality filters was chosen. This has the advantage that the sensitive head is geometrically simple, and only one winding (apart from the feed-back coil) is required. It has the disadvantage that special filters have to be built.\* The U.S. Navy M.A.D. equipment (4) uses this single core method, and the design used here is a modification of theirs.

### The Oscillator, Filters, Amplifier, and Phase-Sensitive Detector

The exciting frequency chosen was approximately 1000 c.p.s. (Actually the filters as constructed are peaked about 990 cycles and the oscillator is tuned to this.) As the same coil is used for excitation and for pickup the exciting voltage must have no second harmonic and must be very stable. Fig. 3 shows the circuit diagram of the oscillator and filters. The oscillator is a well known type wherein the feed-back circuit contains a resistance capacity network, which fixes the frequency. After amplification the exciting voltage is fed to the coil through the 1000 cycle filter. The second harmonic is selected by connecting an appropriate filter across the exciting coil in parallel with the 1000 cycle filter. The values of the filter components are as indicated. These filters were manufactured to our specifications by the United Transformer Company. The 2000 cycle filter has an impedance transformation with an actual voltage step up of about six. Both filters were designed so that there would be a correct impedance match and the exciting coil was wound to give the correct impedance (1000 ohms at 1000 cycles) with the permalloy strip in place. Care was also taken to match the loads on the other sides of the filters. The 1000 cycle filter attenuates 2000 cycles by about 80 db. The oscillator produces only a fraction

\*Another successful recording instrument using the two core method of separating the required harmonics has been developed by P. Serson of the Dominion Observatory, Ottawa. We wish to thank Mr. Serson for showing us the details and results of the use of his instrument. Double-core instruments had also been made in the N.R.C. laboratory by Ralph Bailey (1) for geomagnetic prospecting.

of 1% of second harmonic. The sensitivity of the system varies with different coils and  $\mu$ -metal strips. An average value at the output of the 2000 cycle filter is about 25  $\mu$ v. per gamma of  $H_e$ . With the circuit as used any spurious second harmonic that might get through from the oscillator would be about  $10^{-7}$  v. so the sensitivity is not limited by unwanted 2000 cycle from the exciting voltage.

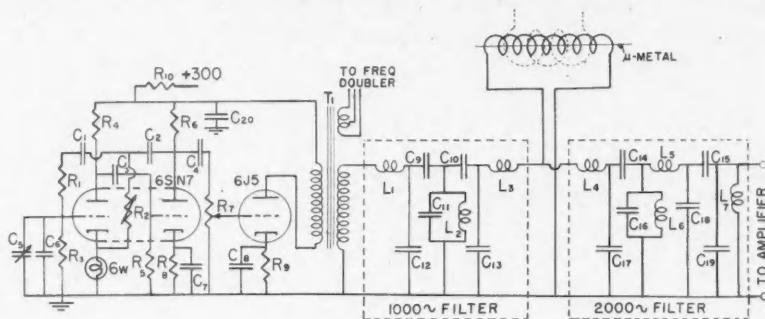


FIG. 3. Oscillator and filters.

$R_1$ —0.25 meg.  
 $R_2$ —1000 ohm, variable  
 $R_3$ —0.25 meg.  
 $R_4$ —56K  
 $R_5$ —0.47 meg.  
 $R_6$ —39K  
 $R_7$ —0.5 meg., variable  
 $R_8, R_9$ —1.5K  
 $R_{10}$ —5.6K

1000 cycle filter  
 $C_9, C_{10}$ —1164.1  $\mu$ mf.  
 $C_{11}, C_{12}, C_{13}$ —14788  $\mu$ mf.  
 $L_1$ —1.591 h.  
 $L_2$ —1.498 h.  
 $L_3$ —1.591 h.

$C_1$ —637  $\mu$ mf.  
 $C_2, C_3, C_4$ —0.1  $\mu$ f.  
 $C_5$ —100  $\mu$ mf., variable  
 $C_6$ —620  $\mu$ mf.  
 $C_7, C_8$ —10  $\mu$ f.  
 $C_{10}$ —20  $\mu$ f.

$T_1$ —Primary, 10,000 ohms  
 —Secondary, (a) 20,000 ohm CT  
 (b) 1000 ohm

2000 cycle filter

$C_{14}$ —1994  $\mu$ mf.  
 $C_{15}$ —126.2  $\mu$ mf.  
 $C_{16}$ —98474  $\mu$ mf.  
 $C_{17}$ —1994  $\mu$ mf.  
 $C_{18}$ —871  $\mu$ mf.  
 $C_{19}$ —1481  $\mu$ mf.  
 $L_4$ —1.591 h.  
 $L_5$ —6.366 h.  
 $L_6$ —0.0638 h.  
 $L_7$ —3.988 h.

The amplifier circuit is shown in Fig. 4. The 2000 cycle filter attenuates 1000 cycles by 80 db. relative to the 2000, and an additional 30 db. rejection of the 1000 cycle signal is achieved by a tuned feed-back network in the second stage of the amplifier. This network, described by Valley (6, pp. 398-408), has a high inverse feedback except at the desired frequency. In spite of the attenuation a certain amount of 1000 cycle gets through. This, with the usual noise, fixes the limit of sensitivity of the instrument.

There is an optimum value of the exciting voltage, a typical curve being shown in Fig. 5. The voltage used is about 3.8. The 2000 cycle filter and amplifier reduce this, relative to the 2000 cycle signal, by  $80 + 30 = 110$  db. or a factor of about  $3.2 \times 10^5$  in voltage. There will be, therefore, about 12  $\mu$ v.

of 1000 cycle unwanted, to be compared with the wanted signal of  $25 \mu\text{v}$ . per gamma. This 1000 cycle residual can be seen when the sensitive head is turned to null field, the output of the amplifier being displayed on a cathode ray oscilloscope.

The circuit of the phase sensitive detector is shown in Fig. 4. Sensitivity in direction of the d-c. output to the phase of the 2000 cycle signal is necessary

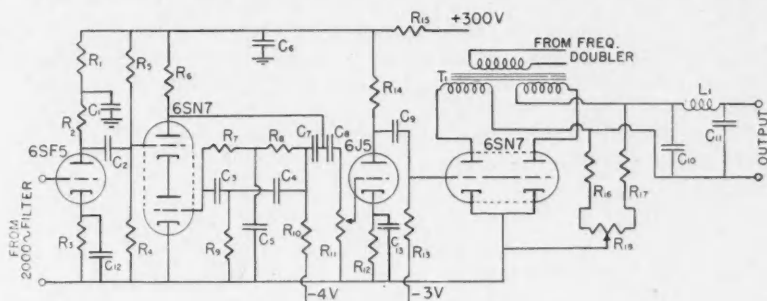


FIG. 4. Amplifier, detector, and filter.

$R_1$ —22K  
 $R_2$ —150K  
 $R_3$ —5.6K  
 $R_4$ —0.9 meg.  
 $R_5$ —2.2 meg.  
 $R_6$ —120K  
 $R_7, R_8$ —0.12 meg.  
 $R_9$ —56K  
 $R_{10}$ —2.2 meg.  
 $R_{11}$ —0.5 meg.  
 $R_{12}$ —2.2K  
 $R_{13}$ —0.12 meg.  
 $R_{14}$ —56K  
 $R_{15}$ —5.6K.

$R_{16}, R_{17}, R_{18}$ —1K  
 $C_1$ —4  $\mu\text{f}$ .  
 $C_2$ —0.01  $\mu\text{f}$ .  
 $C_3, C_4$ —686  $\mu\text{f}$ .  
 $C_5$ —1372  $\mu\text{f}$ .  
 $C_6$ —4  $\mu\text{f}$ .  
 $C_7$ —0.25  $\mu\text{f}$ .  
 $C_8, C_9$ —0.01  $\mu\text{f}$ .  
 $C_{10}, C_{11}$ —4  $\mu\text{f}$ .  
 $C_{12}, C_{13}$ —10  $\mu\text{f}$ .  
 $L_1$ —10 h.  
 $T_1$ —Primary, 10,000 ohm  
 —Secondary, 45000 ohm each

to make the sense of the feed-back current vary as the field passes through null. The circuit for this is a modification of that used by Cosens (2). A reference voltage of the same frequency and of constant relative phase to the signal voltage is required. This is obtained from the 1000 cycle oscillator by a simple

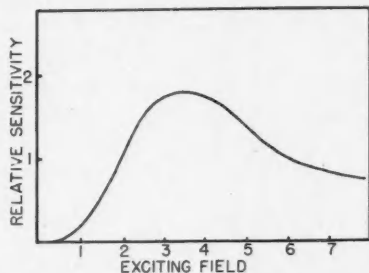


FIG. 5. Relative sensitivity of sensitive element at different exciting voltages.

circuit (not shown). It is a conventional frequency doubler using a push-pull rectifier to give 2000-cycle pulses. These are amplified, the wave form being purified considerably by a parallel-tuned circuit of high  $Q$ . A very pure wave form is not essential here. For maximum sensitivity the reference voltage must be in phase (or  $180^\circ$  out of phase, depending on the direction of  $H_0$ ) with the signal voltage. This is accomplished by a fine adjustment of the oscillator frequency to take advantage of phase shifts in the filters and amplifiers.

The over-all gain of the amplifier from the 2000 cycle filter output to the output of the phase sensitive detector is of the order of 60 db. A simple low pass filter (critical frequency about 35 c.p.s.) is included after the detector to give a smooth d.c. If this is connected directly to a meter such as an Esterline Angus Recorder of 1 ma. full scale, a sensitivity of the order of 100 gammas for the full scale of the meter is ordinarily achieved. The instrument thus far, if calibrated frequently, would make a complete measuring instrument in itself, but it would not be stable in sensitivity over long periods. For convenience in design the oscillator, filters, amplifier, phase sensitive detector, low pass output filter (and power supply for these), are included in one chassis. The feed-back amplifier and servo system are mounted separately with their power supply in another chassis. This design was followed so that the instrument could be used independently without feedback, and also because it was found advisable to use a separate power supply for the feed-back section of the instrument.

### The Feed-back System

In principle, the rectifier output is fed back through a coil surrounding the sensitive element (the outer winding in Fig. 1). It is fed back in such a direction as to neutralize the field almost completely, leaving the sensitive element in a very weak field, but still sufficient to supply the feed-back signal. If the residual field is small enough to be neglected the current in the feed-back solenoid gives a measure of the field. The design of such a system has definite limitations, owing to the requirements of available recording meters and inherent instabilities of inverse feed-back systems.

If the filtered output of the phase sensitive detector were fed back directly it would make a complete instrument. However, with the circuit as shown, the output at this stage would make the feed-back ratio too small to meet the objective of making the residual error signal negligible.

A balanced d-c. amplifier was considered but discarded on the grounds that it adds an objectionable source of zero drift. The only balanced component at present which might cause zero drift is the phase sensitive rectifier. We found no way of eliminating all circuits which might cause drift, but, with the circuit used, this has been reduced to a negligible value.

To make recording of the feed-back current readily possible the current available to cover the selected range in field intensity should be 1 ma. This will operate an Esterline Angus Recorder. Leeds and Northrup and Brown

make more sensitive recorders and these have been used with the instrument but it was considered desirable to design it for use with either type. One milli-ampere was therefore chosen as the feed-back current to neutralize a field of 1000 gammas. To reduce to a minimum, errors due to the residual field, the feed-back ratio  $N$  should be as high as possible. At least 100 was considered a good objective.  $N$  is defined by the equation

$$H = H_F \left( 1 + \frac{1}{N} \right),$$

where  $H$  is the field to be measured and  $H_F$  is the neutralizing field produced by the current in the feed back coil.

An attempt was made to amplify the 2000 cycle signal by about another 10 db. and connect the output of the phase sensitive detector through an appropriate filter directly to the feed-back coil. For this plan the filter design is a difficult problem. It must block the 2000 cycle current completely; it must have a reasonably low impedance to pass the 1 ma. Yet the whole system must be stable. A consideration of the stability requirement and some experimenting led to the conclusion that a high value of  $N$  could not be obtained in this way without using capacities that were much too high to be practical, and specially constructed inductances. One instrument was built and operated successfully for several months but the best value of  $N$  achieved under practical conditions was about 30.

### The Servo System

A servo feed-back system as shown in Fig. 6 was found successful. The principle of operation is well known. The d-c. voltage from the filtered output of

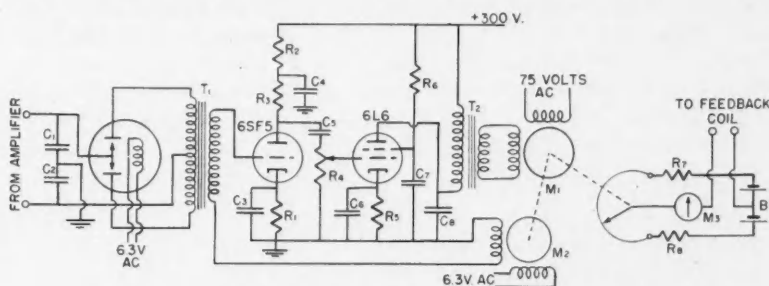


FIG. 6. Servo amplifier and feed back circuit.

- |                             |                           |
|-----------------------------|---------------------------|
| $R_1$ —5.6K                 | $C_1, C_2$ —0.25 $\mu$ f. |
| $R_2$ —22K                  | $C_3$ —10 $\mu$ f.        |
| $R_3$ —150K                 | $C_4$ —4 $\mu$ f.         |
| $R_4$ —0.5 meg.             | $C_5$ —0.01 $\mu$ f.      |
| $R_5$ —0.3K                 | $C_6$ —10 $\mu$ f.        |
| $R_6$ —22K                  | $C_7$ —4 $\mu$ f.         |
| $R_7, R_8$ —100 ohms        | $C_8$ —0.01 $\mu$ f.      |
| $M_1$ —servo motor          | $T_1$ —UTC A-11           |
| $M_2$ —damping generator    | $T_2$ —Primary, 3500 ohms |
| $M_3$ —recording millimeter | Secondary, 900 ohms       |
|                             | B—1.5 v. dry cells.       |



the sensitive detector is broken up into pulses by a vibrating reed chopper or converter (a Brown converter is used). The pulses are at 60 cycles and after amplification drive a two-phase servo motor. The servo motor drives a potentiometer which controls current to the feed-back coil from a battery circuit as shown. A Diehl Manufacturing Company 60 cycle a-c. control motor was used, geared to a General Radio potentiometer type 214A with a gear ratio of 25 to 1. The potentiometer has a resistance of 500 ohms and the winding is fine enough to give steps of less than 2 gammas. Potentiometers of this type have been operated for several months with no trouble. They have the advantage that they are cheap and easy to replace. A precision potentiometer is not required since the feed-back current is measured independently. The amplification, when all available gain is used, is such that the servo motor will start in either direction with a signal of considerably less than 1 gamma.

The servo motor used with the gear train and potentiometer has inertia and torque characteristics which make it unstable unless there is auxiliary damping. Damping is achieved easily by another small two-phase servo motor (mounted on the same shaft as the driving motor) connected to act as an induction generator. It is excited from the 60 cycle power supply and the output fed back into a winding of the converter transformer. The damping can be controlled by the exciting voltage. The damping generator is a Pioneer Bendix type CK-2 designed for 400 cycles but works very well at reduced voltages at 60 cycles. The design of these servo parts is not critical; several mock up systems were made using assorted types of motors obtained from war surplus. The over-all sensitivity of the instrument is such that the servo mechanism will balance it so that the residual field at the sensitive element is about 2 gammas. When using this servo system the definition of the feed-back ratio in the previous section does not apply, but the residual error is always small. Used with an Esterline Angus recording meter set for 1000 gammas full scale the instrument is more accurate than the meter. With a Brown or Leeds and Northrup recorder, precision up to the limit of the magnetometer can be obtained.

### Stability

With the high inverse feed-back ratio used, the gain of the amplifier can change considerably without appreciable change in the accuracy of recording. Apart from component failures the only changes which can affect the output seriously are a change in frequency of the oscillator and a change in the balance of the phase sensitive detector. The oscillator circuit was chosen because of its stability in frequency and purity of wave form. Its power supply is regulated by VR tubes, and experience shows that its frequency is very stable.

Five complete instruments have been made and operated continuously for varying periods up to several months. The instruments have been operated successfully without adjustment for periods up to two months but for continuous use a regular tune-up as described below is advisable every two or three



weeks. Once familiarity with the instrument is achieved the adjustments take only a few minutes.

### Adjustments

In tuning up the instrument the feed-back control potentiometer ( $R_2$  in Fig. 3) on the oscillator section is reduced until the circuit will just oscillate steadily. The gain control ( $R_7$  in Fig. 3) feeding the exciting coil amplifier is then adjusted until the voltage across the exciting coil is 3.8 v. With a signal corresponding to about 50 gammas and the servo amplifier disconnected, the frequency of the oscillator should be adjusted until there is a maximum signal in the 2000 cycle amplifier. The frequency is adjusted by the small variable condenser ( $C_5$  in Fig. 3). This tunes the circuit to the 2000 cycle filter system. The 1000 cycle filter is relatively broader. Therefore the frequency is correct for both if correct for the 2000 cycle filter. Phasing of the reference voltage and the signal to the phase sensitive detector is the next adjustment. The horizontal and vertical plates of a cathode ray oscilloscope are connected to the two inputs of the detector. Test point terminals are brought out for this. The gains should be adjusted to give a good pattern, then the frequency of the main oscillator readjusted slightly until the pattern is as nearly as possible a straight line. This adjustment may put the oscillator slightly off the peak frequency of the filters, but the gain is sufficiently high that this is not important. The next adjustment is to balance the phase sensitive detector. Connect the servo amplifier and turn the gain control ( $R_{11}$  in Fig. 4) of the 2000 cycle amplifier to zero. Adjust the balancing potentiometer ( $R_{18}$  in Fig. 4) until the servo motor remains still in any position. All these adjustments except phasing the detector can be made with nothing more than a high resistance a-c. voltmeter. An indicating voltmeter built into the instrument is connected across the filtered output of the phase sensitive detector. If the instrument is used without the feed-back system this meter indicates the field measured. If the servo feed-back system is in operation this meter should always read so nearly zero that the current is not observable as different from zero. With practice, phasing may be accomplished by using this meter without a cathode ray oscilloscope, but a 3 in. oscilloscope is very useful in making the adjustments quickly.

When the above adjustments are complete, the gain of the 2000 cycle amplifier and the servo amplifier should both be turned up to give a good torque on the motor without instability. Too high a gain will cause the system to oscillate. The perfection of adjustment can be tested at any time by feeling the torque on the servo motor gears when they are given a small displacement from the balanced position.

### Design of Sensitive Element

The handling and mounting of the permalloy strip is very important in making successful magnetometers. This is particularly so if wide changes in sensitivity are to be avoided. The metal used was Allegheny  $\mu$ -metal supplied in sheets 6 mils thick. The strips were cut and heat treated in the laboratory.

The heat treatment must be carried out accurately according to instructions of the suppliers. After heat treatment the strips must be handled very carefully so that no bending or strains are introduced. Otherwise the desired magnetic properties are lost.

The strip is mounted in the center of a lucite bobbin on which the exciting coil is to be wound. The bobbin is made accurately in two halves (see Fig. 1), being split longitudinally through its axis. Two slots are milled in the two halves slightly wider than the strip and making a total thickness of slot of 8 mils, 2 mils greater than the strip thickness. To assemble, the strip is fixed in the slot in one half of the bobbin with a tiny spot of soft wax at its center. The two halves are then pressed together and the coil wound.

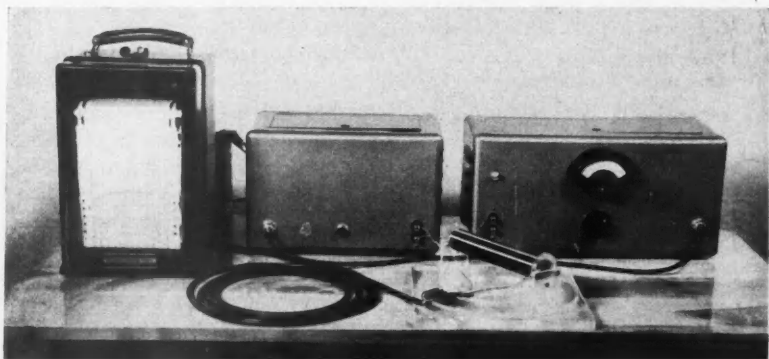


FIG. 7. Complete magnetometer showing oscillator and amplifier box, servo box and recorder, with sensitive element in foreground.

The wax holds the strip at its center, the ends being free to expand and contract in the slot, but not to move laterally, by more than the 2 mils clearance. The feed-back coil is wound on a lucite cylinder about 9 in. long. The cylinder has an axial hole just large enough to hold the bobbin which is placed at the center of the coil and stuck in with a little coil dope or wax.

This design gives very satisfactory results. Tests were made for temperature variation of sensitivity, the head being placed in a box where the temperature was changed between 0°F. and 60°F. When the detector is connected directly to the meter without feed-back, a change in sensitivity of 0.3% per Fahrenheit degree was noted but with the feed-back connected no temperature effect could be observed.

Fig. 7 shows a photograph of a complete instrument. The coil here is designed for recording variations in declination of the earth's magnetic field. To do this it is set in the usual position, horizontally at right angles to the steady horizontal component. The recorded variations will then be  $H \sin D$ .

where  $D$  is variation in declination angle. To use the instrument to record variations in horizontal or vertical force some additional system to neutralize the steady component must be included. Fig. 8 is a sample record of a magnetic storm.

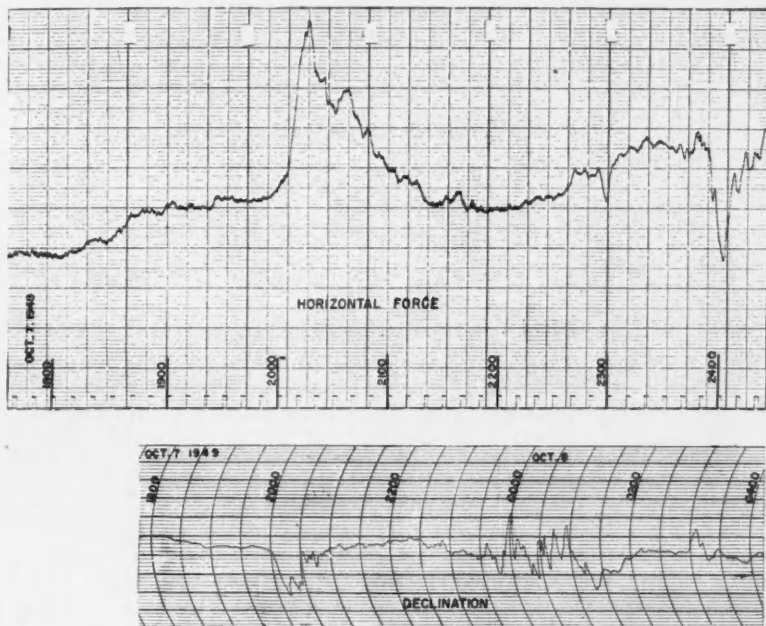


FIG. 8. Records of a magnetic disturbance taken with Leeds and Northrup Speedomax (top) and Esterline Angus millimeter recorders. Time marks are G.M.T. (The Leeds and Northrup recorder paper drive had been altered. Therefore the time marks do not fit the paper scale.) Full scale in each case represents 1000 gammas.

### References

1. BAILEY, R. *Can. J. Research*, F, 26: 523. 1948.
2. COSENS, C. R. *Proc. London Phys. Soc.* 46: 818. 1934.
3. THOMAS, H. P. U.S. Patent No. 2,016,977. Dec. 1, 1931.
4. U.S. War Department, U.S. Navy Department, and Air Council of the United Kingdom. Handbook of maintenance and instructions for AN/ASQ-3A equipment. Office of Publication Board, Department of Commerce, Washington, D.C.
5. VACQUER, V., SIMON, R. F., and HULL, A. W. *Rev. Sci. Instruments*, 18: 483. 1947.
6. VALLEY, G. E. and WALLMAN, H. *Editors*. Vacuum tube amplifiers. Mass. Inst. Technol. Radiation Lab. Ser. No. 18. McGraw-Hill Book Co., Inc., New York. 1948.

## FORMATION OF RADIOACTIVE SURFACE FILMS ON MINERALS<sup>1</sup>

By T. G. CHURCH

### Abstract

With the requisite chemical treatment, specific minerals will assume a surface radioactivity by undergoing reactions with radioactive ions in solution. It is essential that the mineral have a suitably tarnished or coated surface, for in general no exchange will occur on a fresh surface. It is suggested that the radioactivity so induced could be used in conjunction with a mechanical device to separate and concentrate the valuable minerals in an ore, or to control hydro-metallurgical plant processes.

### Introduction

This paper describes experiments performed to determine whether mineral surfaces can be made radioactive by undergoing exchange reactions with radioactive ions in solution. Such radioactive coatings, if selective, would serve as a means of differentiating between minerals in an ore, and enable them to be separated by a suitable mechanical ore sorting device actuated by a Geiger counter. Thus the metallurgist would have at his disposal an additional means of beneficiating certain ores.

F. Paneth (1) has pointed out that natural minerals offer great resistivity to exchange reactions as compared with laboratory-prepared compounds of the same chemical formula. His work clearly indicated that (except in rare cases) no exchange could be expected on the fresh surface of a primary mineral. There remained, however, the possibility that tarnished or weathered mineral surfaces might react more readily. Therefore, in the present work attempts were made to coat the mineral with an adherent film of a substance which would exchange readily with active ions in dilute acid solutions. The experiments were of a preliminary nature only, to test the feasibility of the method. It is anticipated that every ore will present a somewhat different problem.

### Experimental

#### *General*

Synthetic ores were used; the constituent minerals were clean, well crystallized pieces that offered a surface for counting of about 15 mm.<sup>2</sup> Fragments of quartz and feldspar representative of gangue minerals were carried through the same treatments given the ore mineral. A few pieces of each mineral were placed in a beaker containing a conditioning agent designed to produce a surface coating. After the conditioning period the pieces were washed and transferred to the active solution for the required time. Then, after washing and drying, the activity of each piece was measured with a 110 volt a.c. operated Geiger

<sup>1</sup> Manuscript received in original form August 15, 1949, and, as revised, December 1, 1949. Contribution from the Research Division, Atomic Energy Project, National Research Council, Chalk River, Ont. Issued as N.R.C. No. 2079.

Probe Monitor fitted with an end-on counter having a window of 2.7 mgm. per cm.<sup>2</sup> thickness. The samples were placed 6 mm. below the window. Activities were recorded as counts per min. per cm.<sup>2</sup> of mineral surface.

#### *Galena (PbS)*

Galena oxidizes fairly readily in moist air to give a surface coating of lead sulphate. For this reason  $S^{35}$  in the form of  $SO_4^{2-}$  in acid solution was used in attempts to activate the surface by exchange reaction. To produce the desired coating the freshly broken mineral was given a pretreatment with dilute nitric acid before transferring to the active solution. The lead sulphate coating was found to be firm and adherent.

No exchange was observed to occur on the fresh surface of the galena. As oxidation of the surface progressed, exchange took place more and more readily. Even when only a slight tarnishing was apparent, the surface assumed a quite high activity after a few minutes in the active solution. Representative tests are recorded in Table I.

TABLE I  
EXCHANGE OF  $S^{35}O_4^{2-}$  IN SOLUTION WITH GALENA SURFACE

Conditioning treatment	Appearance of coating	Time in active solution (1 $\mu$ c./cc. in 0.01% $H_2SO_4$ )	Activity, counts/min./cm. <sup>2</sup>	
			Galena	Gangue
1% $HNO_3$ quick rinse	Bright, no tarnish	3 min. to 20 hr.	Nil	Nil
1% $HNO_3$ for 1 hour	Slight tarnish	10 min.	4,200	200
1% $HNO_3$ for 20 hr.	Visible coating of $PbSO_4$	10 min.	9,800	350
1% $HNO_3$ for 20 hr.	Heavy coating of $PbSO_4$	20 hr.	31,500	2,100

In these tests the active solution contained added (inactive) sulphuric acid, thus lowering the specific activity of the  $S^{35}$ . When only the tracer  $SO_4^{2-}$  was present a much higher activity on the galena surface was obtained, but in this case some  $S^{35}O_4^{2-}$  was absorbed on the quartz and feldspar, so that the ratio of the activities, galena/gangue, was very little higher than when inactive  $SO_4^{2-}$  was present. Representative tests with carrier-free  $SO_4^{2-}$  are shown in Table II.

#### *Pyrite (FeS)*

Some tests were carried out on pyrite under the same conditions as for galena. The oxidation of the surface in this case produces a coating of ferric oxide instead of sulphate, as any sulphate formed goes into solution. Consequently, the mineral surface could not be made radioactive by using  $S^{35}O_4^{2-}$ .

#### *Apatite ( $CaF_2 \cdot 3Ca_3P_2O_8$ )*

It was found that no exchange occurs between the surface of the apatite and  $P^{32}$  as phosphate in acid solution. Attempts to produce a coating on the mineral

TABLE II  
EXCHANGE OF  $S^{35}O_4^{=}$  IN SOLUTION WITH GALENA SURFACE

Conditioning treatment	Appearance of coating	Time in active solution (2 $\mu$ c./cc. in 0.1% $HNO_3$ )	Activity, counts/min./cm. <sup>2</sup>	
			Galena	Gangue
1% $HNO_3$ for 1 hour	Slight tarnish	10 min.	3,150	$SiO_2$ -2800 feldspar-4200
1% $HNO_3$ for 20 hr.	Visible coating of $PbSO_4$	10 min.	15,400	3,000
1% $HNO_3$ for 20 hr.	Heavy coating of $PbSO_4$	20 hr.	140,000	3,000

that would exchange with  $P^{32}O_4^{=}$  in acid failed. This was to be expected since calcium phosphate is soluble in dilute acid. It was found, however, that dilute sulphuric acid produces a relatively insoluble coating of calcium sulphate on the apatite, and that this coating exchanges very readily with  $S^{35}O_4^{=}$  in solution. In this way the mineral surface could be given a high activity. Some tests under rather extreme conditions are shown in Table III.

TABLE III  
EXCHANGE OF  $S^{35}O_4^{=}$  IN SOLUTION WITH APATITE SURFACE

Conditioning treatment	Appearance of coating	Time in active solution (5 $\mu$ c./cc. in 0.02% $H_2SO_4$ )	Activity, counts/min./cm. <sup>2</sup>	
			Apatite	Gangue
Warm conc. $H_2SO_4$ for 2 hr. several water washes.	Very thick coating of $CaSO_4$	15 min.	2,100	Nil
"	"	48 hr.	126,000	350
10% $H_2SO_4$ for 20 hr., then several water washes.	"	48 hr.	260,000	350

#### Cobalt Minerals

Some work has been done on cobalt minerals. Tests were carried out on smaltite ( $CoAs_2$ ), pentlandite ( $Fe, NiS$ ) and niccolite ( $NiAs$ ), using  $Co^{60++}$  as the active ion. Smaltite generally contains some nickel diarsenide and niccolite has many impurities, including cobalt. Owing to their different chemical compositions and physical characteristics, it is difficult to coat the three minerals uniformly. However, digestion with boiling 3*N* sodium hydroxide solution produces a surface film of hydrated oxides. Then, after standing in slightly acid active solution with a strength of 1  $\mu$ c. per cc. for some hours, the tarnished minerals become radioactive. Some of this induced activity seems to be due to surface absorption and some to ion exchange. Probably close pH

control and the use of suitable amounts of carrier would reduce straight absorption to a minimum. But, regardless of the mechanism of these effects, the activity measured is a definite characteristic of each mineral and the differences in the activities of each are quite marked.

### Conclusion

We may say that certain mineral surfaces can be made radioactive by exchange with active ions in solution, provided that the surface is coated with a slightly soluble compound produced by weathering or by chemical treatment. The number of radioisotopes available should make the method generally applicable. The experimental data which has been presented is rather crude and scanty but it is hoped that sufficient work has been done to indicate the general method to those who may be interested.

### Reference

1. PANETH, F. Radio-elements as indicators. McGraw-Hill Book Company, Inc., New York. 1928.

ELECTRON DIFFUSION IN A SPHERICAL CAVITY<sup>1</sup>

BY A. D. MACDONALD AND SANBORN C. BROWN

## Abstract

The diffusion equation for electrons in a nonuniform field is solved and the breakdown condition derived. The breakdown condition is expressed in such a manner that an effective characteristic diffusion length  $\Lambda_e$  is determined; the meaning of  $\Lambda_e$  expresses the equivalent characteristic diffusion length for uniform electric fields. From the experimental breakdown fields, in which the electric field is uniform,  $\Lambda_e$  is determined and used to predict theoretical breakdown curves for the nonuniform cases. Theory and experiment are compared, the agreement verifying the correctness of the approach.

Electrical breakdown of a gas at microwave frequencies has been considered theoretically and experimentally for the case in which the electric field is uniform (2, 5, 6). It is sometimes important to consider cases in which the electric field is not uniform in order that the shape of the volume from which diffusion takes place may be varied. The case of a cylindrical cavity of arbitrary length has been solved by Herlin and Brown (3), and the procedure of this paper is similar to theirs. The diffusion equation for electrons in a non-uniform field is solved and the breakdown condition is expressed in such a manner that an effective characteristic length  $\Lambda_e$  is determined; the meaning of  $\Lambda_e$  expresses the equivalent characteristic diffusion length for uniform electric fields. From the experimental breakdown fields measured using uniform fields  $\Lambda_e$  is determined and used in the theories developed in References (5) and (6) to predict theoretical breakdown curves for the nonuniform case—these curves are compared with experiment.

## I. Diffusion Theory

The differential equation to be solved for the characteristic diffusion length of electrons in a gas is

$$\Delta^2\psi + \zeta E^2\psi = 0, \quad (1)$$

where  $\psi = Dn$ , the electron diffusion current density potential;  $D$  is the electron diffusion coefficient;  $n$  is the electron concentration;  $E$  is the r.m.s. value of the electric field, and  $\zeta$  is defined by the equation

$$\zeta = \nu/DE^2,$$

$\nu$  being the ionization rate per electron.

The boundary condition on Equation (1) is that the electron concentration and thus  $\psi$  go to zero within a mean free path of the walls of the metal cavity.

<sup>1</sup> Manuscript received November 18, 1949.

Contribution from the Physics Department, Dalhousie University, Halifax, N.S., Naval Research Establishment, Halifax, N.S., and Research Laboratory of Electronics, Massachusetts Institute of Technology. This work was supported in part by the Signal Corps, the Air Material Command, and O.N.R.



$\zeta$  may be expressed as a function of  $E/p$  and  $p\lambda$ , where  $p$  is the pressure and  $\lambda$  is the free space wave length of the applied electric field. Integration of Equation (1) is simplified by the use of the approximation employed by Herlin and Brown (3, 4).

$$\zeta = \zeta_0 \left( \frac{E}{E_0} \right)^{\beta-2} = \left( \frac{k}{E_0} \right)^2 \left( \frac{E}{E_0} \right)^{\beta-2}, \quad (2)$$

where  $\zeta_0$  is the value of the ionization coefficient at the maximum field point;  $k$  is introduced for mathematical convenience and has the units of reciprocal length. The quantity  $\beta-2$  is obtained as the slope of the  $\zeta$  vs.  $E/p$  plot on a logarithmic scale. The slope required is that of  $\zeta$  for which  $p\lambda$  is kept constant. The approximation of Equation (2) is very good where the ionization is high. It is inaccurate only where there is little ionization and, since the regions in which there is little ionization contribute only slightly to the determination of breakdown fields, the procedure leads to correct results.

The electric field in the lowest electric mode in a spherical cavity may be given by (10, p. 562).

$$E_r = E_0 \left( \frac{a}{2.75r} \right) \cos \theta j_1(2.75r/a), \quad (3)$$

$$E_\theta = E_0 \left( \frac{a}{2.75r} \right) \sin \theta \frac{d}{dr} [(2.75r/a) j_1(2.75r/a)], \quad (4)$$

$$E_\phi = 0,$$

where  $r$ ,  $\theta$  and  $\phi$  are the spherical co-ordinates,  $a$  is the radius of the sphere, and  $j_1$  is the first-order spherical Bessel function.

It is seen that the electric field depends on both  $r$  and  $\theta$ , the introduction of which makes Equation (1) inseparable. However, in breakdown, we are interested only in the energy transfer from the field to the electrons so that we need take into account only the magnitude of the field at a given point. Near the center of the cavity, where the field, and therefore the ionization, is high, the magnitude of the electric field is approximately spherically symmetric. This fact is illustrated in Fig. 1, which shows the maximum variation of fields with  $\theta$ , as a function of  $r$ . If we assume that the electric field may be expressed as the average of these values over the whole of the cavity, we may write

$$E = E_0 [1 - (r/a)^2]. \quad (5)$$

Equation (5) is also plotted in Fig. 1, where it is seen to be a good approximation to the average electric field, except near the boundaries where it does not matter.

The assumption that the electric field is independent of  $\theta$  and  $\phi$  leads one to the independence of  $\psi$  on these variables. Therefore, we may write Equation (1) with the assumption of Equation (2).

$$\frac{1}{r^2} \frac{d}{dr} \left( r^2 \frac{d\psi}{dr} \right) + k^2 \left( \frac{E}{E_0} \right)^\beta \psi = 0,$$

and introducing the value of  $E$  from Equation (5), we have

$$\frac{1}{r^2} \frac{d}{dr} \left( r^2 \frac{d\psi}{dr} \right) + k^2 [1 - (r/a)^2]^\beta \psi = 0. \quad (6)$$

We expand the term in  $r/a$  by the binomial theorem and drop powers of  $(r/a)$  greater than 2. This makes an appreciable error only near the boundaries, where again the accuracy of the method is unimportant. Then

$$\frac{d^2\psi}{dr^2} + \frac{2}{r} \frac{d\psi}{dr} + k^2(1 - \mu^2 r^2)\psi = 0, \quad (7)$$

where  $\mu^2 = \beta/a^2$ .  $1/\mu$  is the radius at which the ionization goes to zero under the above assumptions. Beyond  $1/\mu$  these assumptions lead to a negative  $\zeta$  which is not physically correct, so we set  $\zeta = 0$  for  $r > 1/\mu$ .

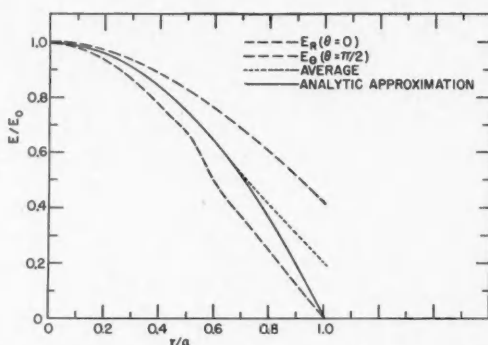


FIG. 1. Electric field in a spherical cavity showing the maximum variation and the analytic approximation to the average field as a function of radius.

For mathematical convenience, we transform to a dimensionless independent variable and let  $k\mu r^2 = x$ ; the equation (7) becomes

$$\frac{d^2\psi}{dx^2} + \frac{3}{2x} \frac{d\psi}{dx} + \frac{k^2}{x} \left( \frac{1}{4k\mu} - \frac{x}{4k^2} \right) \psi = 0 \quad x < \frac{k}{\mu}. \quad (8)$$

We transform the dependent variable by letting

$$\psi = e^{-x/2} g,$$

and then

$$\frac{d^2g}{dx^2} + \frac{dg}{dx} \left( \frac{3}{2x} - 1 \right) - \frac{ag}{x} = 0, \quad (9)$$

where

$$a = \frac{3}{4} - \frac{k}{4\mu}.$$

Equation (9) is the equation for the confluent hypergeometric function in parameters  $3/2$  and  $\alpha$  (Tables of this function are available (7, 8).) The second solution is not allowed by the boundary condition and therefore

$$\psi_1 = e^{-x/2} M\left(\alpha; \frac{3}{2}; x\right), \quad (10)$$

where we designate by  $\psi_1$  that part of  $\psi$  for which  $r$  is less than  $1/\mu$  or  $x < k/\mu$ . When  $x > k/\mu$ ,  $\zeta$  is zero and the differential equation (1) becomes

$$\frac{d}{dx} \left( x^{3/2} \frac{d\psi}{dx} \right) = 0,$$

of which the solution is

$$\psi_2 = C \left[ 1 - \left( \frac{x_0}{x} \right)^{1/2} \right], \quad (11)$$

where  $x_0 = k\mu a^2$  and is determined by the condition that  $\psi_2$  be zero on the boundary;  $C$  is an arbitrary constant. We must match the solutions of Equations (10) and (11) at the point where  $r = 1/\mu$  and therefore

$$\frac{\psi'_1}{\psi_1} = \frac{\psi'_2}{\psi_2},$$

which gives us

$$\frac{2/3 \alpha M(\alpha + 1; 5/2; x_1)}{M(\alpha; 3/2; x_1)} - \frac{1}{2} = \frac{1}{2x_1 \left[ \left( \frac{x_1}{x_0} \right)^{1/2} - 1 \right]}, \quad (12)$$

where

$$x_1 = k/\mu = \frac{ka}{\beta^{1/2}}.$$

Equation (12) relates  $a$ , the radius of the cavity,  $\beta$  determined from the slope of the  $\zeta$  curve and  $k$  which is inversely proportional to the characteristic diffusion length. The equation may be written in the form

$$\left[ \frac{2/3 \alpha M(\alpha + 1; 5/2; y)}{M(\alpha; 3/2; y)} - \frac{1}{2} \right] 2y = \frac{x}{1-x}, \quad (13)$$

where  $\alpha = \frac{3-y}{4}$ ,  $y = \frac{ka}{\beta^{1/2}}$  and  $x = \beta^{1/2}$ . Equation (13) is an equation in

which the left hand side is a function of  $ka/\beta^{1/2}$  only and the right hand side is a function of  $\beta^{1/2}$  only. Therefore it is a simple matter to find  $ka$  as a function of  $\beta$ . For the case of a uniform field, the characteristic diffusion length in a sphere is  $a/\pi$  and inspection of Equation (1) indicates that for a uniform field,  $k = \pi/a$ .  $k$  now may be considered as a measure of the effective radius of the discharge for diffusion and  $ka/\pi$  then is  $\Lambda/\Lambda_e$ , where  $\Lambda$  is the characteristic diffusion length as determined by the geometry of the container,  $\Lambda_e$  is the

effective characteristic diffusion length. Equation (13) is solved numerically and plotted in Fig. 2.

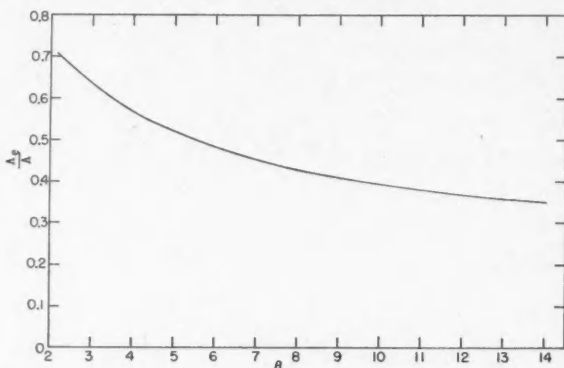


FIG. 2. Ratio of effective diffusion length to characteristic diffusion length.

## II. Experiment

Breakdown fields have been measured for hydrogen in a spherical cavity operating in the lowest electric mode. The details of experimental method are similar to those previously reported (5). The microwave apparatus is shown in Fig. 3. Microwave power with a free space wave length of approximately 10 cm. generated by a c-w magnetron is coupled to a microwave resonant cavity through coaxial transmission lines. A known fraction of the power delivered is measured by a bolometer. The power absorbed by the cavity is combined

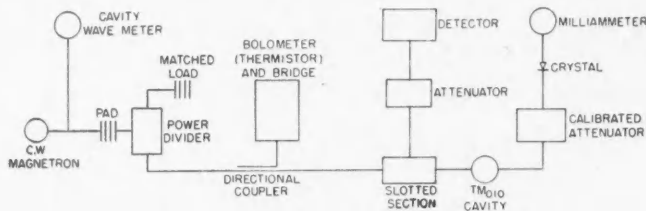


FIG. 3. Block diagram of experimental microwave apparatus.

with the cavity  $Q$  and the known field configuration to determine the electric field by standard methods (1, 9). The cavities in which breakdown takes place are made of oxygen-free high conductivity copper and connected through Kovar to an all-glass vacuum system. The vacuum system would hold at a pressure of better than  $10^{-7}$  mm. of mercury for a period of about two hours with the pumps turned off. A single series of breakdown measurements takes about this time.

### III. Calculation of Effective Diffusion Length

Fig. 4 is a  $\zeta$  vs.  $E/p$  plot for hydrogen. Constant  $p\lambda$  lines are plotted, the data being combined from breakdown measurements of cavities with different  $\Lambda$ 's. Those having the two smallest values of  $\Lambda$  are taken from previously reported data (6). This plot illustrates the use of the theory developed in this paper for computing an effective  $\Lambda$ . Both the corrected and uncorrected data are presented.

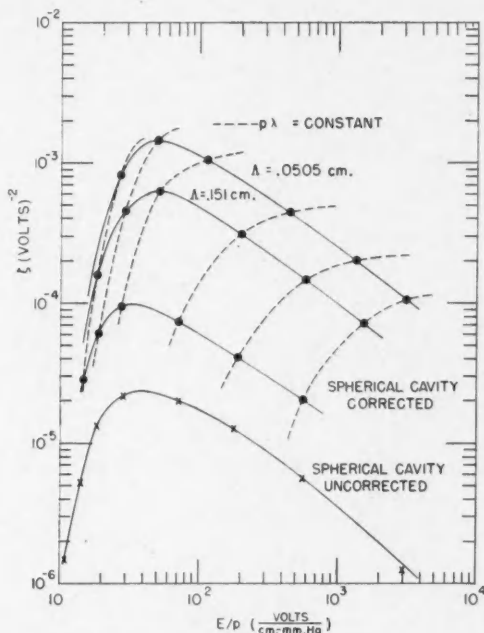


FIG. 4. Plot illustrating the actual calculation of effective  $\Lambda$ 's. Both the corrected and uncorrected  $\zeta$  curves for the spherical cavities are shown.

The procedure used in finding  $\Lambda_e$  begins with a plot of  $\zeta$  vs.  $E/p$ , using the geometrical value which is a first approximation. If the geometrical characteristic diffusion length is equal to the actual diffusion length, we shall find  $\Lambda_e/\Lambda$  from Fig. 2 to be equal to 1. This is not generally true, so we take the value of  $\beta$  for the slope of a constant  $p\lambda$  curve for the pressure and wave length in which we are interested, find  $\Lambda_e/\Lambda$  and recalculate  $\zeta$  to obtain a second approximation. This process is convergent and is continued until successive calculations agree.

The sphere used in the experiment had a radius of 4.69 cm. and a geometrical  $\Lambda$  of 1.49 cm. The effective  $\Lambda$  determined from the theory varies from 0.43 cm.

for a low  $E/p$  to 0.61 cm. for a high  $E/p$ . (The effective radius of the discharge depends on the ionization coefficient.)

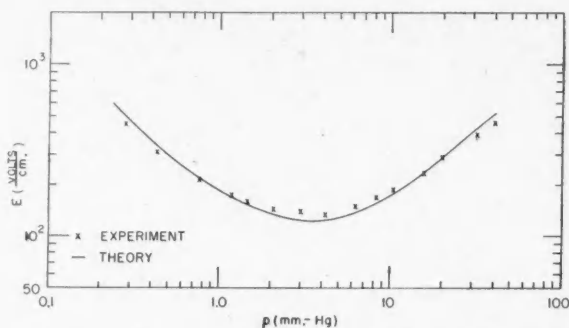


FIG. 5. Comparison of experimental electric field and values predicted from theory.

In Fig. 5 are plotted the theoretical values of  $E$  as a function of  $p$ , using the calculated values of  $\Lambda_e$ . These are calculated from the theory developed in two previous papers (5, 6), the value of  $\Lambda_e$  being inserted for  $\Lambda$  in this theory. Experimental verifications of these theories for the uniform field case was presented in the papers referred to. Experimental breakdown fields are compared with theory on the same figure. The good agreement illustrates the validity of the method.

### References

1. BROWN, S. C., BIONDI, M. A., HERLIN, M. A., EVERHART, E., and KERR, D. E. Methods of measuring the properties of ionized gases at microwave frequencies. Tech. Rept. No. 66. Research Laboratory of Electronics, Massachusetts Institute of Technology.
2. HERLIN, M. A. and BROWN, S. C. Phys. Rev. 74: 291. 1948.
3. HERLIN, M. A. and BROWN, S. C. Phys. Rev. 74: 1650. 1948.
4. HERLIN, M. A. and BROWN, S. C. Phys. Rev. 74: 910. 1948.
5. MACDONALD, A. D. and BROWN, S. C. Phys. Rev. 75: 411. 1949.
6. MACDONALD, A. D. and BROWN, S. C. Phys. Rev. 76: 1634. 1949.
7. MACDONALD, A. D. Properties of the confluent hypergeometric function. Tech. Rept. No. 84. Research Laboratory of Electronics, Massachusetts Institute of Technology.
8. MACDONALD, A. D. J. Math. Phys. 28: 183. 1949.
9. MONTGOMERY, C. G. Microwave techniques. McGraw-Hill Book Company, Inc., New York. 1948.
10. STRATTON, J. A. Electromagnetic theory. McGraw-Hill Book Company, Inc., New York, 1941.

# TABLES OF THE FUNCTION $e^{-az/\gamma} M(a; \gamma; z)^1$

By A. D. MACDONALD<sup>2</sup>

## Abstract

Six-figure tables of the function  $\mu(z) = e^{-az/\gamma} M(a; \gamma; z)$  have been computed for the following values of the parameters,  $a = 0.001, 0.01, 0.1$  (0.1) 1.0, 0.25, 0.75;  $\gamma = 0.5$  (0.5) 2.0, and  $z = 0$  (0.1) 1.0 (0.5) 8. They may be used in conjunction with tables of the exponential function for accurate values of the confluent hypergeometric function.

Tables of the confluent hypergeometric function multiplied by an exponential have been computed. The product  $e^{-az/\gamma} M(a; \gamma; z)$  which is herein designated  $\mu(z)$  has appeared in analytical solutions of the Boltzmann transport equation for electron distribution functions and is useful in predicting electrical breakdown in gases (2). There are two principal reasons for computing this particular function. In some cases, the breakdown equation may be written (2) simply by setting  $\mu(z) = 2$ .<sup>†</sup> In addition, the confluent hypergeometric function has an exponential type behavior in many regions, so that interpolation in the tables is difficult. The function tabulated in the present work is slowly varying, and good accuracy is obtainable by simple interpolation, requiring only first and second differences. Because extensive tables of the exponential function are readily available, tables of  $\mu(z)$  may be used in place of tables of the confluent hypergeometric function.

The tables of  $\mu(z)$  are more extensive than those of the confluent hypergeometric function previously published along with some of the more important properties of the function (1).

The tables have been computed by the Joint Computing Group of the Massachusetts Institute of Technology.

## References

1. MACDONALD, A. D. J. Math. Phys. 28: 183. 1949.<sup>‡</sup>
2. MACDONALD, A. D. and BROWN, S. C. Phys. Rev. 75: 411. 1949.

<sup>1</sup> Manuscript received November 18, 1949.

Contribution from the Research Laboratory of Electronics, Massachusetts Institute of Technology. Supported in part by the Signal Corps, O.N.R., and Air Material Command.

<sup>2</sup> Present address: Dalhousie University, Halifax, N.S.

\*The notation 0.1 (0.1) 1.0 indicates that  $a$  ranges from 0.1 to 1.0 at intervals at 0.1.

<sup>†</sup>As yet unpublished theories of breakdown in gases in addition to that reported in Ref. 2 lead to this condition.

<sup>‡</sup>Includes a number of references to published tables of the confluent hypergeometric function.

TABLE I

$$e^{-az/0.5} M(a; 0.5; z)$$

$\frac{a}{z}$	0.001	0.01	0.05	0.10	0.20	0.25	0.30
0.1	1.00001	1.00007	1.00031	1.00054	1.00080	1.00083	1.00080
0.2	1.00003	1.00028	1.00125	1.00220	1.00324	1.00334	1.00317
0.3	1.00006	1.00064	1.00288	1.00504	1.00733	1.00751	1.00710
0.4	1.00012	1.00116	1.00524	1.00913	1.01311	1.01337	1.01257
0.5	1.00019	1.00187	1.00839	1.01451	1.02063	1.02093	1.01956
0.6	1.00028	1.00276	1.01237	1.02128	1.02993	1.03019	1.02807
0.7	1.00040	1.00387	1.01724	1.02951	1.04106	1.04119	1.03809
0.8	1.00053	1.00521	1.02308	1.03929	1.05406	1.05395	1.04962
0.9	1.00070	1.00678	1.02995	1.05070	1.06900	1.06848	1.06266
1.0	1.00089	1.00863	1.03793	1.06385	1.08594	1.08483	1.07720
1.5	1.00235	1.02273	1.09762	1.15969	1.20322	1.19516	1.17285
2.0	1.00498	1.04792	1.20093	1.31913	1.38328	1.35788	1.30833
2.5	1.00941	1.09004	1.36819	1.56702	1.64142	1.58179	1.48726
3.0	1.01663	1.15814	1.63001	1.93955	1.99867	1.87907	1.71513
3.5	1.02819	1.26640	2.03268	2.48924	2.48357	2.26596	1.99940
4.0	1.04654	1.43698	2.64635	3.29250	3.13459	2.76367	2.34976
4.5	1.07556	1.70474	3.57747	4.46043	4.00323	3.39966	2.77842
5.0	1.12142	2.12453	4.98793	6.15478	5.15835	4.20915	3.30056
5.5	1.19391	2.78295	7.12434	8.61128	6.69183	5.23723	3.93487
6.0	1.30864	3.81690	10.3629	12.1738	8.72622	6.54143	4.70421
6.5	1.49057	5.44328	15.2785	17.3444	11.4249	8.19507	5.63650
7.0	1.77959	8.00619	22.7505	24.8567	15.0057	10.2916	6.76574
7.5	2.23963	12.0524	34.1258	35.7842	19.7592	12.9499	8.13326
8.0	2.97325	18.4519	51.4698	51.6979	26.0728	16.3214	9.78933

TABLE II

$$e^{-az/1.0} M(a; 1.0; z)$$

$\frac{a}{z}$	0.001	0.01	0.05	0.10	0.20	0.25	0.30
0.1	1.00000	1.00003	1.00012	1.00023	1.00041	1.00047	1.00053
0.2	1.00001	1.00010	1.00049	1.00093	1.00164	1.00192	1.00214
0.3	1.00002	1.00024	1.00114	1.00214	1.00375	1.00437	1.00486
0.4	1.00004	1.00043	1.00206	1.00388	1.00677	1.00786	1.00873
0.5	1.00007	1.00069	1.00330	1.00617	1.01073	1.01244	1.01378
0.6	1.00010	1.00102	1.00485	1.00907	1.01569	1.01814	1.02005
0.7	1.00014	1.00142	1.00675	1.01259	1.02169	1.02503	1.02759
0.8	1.00019	1.00191	1.00902	1.01678	1.02879	1.03314	1.03645
0.9	1.00025	1.00247	1.01168	1.02169	1.03703	1.04253	1.04668
1.0	1.00032	1.00313	1.01476	1.02735	1.04648	1.05326	1.05832
1.5	1.00082	1.00805	1.03758	1.06881	1.11426	1.12941	1.14009
2.0	1.00168	1.01652	1.07638	1.13819	1.22405	1.25077	1.26826
2.5	1.00307	1.03014	1.13799	1.24660	1.39005	1.43121	1.45566
3.0	1.00525	1.05132	1.23253	1.41022	1.63236	1.69016	1.72002
3.5	1.00857	1.08366	1.37505	1.65277	1.97949	2.05476	2.08578
4.0	1.01363	1.13265	1.58800	2.00906	2.47191	2.56287	2.58644
4.5	1.02128	1.20663	1.90513	2.53040	3.16713	3.26733	3.26796
5.0	1.03288	1.31835	2.37725	3.29268	4.14707	4.24196	4.19330
5.5	1.05049	1.48737	3.08119	4.40844	5.52852	5.59000	5.44880
6.0	1.07729	1.74387	4.13351	6.04506	7.47838	7.45600	7.15292
6.5	1.11825	2.13446	5.71152	8.45209	10.2356	10.04266	9.46838
7.0	1.18108	2.73145	8.08571	12.0025	14.1426	13.6346	12.6189
7.5	1.27781	3.64726	11.6698	17.2550	19.6914	18.6319	16.9123
8.0	1.42726	5.05713	17.0979	25.0479	27.5895	25.5979	22.7727



TABLE I  
 $e^{-az/0.5}M(a; 0.5; z)$ 

$\alpha \backslash z$	0.40	0.50	0.60	0.70	0.75	0.80	0.90	1.00
0.1	1.00052	1.00000	0.999229	0.998220	0.997629	0.996981	0.995520	0.993843
0.2	1.00207	1.00000	0.997027	0.993209	0.991000	0.988601	0.983257	0.977229
0.3	1.00458	1.00000	0.993549	0.985415	0.980771	0.975771	0.964778	0.952584
0.4	1.00803	1.00000	0.988932	0.975235	0.967518	0.959280	0.941403	0.921907
0.5	1.01237	1.00000	0.983304	0.963023	0.951746	0.939812	0.914250	0.886843
0.6	1.01756	1.00000	0.976778	0.949088	0.933895	0.917956	0.884256	0.848735
0.7	1.02358	1.00000	0.969457	0.933708	0.914350	0.894220	0.852210	0.808679
0.8	1.03039	1.00000	0.961433	0.917124	0.893447	0.869042	0.818768	0.767560
0.9	1.03797	1.00000	0.952792	0.899552	0.871480	0.842796	0.784477	0.726085
1.0	1.04629	1.00000	0.943608	0.881180	0.848700	0.815804	0.749788	0.684818
1.5	1.09829	1.00000	0.891748	0.782522	0.729392	0.677910	0.581141	0.493828
2.0	1.16620	1.00000	0.834274	0.681857	0.612605	0.548430	0.435464	0.342116
2.5	1.24877	1.00000	0.775131	0.586641	0.506715	0.435903	0.319193	0.230950
3.0	1.34547	1.00000	0.716677	0.500253	0.414683	0.342229	0.230420	0.153138
3.5	1.45626	1.00000	0.660286	0.423844	0.336753	0.266298	0.164503	0.100229
4.0	1.58152	1.00000	0.606726	0.357378	0.271889	0.205832	0.116468	0.064959
4.5	1.72196	1.00000	0.556387	0.300221	0.218543	0.158277	0.081928	0.041780
5.0	1.87856	1.00000	0.509421	0.251472	0.175048	0.121212	0.057336	0.026708
5.5	2.05255	1.00000	0.465834	0.210147	0.139813	0.092522	0.039959	0.016989
6.0	2.24538	1.00000	0.425542	0.175278	0.111412	0.070432	0.027753	0.010762
6.5	2.45876	1.00000	0.388408	0.145963	0.088608	0.053494	0.019219	0.006794
7.0	2.69461	1.00000	0.354264	0.121388	0.070357	0.040552	0.013277	0.004276
7.5	2.95507	1.00000	0.322929	0.100835	0.055787	0.030690	0.009153	0.002685
8.0	3.24258	1.00000	0.294213	0.083680	0.044181	0.023194	0.006298	0.001682

TABLE II  
 $e^{-az/1.0}M(a; 1.0; z)$ 

$\alpha \backslash z$	0.40	0.50	0.60	0.70	0.75	0.80	0.90	1.00
0.1	1.00060	1.00063	1.00060	1.00052	1.00046	1.00039	1.00022	1.00000
0.2	1.00242	1.00250	1.00238	1.00206	1.00183	1.00156	1.00087	1.00000
0.3	1.00548	1.00563	1.00534	1.00461	1.00409	1.00346	1.00192	1.00000
0.4	1.00980	1.01003	1.00945	1.00813	1.00719	1.00608	1.00336	1.00000
0.5	1.01540	1.01569	1.01473	1.01260	1.01113	1.00939	1.00517	1.00000
0.6	1.02231	1.02263	1.02115	1.01802	1.01588	1.01337	1.00732	1.00000
0.7	1.03057	1.03086	1.02872	1.02436	1.02141	1.01799	1.00981	1.00000
0.8	1.04020	1.04040	1.03743	1.03160	1.02772	1.02324	1.01262	1.00000
0.9	1.05124	1.05127	1.04728	1.03975	1.03479	1.02910	1.01573	1.00000
1.0	1.06373	1.06348	1.05828	1.04878	1.04259	1.03555	1.01913	1.00000
1.5	1.14960	1.14564	1.13071	1.10695	1.09235	1.07623	1.04012	1.00000
2.0	1.27978	1.26606	1.23330	1.18656	1.15927	1.12998	1.06690	1.00000
2.5	1.46374	1.43047	1.36855	1.28786	1.24293	1.19599	1.09862	1.00000
3.0	1.71441	1.64672	1.54021	1.41187	1.34347	1.27387	1.13469	1.00000
3.5	2.04912	1.92526	1.75335	1.56023	1.46154	1.36363	1.17472	1.00000
4.0	2.49095	2.27959	2.01453	1.73527	1.59820	1.46555	1.21843	1.00000
4.5	3.07042	2.72708	2.33199	1.93994	1.75490	1.58014	1.26568	1.00000
5.0	3.82782	3.28984	2.71592	2.17788	1.93348	1.70814	1.31637	1.00000
5.5	4.81629	3.99685	3.17882	2.45343	2.13615	1.85048	1.37049	1.00000
6.0	6.10581	4.88079	3.73588	2.77175	2.36550	2.00827	1.42804	1.00000
6.5	7.78856	5.98934	4.40558	3.13888	2.62455	2.18280	1.48907	1.00000
7.0	9.98605	7.37822	5.21031	3.56184	2.91676	2.37554	1.55365	1.00000
7.5	12.8585	9.11894	6.17712	4.04881	3.24607	2.58815	1.62190	1.00000
8.0	16.6172	11.3019	7.33875	4.60927	3.61698	2.82248	1.69392	1.00000

TABLE III  
 $e^{-az/1.5}M(a; 1.5; z)$

$\frac{a}{z}$	0.001	0.01	0.05	0.10	0.20	0.25	0.30
0.1	1.00000	1.00001	1.00007	1.00013	1.00023	1.00028	1.00032
0.2	1.00001	1.00006	1.00027	1.00051	1.00095	1.00114	1.00131
0.3	1.00001	1.00013	1.00061	1.00118	1.00217	1.00260	1.00298
0.4	1.00002	1.00023	1.00111	1.00213	1.00392	1.00469	1.00537
0.5	1.00004	1.00037	1.00177	1.00339	1.00622	1.00743	1.00850
0.6	1.00005	1.00054	1.00259	1.00497	1.00909	1.01085	1.01240
0.7	1.00008	1.00075	1.00360	1.00689	1.01258	1.01498	1.01710
0.8	1.00010	1.00099	1.00480	1.00917	1.01669	1.01986	1.02265
0.9	1.00013	1.00129	1.00620	1.01183	1.02148	1.02552	1.02906
1.0	1.00016	1.00162	1.00781	1.01489	1.02696	1.03200	1.03639
1.5	1.00041	1.00409	1.01958	1.03709	1.06630	1.07817	1.08834
2.0	1.00083	1.00821	1.03912	1.07364	1.12991	1.15217	1.17084
2.5	1.00148	1.01463	1.06937	1.12971	1.22578	1.26269	1.29292
3.0	1.00246	1.02428	1.11454	1.21269	1.36513	1.42186	1.46711
3.5	1.00391	1.03853	1.18070	1.33319	1.56382	1.64669	1.71083
4.0	1.00603	1.05935	1.27674	1.50651	1.84429	1.96103	2.04826
4.5	1.00912	1.08969	1.41563	1.75482	2.23847	2.39845	2.51310
5.0	1.01364	1.13389	1.61648	2.11047	2.79188	3.00631	3.15239
5.5	1.02024	1.19846	1.90756	2.62076	3.56970	3.85166	4.03193
6.0	1.02995	1.29313	2.33090	3.35520	4.66549	5.02961	5.24399
6.5	1.04427	1.43257	2.94918	4.41633	6.21403	6.67552	6.91825
7.0	1.06552	1.63899	3.85635	5.95593	8.40997	8.88248	9.23742
7.5	1.09718	1.94606	5.19364	8.19940	11.5352	12.2266	12.4594
8.0	1.14463	2.40514	7.17412	11.4825	15.9992	16.8035	16.9491

TABLE IV  
 $e^{-az/2.0}M(a; 2.0; z)$

$\frac{a}{z}$	0.001	0.01	0.05	0.10	0.20	0.25	0.30
0.1	1.00000	1.00001	1.00004	1.00008	1.00015	1.00018	1.00022
0.2	1.00000	1.00003	1.00017	1.00033	1.00062	1.00075	1.00087
0.3	1.00001	1.00008	1.00038	1.00075	1.00141	1.00171	1.00198
0.4	1.00001	1.00014	1.00069	1.00135	1.00254	1.00307	1.00357
0.5	1.00002	1.00023	1.00110	1.00214	1.00402	1.00487	1.00565
0.6	1.00003	1.00033	1.00162	1.00313	1.00588	1.00710	1.00824
0.7	1.00005	1.00046	1.00224	1.00433	1.00812	1.00981	1.01137
0.8	1.00006	1.00061	1.00297	1.00576	1.01076	1.01299	1.01505
0.9	1.00008	1.00079	1.00383	1.00741	1.01384	1.01669	1.01931
1.0	1.00010	1.00099	1.00482	1.00931	1.01735	1.02091	1.02418
1.5	1.00025	1.00246	1.01192	1.02294	1.04241	1.05091	1.05861
2.0	1.00049	1.00485	1.02347	1.04500	1.08251	1.09863	1.11309
2.5	1.00086	1.00850	1.04095	1.07820	1.14220	1.16929	1.19329
3.0	1.00139	1.01382	1.06643	1.12632	1.22780	1.27003	1.30699
3.5	1.00217	1.02146	1.10280	1.19467	1.34806	1.41077	1.46492
4.0	1.00326	1.03230	1.15419	1.29072	1.51520	1.60525	1.68187
4.5	1.00481	1.04762	1.22647	1.42510	1.74637	1.87266	1.97836
5.0	1.00701	1.06923	1.32810	1.61296	2.06576	2.23983	2.38292
5.5	1.01011	1.09983	1.47125	1.87605	2.50758	2.74452	2.93534
6.0	1.01453	1.14329	1.67366	2.24575	3.12050	3.43996	3.69137
6.5	1.02084	1.20535	1.96120	2.76755	3.97396	4.40159	4.72933
7.0	1.02991	1.29444	2.37183	3.50767	5.16750	5.73660	6.15961
7.5	1.04303	1.42309	2.96149	4.56291	6.84423	7.59785	8.13823
8.0	1.06210	1.60997	3.81301	6.07539	9.21068	10.2040	10.8867

TABLE III  
 $e^{-\alpha z/1.5} M(\alpha; 1.5; z)$ 

$\alpha \backslash z$	0.40	0.50	0.60	0.70	0.75	0.80	0.90	1.00
0.1	1.00039	1.00045	1.00048	1.00050	1.00050	1.00050	1.00048	1.00044
0.2	1.00159	1.00180	1.00194	1.00200	1.00200	1.00199	1.00191	1.00176
0.3	1.00362	1.00408	1.00438	1.00450	1.00451	1.00447	1.00428	1.00393
0.4	1.00650	1.00731	1.00782	1.00802	1.00802	1.00794	1.00758	1.00695
0.5	1.01026	1.01151	1.01227	1.01257	1.01254	1.01241	1.01181	1.01080
0.6	1.01493	1.01671	1.01777	1.01815	1.01809	1.01787	1.01697	1.01548
0.7	1.02054	1.02293	1.02432	1.02478	1.02467	1.02434	1.02306	1.02097
0.8	1.02712	1.03020	1.03196	1.03247	1.03229	1.03182	1.03006	1.02727
0.9	1.03472	1.03856	1.04070	1.04125	1.04096	1.04031	1.03799	1.03438
1.0	1.04336	1.04803	1.05057	1.05112	1.05070	1.04983	1.04684	1.04228
1.5	1.10390	1.11361	1.11806	1.11780	1.11707	1.11334	1.10516	1.09368
2.0	1.19829	1.21395	1.21939	1.21600	1.21140	1.20506	1.18773	1.16503
2.5	1.33537	1.35694	1.36100	1.35056	1.34074	1.32826	1.29640	1.25700
3.0	1.52730	1.55326	1.55162	1.52806	1.50960	1.48744	1.43391	1.37095
3.5	1.79064	1.81734	1.80284	1.75715	1.72527	1.68859	1.60397	1.50881
4.0	2.14804	2.16843	2.12990	2.04909	1.99713	1.93938	1.81133	1.67316
4.5	2.63035	2.63233	2.55278	2.41831	2.33712	2.24950	2.06197	1.86727
5.0	3.27970	3.24341	3.09755	2.88327	2.76037	2.63112	2.36323	2.09510
5.5	4.15369	4.04758	3.79821	3.46747	3.28592	3.09937	2.72409	2.36143
6.0	5.33113	5.10621	4.69907	4.20080	3.93769	3.67302	3.15543	2.67194
6.5	6.92009	6.50126	5.85784	5.12122	4.74564	4.37534	3.67041	3.03438
7.0	9.06900	8.34246	7.34980	6.27693	5.74739	5.23510	4.28486	3.45559
7.5	11.9820	10.7769	9.27316	7.72917	6.99005	6.28789	5.01789	3.94188
8.0	15.9404	14.0016	11.7562	9.55576	8.53265	7.57769	5.89246	4.50911

TABLE IV  
 $e^{-\alpha z/2.0} M(\alpha; 2.0; z)$ 

$\alpha \backslash z$	0.40	0.50	0.60	0.70	0.75	0.80	0.90	1.00
0.1	1.00027	1.00032	1.00035	1.00038	1.00039	1.00040	1.00041	1.00042
0.2	1.00109	1.00127	1.00142	1.00153	1.00158	1.00161	1.00166	1.00167
0.3	1.00248	1.00289	1.00322	1.00347	1.00356	1.00364	1.00374	1.00375
0.4	1.00445	1.00518	1.00576	1.00620	1.00637	1.00650	1.00666	1.00668
0.5	1.00703	1.00817	1.00907	1.00975	1.01000	1.01020	1.01043	1.01045
0.6	1.01024	1.01188	1.01317	1.01413	1.01448	1.01476	1.01507	1.01507
0.7	1.01410	1.01633	1.01808	1.01936	1.01983	1.02019	1.02058	1.02054
0.8	1.01864	1.02155	1.02382	1.02546	1.02606	1.02650	1.02697	1.02688
0.9	1.02387	1.02756	1.03041	1.03246	1.03319	1.03373	1.03426	1.03409
1.0	1.02984	1.03440	1.03789	1.04037	1.04124	1.04188	1.04247	1.04219
1.5	1.07175	1.08201	1.08958	1.09464	1.09629	1.09736	1.09790	1.09642
2.0	1.13728	1.15560	1.16852	1.17652	1.17881	1.18003	1.17946	1.17520
2.5	1.23265	1.26142	1.28066	1.29140	1.29386	1.29455	1.29099	1.28154
3.0	1.36628	1.40793	1.43402	1.44651	1.44822	1.44719	1.43769	1.41952
3.5	1.54970	1.60656	1.63932	1.65148	1.65084	1.64621	1.62637	1.59452
4.0	1.79863	1.87276	1.91088	1.91897	1.91345	1.90238	1.86581	1.81343
4.5	2.13457	2.22734	2.26775	2.26564	2.25139	2.22966	2.16729	2.08497
5.0	2.58702	2.69847	2.73531	2.71334	2.68462	2.64612	2.54516	2.42008
5.5	3.19652	3.32504	3.34742	3.29075	3.23913	3.17508	3.01764	2.83249
6.0	4.01897	4.15642	4.14921	4.03549	3.94873	3.84661	3.60788	3.33929
6.5	5.13163	5.26526	5.20102	4.99696	4.85743	4.69955	4.34521	3.96179
7.0	6.64158	6.74651	6.58362	6.24014	6.02259	5.78402	5.26680	4.72646
7.5	8.69761	8.73093	8.40528	7.85055	7.51901	7.16480	6.41983	5.66634
8.0	11.5070	11.3973	10.8114	9.94091	9.44437	8.92566	7.86413	6.82248

## THE MICROWAVE ABSORPTION SPECTRUM OF METHYL ALCOHOL<sup>1</sup>

BY BARBARA M. GIRDWOOD<sup>2</sup>

### Abstract

The microwave absorption spectrum of methyl alcohol was studied in the region 23,400 to 25,200 Mc., using a double modulation system in which the usual radio-frequency sine wave was replaced by a sharp, pip-shaped pulse with a repetition rate of 55 kc. Twenty-five new lines were found and these, along with those previously reported outside the region examined, were grouped into four series. When the methyl alcohol was mixed with a large percentage of water vapor the spectrum was found to be modified considerably.

### Introduction

Lines in the microwave absorption spectrum of methyl alcohol have been reported previously by Hershberger and Turkevitch (5), B. P. Dailey (2), and by B. Bak, E. S. Knudsen, and E. Madsen (1), using either the Hughes and Wilson (6) Stark modulation or the Gordy and Kessler (4) double modulation techniques. The author used a double modulation method but replaced the r.f. sine wave with a sharp pip with a repetition rate of 55 kc. With this arrangement methyl alcohol and methyl alcohol in water vapor were studied in the 1.25 cm. region and a number of new lines were discovered. It was found that the presence of water vapor in large percentages had a marked effect on the position of the lines.

### Apparatus

The spectroscope which was used is shown schematically in Fig. 1 and the pip modulator in Fig. 2. The receiver was a RCN type SCR-5A and was tuned to 110 kc. Frequencies were measured by a cavity wavemeter which had been calibrated previously from the known ammonia lines.

As shown in Fig. 3, the irregularity of the signal from the detecting crystal for a sine wave and a very narrow absorption line would make it impossible to amplify, but the output from the pip modulator and a narrow line, as shown in Fig. 4, is regularly spaced and easily amplified. The signal from a line whose width is greater than the amplitude of the modulating wave is shown in Fig. 5. It is very likely that the pip modulation adds a false width to the line and thus distorts the line shape.

Part of the gain in sensitivity which was obtained was due to a reduction in noise background. The sawtooth oscillator and pip generator were built to operate without a trigger signal and there was very little 55 kc. signal which could be picked up by the tuned receiver because the Fourier frequencies involved in the pip were much higher. Undoubtedly a further gain could be achieved by building a receiver which could be tuned to the original modulation repetition rate.

<sup>1</sup> Manuscript received November 8, 1949.

Contribution from the Department of Physics, McGill University, Montreal, Que.

<sup>2</sup> Present address; National Research Laboratories, Ottawa, Canada.

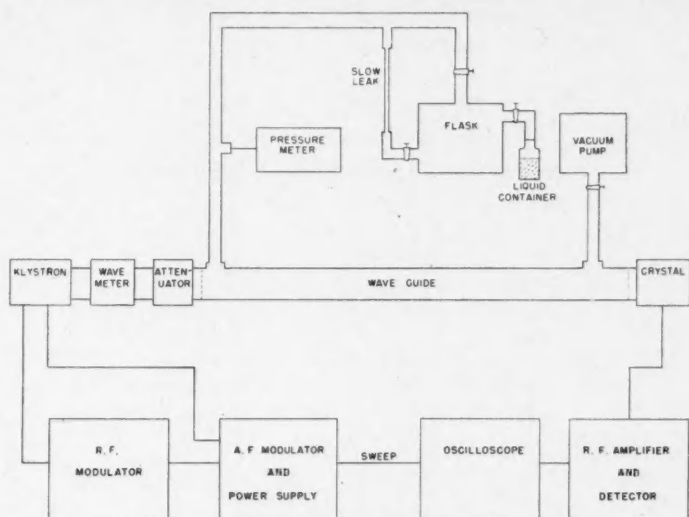


FIG. 1. Schematic diagram of microwave spectroscope.

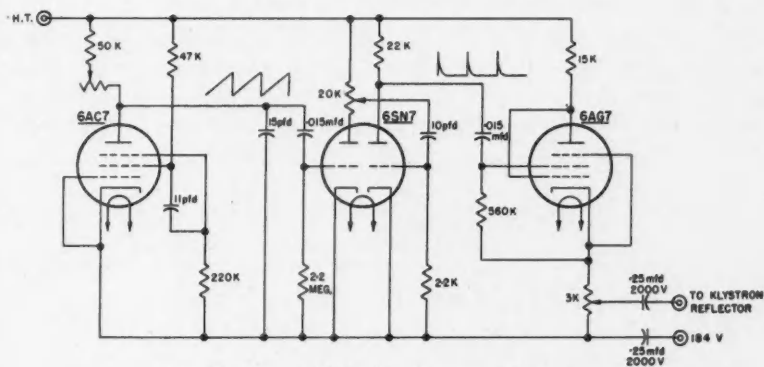


FIG. 2. Pip modulator for microwave spectroscope.

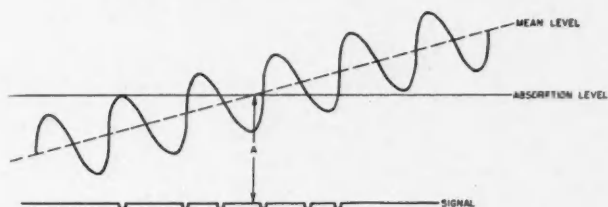


FIG. 3. Klystron frequency vs. time for narrow line and sine wave modulator.

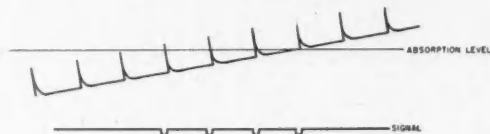


FIG. 4. Klystron frequency vs. time for wide line and pip modulator.

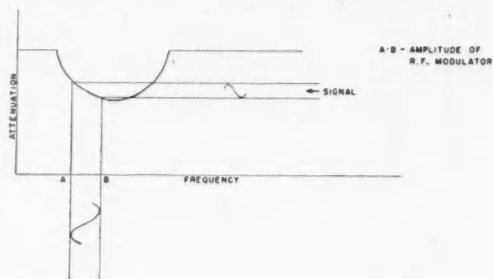


FIG. 5. Signal from wide line using sine wave modulator.

### The Absorption Spectrum of Methyl Alcohol

The lines which have been reported are in a range 20,898 to 26,562 Mc. while the present work was done in the range 23,400 to 25,200 Mc. The frequencies of the new lines which were found, along with the ones which were verified, are shown in Table I. All the lines appeared as doublets. An accuracy of  $\pm 5$  Mc. was obtained.

TABLE I

#### ABSORPTION SPECTRUM OF METHYL ALCOHOL

w—weak, b—broad, bb—very broad, s—sharp, ss—very sharp

Frequency, Mc.	Reported at	Comments	Frequency, Mc.	Reported at	Comments
25,182		b	24,280		s
25,135	25,132.0	b	24,235		ss
25,056	25,050	b	24,180		ss
25,015	25,017	bb	24,132		ss
24,966	24,954	bb	24,068-76	24,080	quadruplet 2 Mc separation
24,928	24,928.8	bb, width— 24,928-913	24,017		ss
24,863		bb	23,955		ss
24,806		b	23,908		ss
24,752		b	23,858	23,861	ss
24,697		b, w	23,812		s, w
24,640		b, w	23,759		s, w
24,588		b, w	23,702		s, w
24,530		b, w	23,650		s, w
24,478		b, w	23,594		s
24,426		bb	23,538		s
24,372		bb	23,493		s
24,317	24,317	bb	23,445	23,450	Triplet

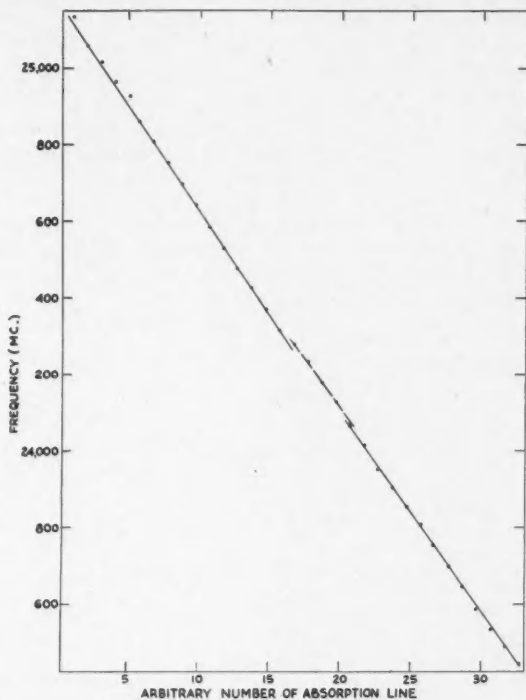


FIG. 6. Methyl alcohol spectrum in the region 23,400 to 25,200 Mc.

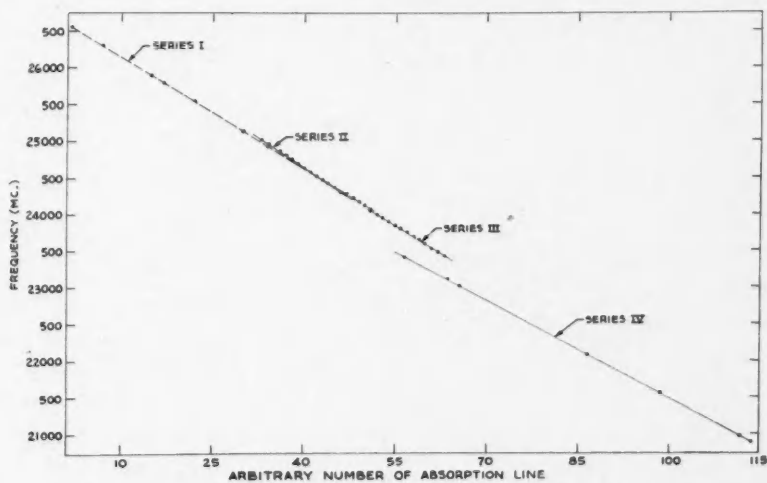


FIG. 7. Methyl alcohol spectrum in the region 21,000 to 27,000 Mc.

The very nearly equal spacings between the lines were at once apparent and, when the lines were empirically numbered 1, 2, 3,—in order of decreasing frequency and a plot made of frequency against line number (Fig. 6), the lines were seen to fall into three separate series. On the assumption that the lines which had been reported but which were outside the region examined were part of a similar arrangement, the values were studied and were finally plotted as shown in Fig. 7. In all there were four separate series.

The accuracy of this plot may be seen from Tables II, III, IV, and V, where the first and second differences have been tabulated. The lines were grouped in series as indicated by the graph, and the integer dividers for the intervals were also determined from the graph.

TABLE II  
SERIES I

Frequency, Mc.	First difference	Second difference
26,562		
26,310	$\frac{252}{5} = 50$	
25,898	$\frac{412}{8} = 51$	-1
25,796	$\frac{102}{2} = 51$	0
25,546	$\frac{250}{5} = 50$	+1
25,385	$\frac{161}{3} = 53$	-3
25,135	$\frac{250}{5} = 50$	+3
24,929	$\frac{206}{4} = 51$	-1
24,280	$\frac{649}{13} = 50$	+1
24,235	45	+5
24,180	55	-10
24,132	48	+7
24,076	56	-8
		-6

Bak, Knudsen, and Madsen (1) have measured lines in the region of 25,200 Mc. and these values, along with the others available, were plotted in Fig. 8 to show the detail in this part of the spectrum. The above groupings include



TABLE III

## SERIES II

Frequency, Mc.	First difference	Second difference
25,015		
25,966	59	
24,863	$\frac{103}{2} = 51$	+8
24,806	57	-6
24,752	54	+3
24,697	55	-1
24,640	57	-2
24,588	52	+5
24,530	58	-6
24,478	52	+6
24,426	52	0
24,372	54	-2
24,317	55	-1
		+4

TABLE IV

## SERIES III

Frequency, Mc.	First difference	Second difference
24,017		
23,955	62	
23,908	47	+15
23,858	50	-3
23,812	46	+4
23,759	53	-7
23,702	57	-4
23,650	52	+5
23,594	56	-4
23,538	56	0
23,493	45	+11
23,445	48	-3
		+11

TABLE V

SERIES IV

Frequency, Mc.	First difference	Second difference
23,415		
23,121	$\frac{294}{7} = 42$	
23,033	$\frac{88}{2} = 44$	-2
22,095	$\frac{938}{21} = 44$	0
21,551	$\frac{544}{12} = 45$	-1
20,989	$\frac{562}{13} = 43$	+2
20,898	$\frac{91}{2} = 45$	-2
		-3

NOTE: *The identification of these as a series is uncertain owing to the size of the intervals.*

all the published lines except one at 24,040 Mc. which was not found by the author and could not be fitted into the picture.

### Alcohol in Water Vapor

The frequencies obtained when the methyl alcohol was in a mixture containing roughly 70% water vapor are listed in Table VI and are plotted in Fig. 9. The shift of the lines from their former positions—the shift being greater the further the line was from the region of 24,312 Mc.—and the presence of two single lines in the same region were the most noteworthy features of the spectrum.

When the mixture of alcohol and water vapor was first admitted to the silver absorption cell the lines were displaced but they returned to their original position within an hour. The second time the mixture was admitted the lines were displaced and remained displaced for the three hours during which they were watched.

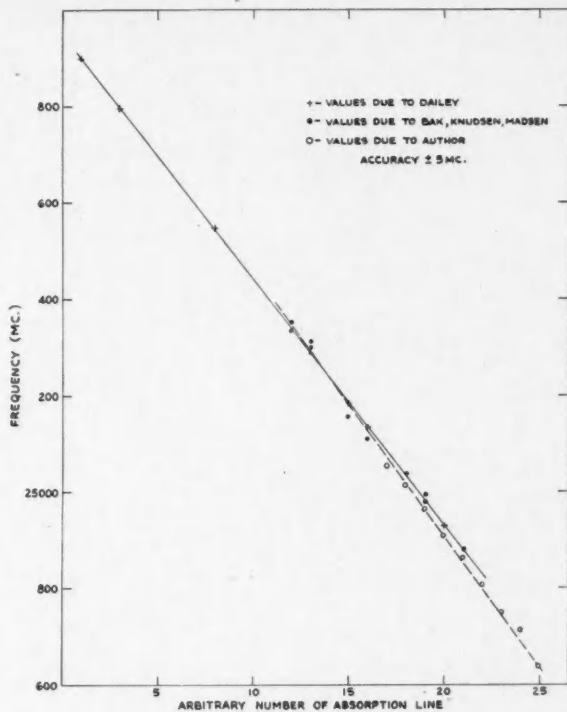


FIG. 8. Methyl alcohol spectrum in the region 24,600 to 25,900 Mc.

TABLE VI

ABSORPTION SPECTRUM OF METHYL ALCOHOL IN WATER VAPOR

w—weak, b—broad, bb—very broad, s—sharp, ss—very sharp

Frequency, Mc.	Comments	Frequency	Comments
24,884	bb, w	24,076	ww
24,776	bb	24,046	s
24,721	bb	23,991	s
24,666	bb	23,938	s
24,617	b	23,890	s
24,570	b	23,835	s
24,511	b	23,781	s
24,463	b	23,723	s
24,410	b	23,662	s
24,364	b	23,606	s
24,312	b, single	23,546	s
24,265	b, single	23,504	s
24,209	ss	23,457	bb
24,156	ss	23,440	ss
24,100	ss		

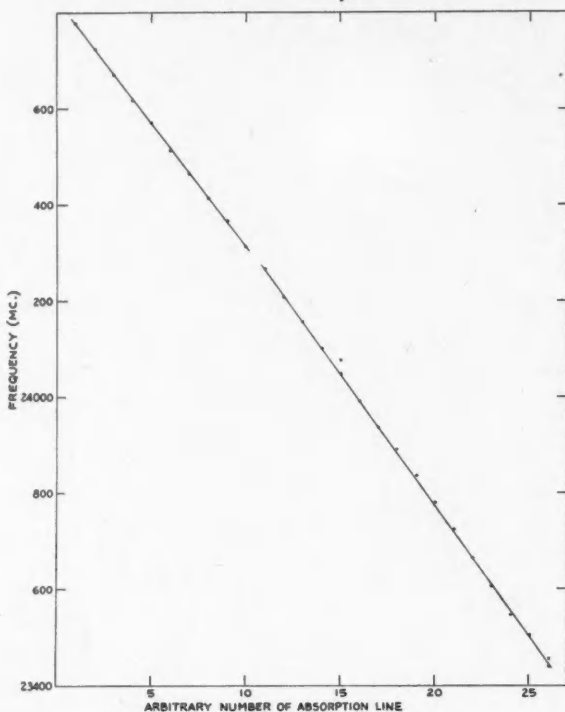


FIG. 9. Absorption spectrum of methyl alcohol in water vapor.

### The Interpretation of the Spectra

The methyl alcohol spectrum has been attributed by Dennison\* to the hindered internal rotation of the OH radical and he has calculated the frequencies of eight of the lines on this basis. However this gives a value of the barrier height lower than that estimated from the infrared spectrum and does not explain the observed Stark effect. There is now the added difficulty of explaining the effect of the water vapor. The addition of a H atom or a complete water molecule would be expected to have a more serious effect on the spectrum. Another explanation might be that the spectrum is due to the rotation of two molecules joined together by the OH radical. Such a double molecule would have a rotation line at approximately 26,000 Mc. and, owing to vibrations of the low energy bond joining the two molecules, would have a number of equally spaced lines on either side of the pure rotation line. The number of observed lines seems to be rather large unless the energies of the

\*Unpublished results referred to by Gordy (3).

vibrations involved are extremely small. Further information is required before the methyl alcohol spectrum can be completely understood.

### Acknowledgments

The author wishes to acknowledge the help and encouragement of Dr. J. S. Foster and the staff of the Radiation Laboratory of McGill University during the course of this work.

### References

1. BAK, B., KNUDSEN, E. S., and MADSEN, E. Phys. Rev. 75: 1662. 1949.
2. DAILEY, B. P. Phys. Rev. 72: 84. 1947.
3. GORDY, W. Revs. Modern Phys. 20: 668. 1948.
4. GORDY, W. and KESSLER, M. Phys. Rev. 72: 64. 1947.
5. HERSHBERGER, W. D. and TURKEVITCH, J. Phys. Rev. 71: 554. 1947.
6. HUGHES, R. E. and WILSON, E. B. Phys. Rev. 71: 562. 1947.

## ENERGY DISTRIBUTION OF FISSION FRAGMENTS FROM $U^{235}$ AND $U^{233}$ <sup>1</sup>

By D. C. BRUNTON AND G. C. HANNA

### Abstract

New measurements have been made of the energy distribution of fission fragments. A coincident pulse technique has been used which measures simultaneously the energies of both fragments of a fission pair. Previous work in this field was limited in statistical accuracy owing to low fission rates. With the Chalk River high flux pile and a 30-channel pulse analyzer a rapid accumulation of data is made possible. The improved statistical accuracy has led to new results on the detailed association of fragment pairs and on the energy variation occurring in each fission mode. A careful comparison of  $U^{233}$  and  $U^{235}$  has been made.

### I. Introduction

The first measurements of the ionization pulses from fission fragments were made by Frisch (13), who recorded fragment energies of the order of 100 Mev. in an ionization chamber in 1939. Shortly afterwards Jentschke and Prankl (16) resolved the fragment energy spectrum into two groups at about 60 and 100 Mev. Booth, Dunning, and Slack (2) found a continuous distribution of fragment energies with two pronounced maxima. Subsequently many measurements have been made of the energy spectrum from fission fragments (8, 10, 11, 12, 17, 18, 19, 22).

The experiments of Jentschke (18), of Flammersfeld, Jensen, and Gentner (10) and of Deutsch and Ramsey (8) are of particular interest because, in these experiments, the energies of both fragments of a fission pair were measured simultaneously. The source was placed at the center of a double "back-to-back" ionization chamber. When fission occurred the two fragments traveled in opposite directions into the two chambers. The ionization pulses were amplified and displayed on a double beam oscilloscope. A continuous photographic record was made, and the film was examined for coincident pulses. A rather tedious examination of the film is required, and the results of these experiments show poor statistical accuracy. One of the purposes of the present experiment was to decrease the statistical errors and obtain reasonably accurate data on the spread of kinetic energies associated with each splitting ratio of the uranium nucleus. This objective was feasible at the Chalk River Laboratory because of the exceptional facilities available, namely, a high flux pile and a 30-channel pulse analyzer.

The work of Deutsch and Ramsey (8) included a comparison of the energy distributions for fission in  $U^{235}$  and  $Pu^{239}$ . The present experiment has extended this comparison to fission in  $U^{233}$ .

<sup>1</sup> Manuscript received November 14, 1949.

Contribution from the Nuclear Physics Branch, Division of Atomic Energy Research, National Research Council of Canada, Chalk River, Ontario. Issued as N.R.C. No. 2085.

As in previous work, the present experiment employed a double ionization chamber with a thin source mounted on the common cathode. The general plan of the experiment was to select in one chamber fragments in a small energy interval, and to measure the energy distribution of the coincident fragments in the other chamber. A preliminary note on some of the results obtained has already been published in the Physical Review (4).

## II. Experimental Equipment

The double ionization chamber used is shown in Fig. 1. The chamber was constructed almost entirely of aluminum to reduce the background activity when irradiated with a high flux of neutrons. The insulation consisted of porcelain and of glass coated with ceresin wax. The electrode connections were introduced through Kovar seals, and the main vacuum seals were made with neoprene gaskets.

The chamber employed electron collection to obtain fast rising pulses. For this purpose Frisch grids were used to shield the collecting electrodes from charges induced by the slowly moving positive ions. The operation of grid chambers has been carefully investigated by Bunemann, Cranshaw, and Harvey (5). The grids used were constructed of copper wire, 0.013 cm. diameter, spaced 0.188 cm. apart, and separated from the collecting electrodes by 1 cm. This design gave a screening efficiency greater than 98%.

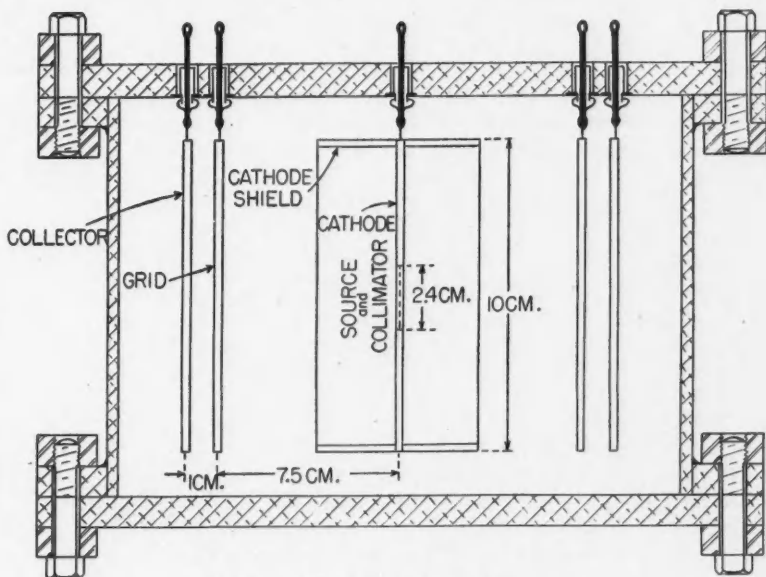


FIG. 1. The double ionization chamber.

The common cathode carried the collimator. The uranium source was contained in a collodion film mounted on this collimator. Preparation of the source is described in Section III. The collimator was a dural plate 0.010 in. thick, with approximately 2000 closely spaced holes, 0.010 in. in diameter. Thus the collimator allows only fragments within  $45^\circ$  from the normal to the cathode to enter one chamber. Collimation is required to limit ionization losses. Losses associated with fragments at large angles to the normal are twofold; firstly, self-absorption in the source becomes objectionable with long oblique paths; secondly, electrons may escape to the case if a portion of the track is allowed to enter the fringing field near the edges of the electrodes. The cathode shields shown in Fig. 1 were added to reduce further this electron loss.

The chamber was filled with pure argon plus about 3% carbon dioxide to a pressure of 65 cm. of mercury. The pressure was so chosen that the fragments of longest range traveled only about 60% of the distance from the cathode to the grid. Under these conditions the natural  $\alpha$ -particles from the sources were also contained well within the cathode-grid region. The carbon dioxide was added to the argon to increase the electron mobility and permit fast collection.

As the source was mounted on one side of the collimator only, fragments entering one of the chambers, "the collimated chamber", were collimated directly. Collimation in the other chamber was secured by counting only coincident pulses. Fragments in a small energy interval were selected in the uncollimated chamber by an electronic "gate". Pulses from the collimated chamber in coincidence with these were passed to a 30-channel pulse analyzer (26), which measured their energy distribution. A detailed description of the electronic apparatus is given in Section IV(b).

The neutron source was the NRX heavy water pile at Chalk River. Most of the measurements were made with the chamber inside the thermal column. On a few occasions, where a lower flux of neutrons was sufficient, an external beam was used.

### III. Preparation of the Source

The source was prepared by the evaporation of a uranium-collodion solution on water. This source solution was prepared by mixing four parts of a solution of uranium acetate (2 mgm. per ml.) in amyl acetate with one part of a solution of collodion in ether (87 mgm. of collodion per ml.). A small quantity of the final solution ( $\sim 0.03$  ml.) was dropped onto a clean surface of distilled water. The solution spreads out quickly and uniformly to cover an area of about 100 sq. cm. and is allowed to dry for about 10 sec. The drying time is important since the uranium acetate is slowly soluble in water. With a quickly soluble salt (e.g., uranium nitrate) the uranium in the film may dissolve in the water before the film can be removed from the water surface. In preliminary trials with uranium nitrate and slowly drying films, up to 99% of the uranium was lost. Many variations of the materials used offer possibilities, but the combination of uranium acetate, amyl acetate, collodion, and water was found to



be the best of a wide variety tested and even with this prescription approximately 20% of the uranium was lost to the water.

The film was lifted from the water by means of a wire frame. A rectangular loop of wire was brought up underneath the center of the source. As the frame is withdrawn the film folds over the loop, forming a double layer. Removing a double film in this manner was found easier than handling a single film of twice the thickness.

The film was allowed to dry for one minute and then laid carefully over the collimator plate. This drying time was so chosen that the film was slightly moist, to provide proper adhesion to the plate. Excess surface moisture gives rise to fillets of water in the collimator holes, which dissolves uranium out of the film. As the film dries, a significant fraction of the fissile material is left deposited on the side walls of the collimator holes. Since such a deposit can "see" only into one chamber, it cannot give rise to truly coincident pulses and contributes only an objectionable background.

In preliminary experiments (when the sources were prepared by different techniques) four-fifths of the source material collected in such deposits in the collimator. This gave rise to a false-to-true counting ratio of 4:1 in the collimated chamber and a significant per cent of chance coincidences. In the final experiments the false-to-true counting ratio was about unity and the chance coincident counting rate was reduced to a negligible proportion (Section IV(c)).

#### IV. Experimental Conditions

##### (a) OPERATION OF THE CHAMBER

The chamber was tested under a wide range of voltage conditions. Cathode-grid fields from 5 to 400 v. per cm. were used. If this "collecting" field is too low, a portion of the ionization is lost through recombination, and the resulting pulses are not "saturated". Pulse amplitudes were measured for a series of field values until saturation was indicated by no further increase in pulse size with increase in the electric field. Saturation occurred for  $\alpha$ -pulses in pure argon at about 10 v. per cm. whereas fission fragments in an argon plus carbon dioxide mixture required cathode-grid fields of  $\sim 200$  v. per cm.

If the grid-collector field is not maintained sufficiently large relative to the cathode-grid field, the pulse size is decreased by loss of electrons to the grid. For the design of grid used, the theoretical minimum ratio required for these fields is about 3:1 according to Bunemann *et al.* (5). Our experimental value for this ratio of fields was 3.5:1, which is in reasonable agreement with the theory, considering nonuniformities in the fields and inaccuracies in grid construction. To ensure complete freedom from such losses a ratio of 4:1 was used in the experiment.

The type of gas used in the chamber is important. Negative ion formation by electron attachment must be avoided. The relatively immobile negative

ions give a slowly rising pulse which is not recorded by the fast amplifiers used here to obtain a good signal-to-noise ratio and a low chance coincidence rate. Even small impurities of electronegative gases must be eliminated. Argon, 99.9% pure, with less than five parts per million oxygen, was used. Argon, alone, however, suffers from the disadvantage of low electron mobility, and hence a long pulse rise time results.

The pulse collection time for a track of ionization is the time between the arrival of the first electrons in the grid-collector region and the arrival of the last electrons on the collector. Thus, if  $l_1$  is the projection of the length of the track in the direction of the field and  $l_2$  is the grid-collector spacing ( $l_2 = 1$  cm.), the collection time is

$$\frac{l_1}{W_1} + \frac{l_2}{W_2},$$

where  $W_1$  and  $W_2$  are the drift velocities of electrons in the cathode-grid and grid-collector fields respectively.

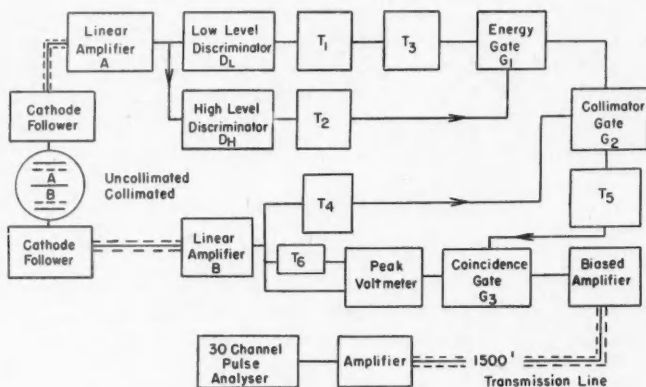


FIG. 2. Block diagram of electronic arrangement for coincident pulse measurement.

With a filling of pure argon and at field strengths of about 100 v. per cm.,  $W_1 \approx 4 \times 10^6$  cm. per sec. and  $W_2 \approx 8 \times 10^5$  cm. per sec. (Healey and Reed (14)), and consequently the maximum collection time was about 10  $\mu$ sec.

The addition of a few per cent carbon dioxide to the argon increases the electron mobilities so that  $W_1 \approx 3 \times 10^6$  cm. per sec.,  $W_2 \approx 6 \times 10^6$  cm. per sec., and the maximum collection time is reduced to about 1.5  $\mu$ sec. This allows much faster amplifier response and a corresponding reduction in the coincidence resolving time. The consequent improvement in noise background and chance coincident rate is discussed in Section IV(c). In addition, it was observed that with the argon plus carbon dioxide mixture less stringent conditions are imposed on gas purity. This may arise from the much lower agitational velocities of electrons in this mixture and the consequent reduction in the

probability of electron attachment to impurities such as water vapor and hydrogen sulphide. As mentioned above, however, the argon plus carbon dioxide mixture requires much higher fields to produce saturation.

### (b) THE ELECTRONIC EQUIPMENT

A block diagram of the general layout of the electronic equipment is shown in Fig. 2. Output pulses from each chamber are fed through cathode-followers to a pair of linear amplifiers. The amplified output from the uncollimated chamber is then fed through a system of discriminators, trigger circuits and gating stages ( $D_L$ ,  $D_H$ ,  $T_1$ ,  $T_2$ ,  $T_3$ ,  $T_4$ ,  $G_1$ ,  $G_2$ ) by means of which pulses lying within a selected energy interval trigger the coincidence mixer  $G_3$ . The pulses from the collimated chamber are converted into square pulses of the same amplitude by the "peak voltmeter" circuit ( $T_6$  controls the duration of these shaped pulses). Of these  $G_3$  passes only those that are in coincidence with the pulses of selected energy from the uncollimated chamber. These coincident pulses are then passed through a biased amplifier and their energy distribution is measured on a 30-channel pulse analyzer. The components of this system will now be described in detail.

(1) *The Cathode Followers (Fig. 3)*

As the chamber itself was in a high neutron flux, the bulk of the electronic equipment had to be operated some distance away. The output of the chamber was fed through cathode followers to avoid the loss in pulse amplitude that would have resulted if direct feeding of long cables had been employed. A point of interest is the low value of input resistance used. It is usual in this type of

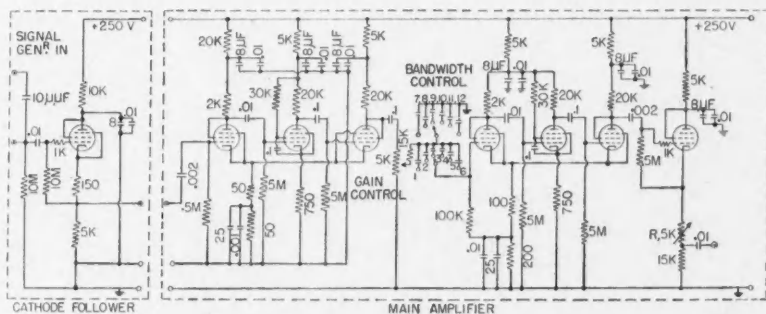


FIG. 3. Input cathode follower and main amplifier: circuit diagram. All valves are 12SH7's, filaments in series fed from a 250 v. stabilized supply. Gain control: wire wound resistors to give 4db steps. Control R is a fine gain control for balancing the two amplifiers.

*Band width control capacities  
(condenser banks ganged)*

1 = 0.001 $\mu\text{f.}$	7 = 0.001 $\mu\text{f.}$
2 = 0.0005 $\mu\text{f.}$	8 = 0.0005 $\mu\text{f.}$
3 = 0.00025 $\mu\text{f.}$	9 = 0.00025 $\mu\text{f.}$
4 = 100 $\mu\mu\text{f.}$	10 = 50 $\mu\mu\text{f.}$
5 = 50 $\mu\mu\text{f.}$	11 = 20 $\mu\mu\text{f.}$
6 = 20 $\mu\mu\text{f.}$	12 = 0 $\mu\mu\text{f.}$

work to use resistances of about  $10^9$  ohms in the interests of good signal-to-noise ratio. However, first circuit noise is in this case quite negligible compared with the noise resulting from  $\beta$ - and  $\gamma$ -ray ionization in the chamber. On the other hand, the steady current from this cause flowing through a resistance as high as  $10^9$  ohms was found to alter appreciably the potential of the collecting electrode (see Section IV(d)). This slight but somewhat inconvenient dependence of chamber operating conditions on ionization was eliminated by reducing this resistance to  $10^7$  ohms.

### (2) The Main Amplifier (Fig. 3)

The design of the main amplifier is virtually identical with that of Cranshaw and Harvey (6). Two high stability negative feed-back rings are separated by a condenser-resistance network which determines the pulse shape.

It is important to avoid a dependence of output amplitude on pulse rise time. Although the  $45^\circ$  collimation used restricts the spread of rise times considerably, the amplifier time constants have been chosen long enough to tolerate a variation from zero to the maximum (1.5  $\mu$ sec.) in the rise time. The "smoothing" and "differentiating" time constants used were 1 and 5  $\mu$ sec. respectively with a resultant pulse rise time of 2.5  $\mu$ sec. and decay time (from maximum to 20% of maximum)  $\sim 10$   $\mu$ sec. The expected independence was confirmed experimentally by measuring the ratio of  $\alpha$ -particle pulses to signal generator pulses (of effectively zero rise time) as a function of amplifier time constants.

Negative pulses of amplitude  $\sim 50$  v. were obtained at the amplifier outputs. The balancing of the amplifiers was achieved by the continuous gain control  $R$  in Fig. 3.

### (3) Coincidence Discriminator (Fig. 4)

So far the treatment of pulses from both chambers has been identical. The two outputs from the amplifier now enter the coincidence discriminator where those pulses from the uncollimated chamber lying in a chosen energy interval are selected.

Consider the energy "gating" of pulses from the uncollimated chamber ("uncollimated pulses"). These pulses are first amplified by a factor of four and passed to two similar discriminator and trigger circuits  $D_L T_1$  and  $D_H T_2$ , the detailed operation of which is described more fully in Appendix I.

If a pulse amplitude exceeds the level set by  $D_L$ ,  $T_1$  will fire; if, further, it exceeds the level of  $D_H$ ,  $T_2$  will fire.  $T_2$  is made to cancel  $T_1$  so that a gating pulse is passed through  $G_1$  only if the actuating pulse lies between the thresholds of  $D_L$  and  $D_H$ . This cancelling involves the use of an intermediate trigger circuit  $T_3$ . Referring to Fig. 5,  $T_3$  is adjusted to give an output pulse of length just greater than the rise time,  $T_2$  (and  $T_1$ ) are of length about twice  $T_3$ . Thus the back of the square wave from  $T_3$  always lies within the pulse from  $T_2$  at whatever point on the front of the input pulse  $T_2$  is fired. The wave  $T_3$  is differentiated with a 1  $\mu$ sec. time constant and applied to the grid of a normally

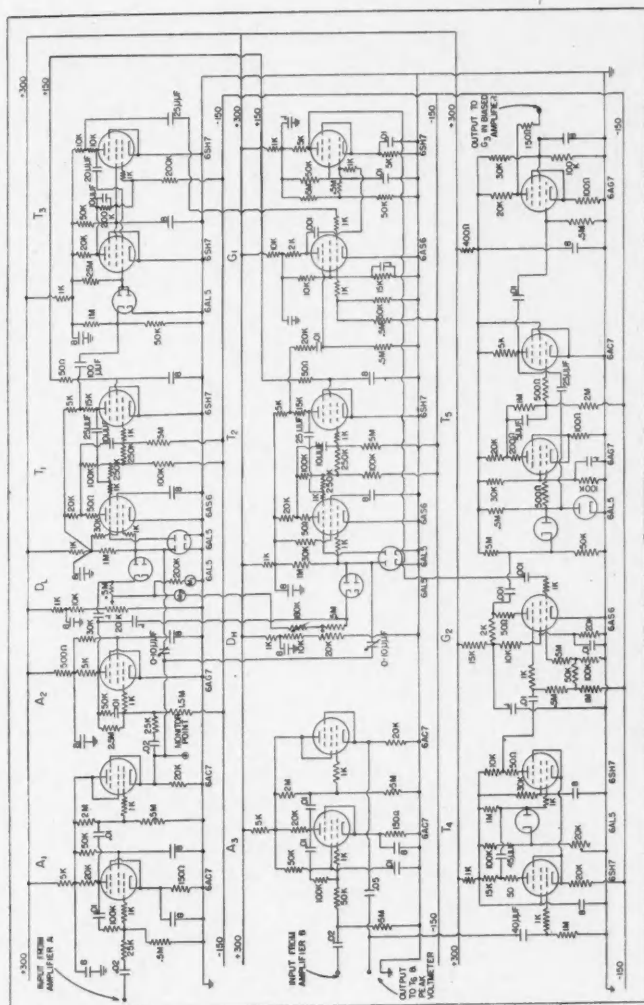


FIG. 4. Coincidence discriminator: circuit diagram.

The working of this circuit is best followed with the aid of the block diagram Fig. 2. The circuit sections  $A_1$  and  $A_3$  are two identical feed-back amplifiers and cathode follower stages to increase the main amplifier output (50 v.) to 100 v. maximum.  $A_2$  provides a further gain of two before the discriminators  $D_1$  and  $DH$ .

The 8  $\mu\text{f}$ . decoupling condensers are shunted by 0.001  $\mu\text{f}$ . condensers.

cut off 6AS6 valve. The negative output from  $T_2$  is applied to the suppressor. Consequently there appears on the anode of this gating stage ( $G_1$ ) a negative pulse if, and only if,  $D_L T_1$  fires and  $D_H T_2$  does not.

It was originally intended to derive from  $G_1$  a square wave which would open the pulse analyzer to a pulse from the collimated side of the chamber (via amplifier  $B$ ) since there was within the pulse analyzer a convenient way of gating pulses without introducing uncertainties into their amplitudes. How-

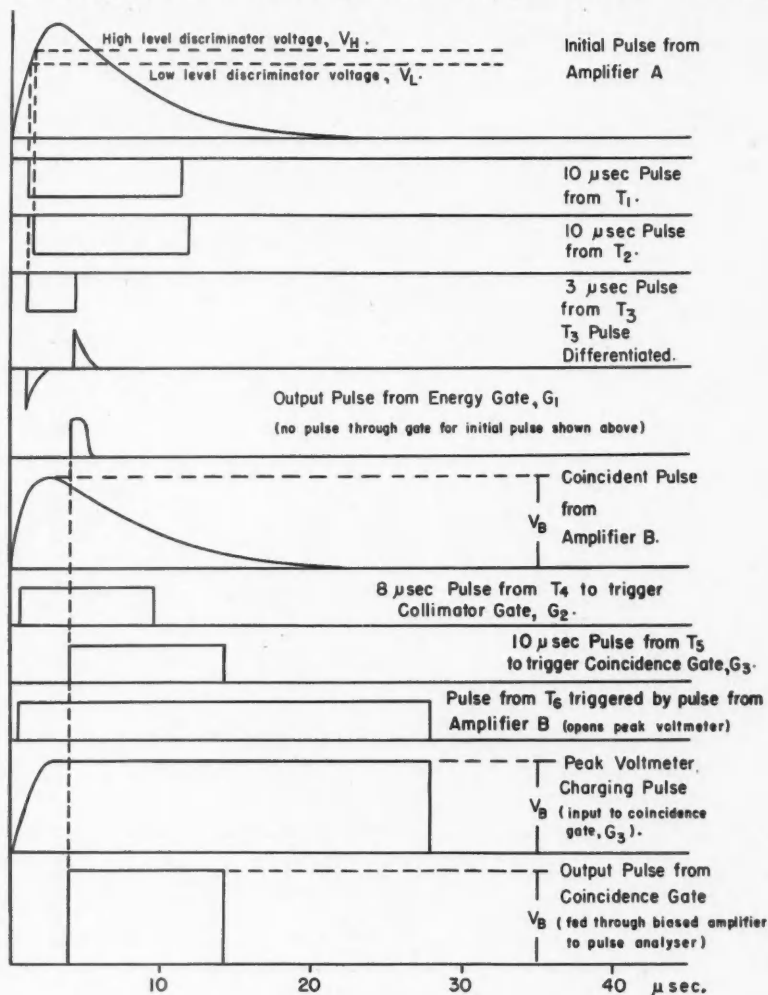


FIG. 5. Coincidence discriminator: wave-form diagram.

ever this would have involved a long (80  $\mu$ sec.) coincidence resolving time and resulted in a high chance coincidence rate. Consequently a coincidence stage of shorter resolving time was inserted between  $G_1$  and the pulse analyzer. This—called the “Collimator Gate” ( $G_2$ )—passes a pulse to  $T_6$  only if there is a coincident pulse from the collimated side, and thus assumes the onus of coincidence discrimination. For various reasons it was subsequently decided to operate the pulse analyzer at a large distance ( $\sim 1500$  ft.) from the rest of the equipment, and to avoid a separate lead for the gating pulses it was necessary to gate the collimated pulses on the spot using the gate  $G_3$  (see below). This scheme was not subject to the limitations (in resolving time) of the pulse analyzer and the reasons for the gate  $G_2$  eliminated. However  $G_2$  was retained and the gate  $G_3$  operated with a long resolving time.

The gating action of  $G_2$  is accomplished as follows. Any collimated pulse produces a positive square wave in  $T_4$ , which is applied to the suppressor grid of a 6AS6 valve, the control grid of which is connected to an inverted version of the output of  $G_1$ . Both grid and suppressor are normally biased beyond cutoff. Consequently a pulse appears on the anode only if both grid and suppressor are pulsed simultaneously. Clearly the resolving time which determines the chance coincidence rate is the sum of the durations of the wave forms from  $G_1$  and  $T_4$ . The former can be made very short, but there is a lower limit imposed on  $T_4$ . The wave  $G_1$  may be delayed from pulse onset time (at which point  $T_4$  fires) up to a time equal to the sum of the rise time and the duration of  $T_3$ , that is, approximately twice the input pulse rise time. Clearly the duration of  $T_4$  must be greater than this. Actually with the rise time of 2.5  $\mu$ sec. obtained from the amplifiers and  $T_3$  3  $\mu$ sec.,  $G_1$  was 2  $\mu$ sec. and  $T_4$  8  $\mu$ sec., giving a total resolving time of 10  $\mu$ sec. The duration of  $T_1$  (equal to  $T_2$ ) was chosen to be 10  $\mu$ sec.

The trigger circuit  $T_5$  produces a 10  $\mu$ sec. pulse to operate the coincidence gate  $G_3$ .

#### (4) Biased Amplifier Unit (Fig. 6)

The biased amplifier unit which contains the peak voltmeter and trigger circuit  $T_6$  is similar to the equipment described by Cranshaw and Harvey (6) with the small addition  $G_3$  to enable the gating to be carried out. (For a more detailed description of the circuit the paper of Cranshaw and Harvey should be consulted.)

Briefly, signals entering this unit are converted into square waves of adjustable length and of the same amplitude as the incoming pulses. This is accomplished by the switching trigger circuit  $V_1$ ,  $V_2$  (Fig. 6) and the peak voltmeter circuit  $D_3$  and  $C$ . The square-wave output is available at the cathode of  $V_5$ . In the original design the pulses then passed directly to the biasing or “cutting” stage  $V_6$  and the subsequent amplifier  $V_7$ , to which has been added a reversal stage  $V_9$  and an output cathode follower  $V_{10}$ . The advantage of using square waves is that the output pulse duration is independent of the amount of cutting, and thus subsequent amplifiers need not be of very wide band width.

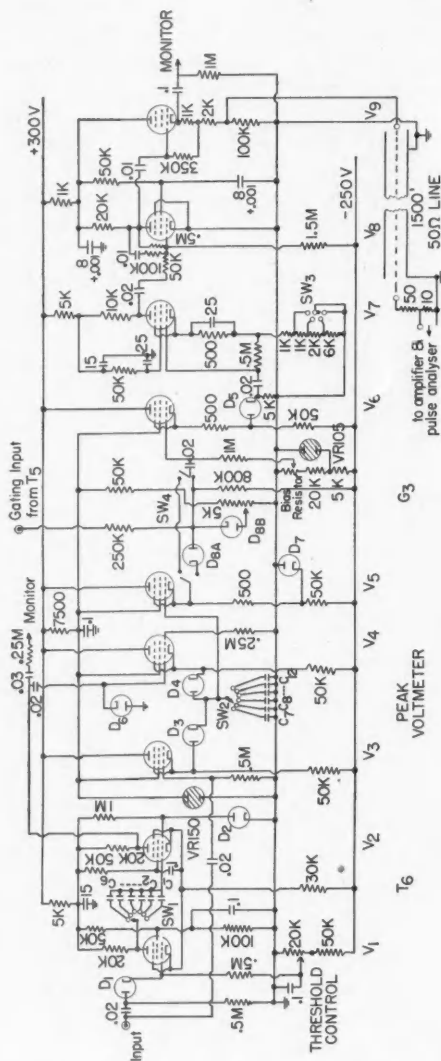


FIG. 6. Biased amplifier; circuit diagram.

Bias resistor: wire wound resistor assembly with coarse (step) and fine (continuous) controls. Total resistance = 50K.

SW1 controls the length of pulse

SW2 selects the reservoir capacity

SW3 controls the gain of the amplifier stage V7

SW4 permits ungated operation.

Components:

$C_1 = 0.005 \mu\text{f}$ .

$C_2 = 0.002 \mu\text{f}$ .

$C_3 = 0.001 \mu\text{f}$ .

$C_4 = 0.0005 \mu\text{f}$ .

$C_5 = 0.0002 \mu\text{f}$ .

$C_6 = 0.0001 \mu\text{f}$ .

$C_7 = 0.0001 \mu\text{f}$ .

$C_8 = 0.0001 \mu\text{f}$ .

$C_9 = 0.0001 \mu\text{f}$ .

$C_{10} = 0.0001 \mu\text{f}$ .

$C_{11} = 0.0001 \mu\text{f}$ .

$C_{12} = 0.0001 \mu\text{f}$ .

$C_{13} = 0.0001 \mu\text{f}$ .

$C_{14} = 0.0001 \mu\text{f}$ .

$C_{15} = 0.0001 \mu\text{f}$ .

$C_{16} = 0.0001 \mu\text{f}$ .

$C_{17} = 0.0001 \mu\text{f}$ .

$C_{18} = 0.0001 \mu\text{f}$ .

$C_{19} = 0.0001 \mu\text{f}$ .

$C_{20} = 0.0001 \mu\text{f}$ .

$C_{21} = 0.0001 \mu\text{f}$ .

$C_{22} = 0.0001 \mu\text{f}$ .

$C_{23} = 0.0001 \mu\text{f}$ .

$C_{24} = 0.0001 \mu\text{f}$ .

$C_{25} = 0.0001 \mu\text{f}$ .

$C_{26} = 0.0001 \mu\text{f}$ .

$C_{27} = 0.0001 \mu\text{f}$ .

$C_{28} = 0.0001 \mu\text{f}$ .

$C_{29} = 0.0001 \mu\text{f}$ .

$C_{30} = 0.0001 \mu\text{f}$ .

$C_{31} = 0.0001 \mu\text{f}$ .

$C_{32} = 0.0001 \mu\text{f}$ .

$C_{33} = 0.0001 \mu\text{f}$ .

$C_{34} = 0.0001 \mu\text{f}$ .

$C_{35} = 0.0001 \mu\text{f}$ .

$C_{36} = 0.0001 \mu\text{f}$ .

$C_{37} = 0.0001 \mu\text{f}$ .

$C_{38} = 0.0001 \mu\text{f}$ .

$C_{39} = 0.0001 \mu\text{f}$ .

$C_{40} = 0.0001 \mu\text{f}$ .

$C_{41} = 0.0001 \mu\text{f}$ .

$C_{42} = 0.0001 \mu\text{f}$ .

$C_{43} = 0.0001 \mu\text{f}$ .

$C_{44} = 0.0001 \mu\text{f}$ .

$C_{45} = 0.0001 \mu\text{f}$ .

$C_{46} = 0.0001 \mu\text{f}$ .

$C_{47} = 0.0001 \mu\text{f}$ .

$C_{48} = 0.0001 \mu\text{f}$ .

$C_{49} = 0.0001 \mu\text{f}$ .

$C_{50} = 0.0001 \mu\text{f}$ .

$C_{51} = 0.0001 \mu\text{f}$ .

$C_{52} = 0.0001 \mu\text{f}$ .

$C_{53} = 0.0001 \mu\text{f}$ .

$C_{54} = 0.0001 \mu\text{f}$ .

$C_{55} = 0.0001 \mu\text{f}$ .

$C_{56} = 0.0001 \mu\text{f}$ .

$C_{57} = 0.0001 \mu\text{f}$ .

$C_{58} = 0.0001 \mu\text{f}$ .

$C_{59} = 0.0001 \mu\text{f}$ .

$C_{60} = 0.0001 \mu\text{f}$ .

$C_{61} = 0.0001 \mu\text{f}$ .

$C_{62} = 0.0001 \mu\text{f}$ .

$C_{63} = 0.0001 \mu\text{f}$ .

$C_{64} = 0.0001 \mu\text{f}$ .

$C_{65} = 0.0001 \mu\text{f}$ .

$C_{66} = 0.0001 \mu\text{f}$ .

$C_{67} = 0.0001 \mu\text{f}$ .

$C_{68} = 0.0001 \mu\text{f}$ .

$C_{69} = 0.0001 \mu\text{f}$ .

$C_{70} = 0.0001 \mu\text{f}$ .

$C_{71} = 0.0001 \mu\text{f}$ .

$C_{72} = 0.0001 \mu\text{f}$ .

$C_{73} = 0.0001 \mu\text{f}$ .

$C_{74} = 0.0001 \mu\text{f}$ .

$C_{75} = 0.0001 \mu\text{f}$ .

$C_{76} = 0.0001 \mu\text{f}$ .

$C_{77} = 0.0001 \mu\text{f}$ .

$C_{78} = 0.0001 \mu\text{f}$ .

$C_{79} = 0.0001 \mu\text{f}$ .

$C_{80} = 0.0001 \mu\text{f}$ .

$C_{81} = 0.0001 \mu\text{f}$ .

$C_{82} = 0.0001 \mu\text{f}$ .

$C_{83} = 0.0001 \mu\text{f}$ .

$C_{84} = 0.0001 \mu\text{f}$ .

$C_{85} = 0.0001 \mu\text{f}$ .

$C_{86} = 0.0001 \mu\text{f}$ .

$C_{87} = 0.0001 \mu\text{f}$ .

$C_{88} = 0.0001 \mu\text{f}$ .

$C_{89} = 0.0001 \mu\text{f}$ .

$C_{90} = 0.0001 \mu\text{f}$ .

$C_{91} = 0.0001 \mu\text{f}$ .

$C_{92} = 0.0001 \mu\text{f}$ .

$C_{93} = 0.0001 \mu\text{f}$ .

$C_{94} = 0.0001 \mu\text{f}$ .

$C_{95} = 0.0001 \mu\text{f}$ .

$C_{96} = 0.0001 \mu\text{f}$ .

$C_{97} = 0.0001 \mu\text{f}$ .

$C_{98} = 0.0001 \mu\text{f}$ .

$C_{99} = 0.0001 \mu\text{f}$ .

$C_{100} = 0.0001 \mu\text{f}$ .

$C_{101} = 0.0001 \mu\text{f}$ .

$C_{102} = 0.0001 \mu\text{f}$ .

$C_{103} = 0.0001 \mu\text{f}$ .

$C_{104} = 0.0001 \mu\text{f}$ .

$C_{105} = 0.0001 \mu\text{f}$ .

$C_{106} = 0.0001 \mu\text{f}$ .

$C_{107} = 0.0001 \mu\text{f}$ .

$C_{108} = 0.0001 \mu\text{f}$ .

$C_{109} = 0.0001 \mu\text{f}$ .

$C_{110} = 0.0001 \mu\text{f}$ .

$C_{111} = 0.0001 \mu\text{f}$ .

$C_{112} = 0.0001 \mu\text{f}$ .

$C_{113} = 0.0001 \mu\text{f}$ .

$C_{114} = 0.0001 \mu\text{f}$ .

$C_{115} = 0.0001 \mu\text{f}$ .

$C_{116} = 0.0001 \mu\text{f}$ .

$C_{117} = 0.0001 \mu\text{f}$ .

$C_{118} = 0.0001 \mu\text{f}$ .

$C_{119} = 0.0001 \mu\text{f}$ .

$C_{120} = 0.0001 \mu\text{f}$ .

$C_{121} = 0.0001 \mu\text{f}$ .

$C_{122} = 0.0001 \mu\text{f}$ .

$C_{123} = 0.0001 \mu\text{f}$ .

$C_{124} = 0.0001 \mu\text{f}$ .

$C_{125} = 0.0001 \mu\text{f}$ .

$C_{126} = 0.0001 \mu\text{f}$ .

$C_{127} = 0.0001 \mu\text{f}$ .

$C_{128} = 0.0001 \mu\text{f}$ .

$C_{129} = 0.0001 \mu\text{f}$ .

$C_{130} = 0.0001 \mu\text{f}$ .

$C_{131} = 0.0001 \mu\text{f}$ .

$C_{132} = 0.0001 \mu\text{f}$ .

$C_{133} = 0.0001 \mu\text{f}$ .

$C_{134} = 0.0001 \mu\text{f}$ .

$C_{135} = 0.0001 \mu\text{f}$ .

$C_{136} = 0.0001 \mu\text{f}$ .

$C_{137} = 0.0001 \mu\text{f}$ .

$C_{138} = 0.0001 \mu\text{f}$ .

$C_{139} = 0.0001 \mu\text{f}$ .

$C_{140} = 0.0001 \mu\text{f}$ .

$C_{141} = 0.0001 \mu\text{f}$ .

$C_{142} = 0.0001 \mu\text{f}$ .

$C_{143} = 0.0001 \mu\text{f}$ .

$C_{144} = 0.0001 \mu\text{f}$ .

$C_{145} = 0.0001 \mu\text{f}$ .

$C_{146} = 0.0001 \mu\text{f}$ .

$C_{147} = 0.0001 \mu\text{f}$ .

$C_{148} = 0.0001 \mu\text{f}$ .

$C_{149} = 0.0001 \mu\text{f}$ .

$C_{150} = 0.0001 \mu\text{f}$ .

$C_{151} = 0.0001 \mu\text{f}$ .

$C_{152} = 0.0001 \mu\text{f}$ .

$C_{153} = 0.0001 \mu\text{f}$ .

$C_{154} = 0.0001 \mu\text{f}$ .

$C_{155} = 0.0001 \mu\text{f}$ .

$C_{156} = 0.0001 \mu\text{f}$ .

$C_{157} = 0.0001 \mu\text{f}$ .

$C_{158} = 0.0001 \mu\text{f}$ .

$C_{159} = 0.0001 \mu\text{f}$ .

$C_{160} = 0.0001 \mu\text{f}$ .

$C_{161} = 0.0001 \mu\text{f}$ .

$C_{162} = 0.0001 \mu\text{f}$ .

$C_{163} = 0.0001 \mu\text{f}$ .

$C_{164} = 0.0001 \mu\text{f}$ .

$C_{165} = 0.0001 \mu\text{f}$ .

$C_{166} = 0.0001 \mu\text{f}$ .

$C_{167} = 0.0001 \mu\text{f}$ .

$C_{168} = 0.0001 \mu\text{f}$ .

$C_{169} = 0.0001 \mu\text{f}$ .

$C_{170} = 0.0001 \mu\text{f}$ .

$C_{171} = 0.0001 \mu\text{f}$ .

$C_{172} = 0.0001 \mu\text{f}$ .

$C_{173} = 0.0001 \mu\text{f}$ .

$C_{174} = 0.0001 \mu\text{f}$ .

$C_{175} = 0.0001 \mu\text{f}$ .

$C_{176} = 0.0001 \mu\text{f}$ .

$C_{177} = 0.0001 \mu\text{f}$ .

$C_{178} = 0.0001 \mu\text{f}$ .

$C_{179} = 0.0001 \mu\text{f}$ .

$C_{180} = 0.0001 \mu\text{f}$ .

$C_{181} = 0.0001 \mu\text{f}$ .

$C_{182} = 0.0001 \mu\text{f}$ .

$C_{183} = 0.0001 \mu\text{f}$ .

$C_{184} = 0.0001 \mu\text{f}$ .

$C_{185} = 0.0001 \mu\text{f}$ .

$C_{186} = 0.0001 \mu\text{f}$ .

$C_{187} = 0.0001 \mu\text{f}$ .

$C_{188} = 0.0001 \mu\text{f}$ .

$C_{189} = 0.0001 \mu\text{f}$ .

$C_{190} = 0.0001 \mu\text{f}$ .

$C_{191} = 0.0001 \mu\text{f}$ .

$C_{192} = 0.0001 \mu\text{f}$ .

$C_{193} = 0.0001 \mu\text{f}$ .

$C_{194} = 0.0001 \mu\$



The gating stage  $G_3$  was inserted between  $V_5$  and  $V_6$  and operates as follows. Unless the circuit  $T_5$  is operated the gating input line is at +30 v. approximately. In this condition  $V_{8B}$  is conducting; its cathode potential is determined by  $R_2$ , so long as it is more negative than the cathode of  $V_{8A}$  (with this limitation  $R_2$  acts as a "zero-set"). If  $T_5$  is triggered, by coincident pulses, the gating line will rise to +300 v. approximately.  $V_{8B}$  now cuts off and  $V_{8A}$  opens, its anode rising to the same potential as the cathode of  $V_5$ , i.e., to the height of the pulse from the collimated chamber.

In this experiment the biased amplifier was used merely to bias the pulses so that the range of fission energies extended over the whole of the pulse analyzer range instead of just the upper half. This of course is a simple matter not requiring the elaboration of the circuit used, which was designed to provide high resolution. However the equipment was available and was quite suitable for this role.

The output cathode follower of the biased amplifier provided a convenient local monitoring point. The cathode circuit was completed by a 1500 ft. 50 ohm. transmission line, properly terminated at the far end, feeding the step-up amplifier and pulse analyzer. This amplifier comprised a ring-of-three circuit, similar to one of the stages in the main amplifier, followed by an output stage capable of providing the +100 v. swing necessary to drive the pulse analyzer. This instrument has been described by Westcott and Hanna (26).

### (c) CHANCE COINCIDENCES AND THE PULSE SPECTRUM

Any system with finite pulse lengths and resolving times will produce results which contain some spurious information. In this section we shall examine the quality and quantity of such erroneous data in the present experiment.

Spurious pulses arise from two causes: firstly, overlapping of pulses when two occur within a time defined as the pulse length and, secondly, purely chance coincidences. These effects become the more serious as the counting rate increases, and it is important to consider what limit on counting rate is dictated by these spurious effects.

The phenomenon of pulse overlapping or "build-up" occurs when the measured amplitude of a pulse is increased by the tail of a previous one. It is not specific to this problem but arises whenever pulse heights are being measured. Obviously, it results in a smearing of an energy distribution in the direction of higher energy; but, for a continuous distribution, the calculation of the effect in detail is very tedious. We limit the discussion here to a semiquantitative appraisal of a much simplified situation so as to demonstrate that the smearing effect, whatever its detailed nature, is of very small importance under the conditions of this experiment.

Let  $N$  counts per second be the counting rate in the uncollimated chamber,  $CN$  counts per second the rate of genuine coincidences in both chambers, and  $CNR$  counts per second the counting rate in the collimated chamber.

The factor  $R$  arises from the material deposited in the collimator holes which cannot give rise to true coincidences as pointed out in Section III.

A fraction,  $f$ , of the  $N$  counts per second, lying in a chosen energy interval is selected ( $f$  depends on the width and position of the energy gate). The genuine coincidence rate,  $CfN$  will be compared with the build-up and chance coincidence rate.

### 1. Build-ups

It should be pointed out that we are concerned here with the effect of pulses neighboring (in time) on the two pulses of a genuine coincidence only. Chance coincidence pairs which are affected by build-ups are automatically included (as a very small minority) in the chance coincidence rate (part 2).

#### (i) In the Collimated Chamber

Since the total counting rate in this chamber is  $CNR$ , the chance of a pulse occurring  $t_1$  sec. before or  $t_2$  sec. after any given pulse is  $CNR(t_1 + t_2)$ . The genuine coincidence rate is  $CfN$ ; therefore the build-up rate is  $CfN CNR(t_1 + t_2)$ . The first term involving  $t_1$  expresses the chance of the true pulse sitting on the tail of a preceding one. The value of  $t_1$  depends on the pulse shape and the amount of distortion to be considered. It will be denoted by  $a\tau$ , where  $\tau$  is the time constant of the pulse fall and  $a$  is a factor depending on the distortion allowed. The second term involving  $t_2$  arises from a pulse following the true pulse whose amplitude is being recorded. The peak voltmeter circuit measures the maximum amplitude reached during the time  $t_R + t_3 + t_5$ , where  $t_R$ ,  $t_3$ , and  $t_5$  are the rise time, and the pulse lengths in trigger circuits  $T_3$ , and  $T_5$  respectively (see Fig. 5). If, then, a pulse occurs within this time after the true one and is of larger amplitude (usually by virtue of the fact that it is sitting on the tail of the true one) a false count will be recorded. The time  $t_2$  must include a factor determined by how much larger the distorted amplitude of the second pulse is, and will be denoted by  $p(t_R + t_3 + t_5)$ .

Let us illustrate the magnitude of these effects by some numerical examples. For this purpose we require the decay time  $\tau$  defined as the time required for the pulse to decay to 20% of its maximum amplitude. The time  $\tau$  was measured to be 12.5  $\mu$ sec. (see also Appendix II).

If  $a = 1$ , then build-up pulses of the first type appear as distortions of 20% or more in amplitude. The number of such pulses is given by  $CfN CNR \tau$  or as a per cent of true coincidence,  $CNR \tau \times 100$ . Typical values are

$$N = 200 \text{ counts per sec.}$$

$$C = 1/40$$

$$R = 2.$$

$\therefore$  per cent pulses distorted by  $> 20\%$  in amplitude

$$= 1/40 \times 200 \times 2 \times 12 \times 10^{-6} \times 100 = 0.012\%.$$

For  $a = 5$  it is shown in Appendix II that the pulse has decreased to 0.002%

of its maximum value in the time  $5\tau$ . Hence 0.06% of the pulses are build-ups suffering a distortion of  $> 0.002\%$ . It has been assumed in these calculations that all pulses are of equal size. The variation in pulse size throughout the fission spectrum results in a larger per cent distortion on the low energy pulses but cannot substantially alter these results.

For build-ups of the second kind we may use similar arguments and if we retain the fiction of pulses of equal amplitude the calculation is quite simple. In the time  $(t_R + t_a + t_b) = (2.5 + 8 + 10) \approx 20 \mu\text{sec.}$ , we find that a pulse decays to 3% of its maximum amplitude. Hence if we choose  $p = 1$  (its maximum value),  $CNR(20 \times 10^{-6}) \times 100 = 0.02\%$  of the pulses are distorted by  $> 3\%$ . This 0.02% includes the cases of pulses of widely different initial amplitude from a true pulse being recorded. Furthermore, with a continuous distribution in pulse size, the operation of the peak voltmeter circuit permits a distorted measurement only when the second pulse is of larger amplitude than the true pulse.

#### (ii) In the Uncollimated Chamber

The counting rate of pulses in this chamber which are coincident with collimated pulses is  $CN$ . With a total counting rate  $N$ , the counting rate for build-ups is  $CN Nb \tau$ , where  $b$  is a factor, similar to  $a$  above, giving a measure of the per cent distortion considered when the true pulse falls on the tail of a preceding one. The factor  $b$ , however, is more restrictive than  $a$  since the amplitude distortions of significance in this case are only those which introduce or remove pulses from the selected energy band. There is a contribution from build-ups of the second kind, that is when a pulse sitting on the tail of the true pulse opens the energy gate. This pulse must clearly lie within the time  $\tau_c$  (the coincidence resolving time,  $\sim 10 \mu\text{sec.}$ ) after the true one. Apart from this additional restriction the effect is much the same as that of build-ups of the first kind. Consequently only the latter will be illustrated numerically.

The energy gate selects a fraction  $f'$  of the coincident pulses.  $f'$  is not exactly equal to  $f$  but since the build-up rate decreases rapidly for large amplitude shifts and since in any case the number introduced into the selected band is approximately equal to the number removed, it is reasonable to replace  $f'$  by  $f$  in practice. This means that the energy gate is opened  $cfN Nb \tau$  times per second by pulses (in true coincidence with collimated pulses) which have been distorted by build-ups. This quantity gives, therefore, the number of collimated pulses which are false because they are actually in coincidence with pulses lying outside the selected energy range. This effect will obviously depend on the position and width of the energy gate. For simplicity we will again assume equal amplitude pulses of, say, 70 Mev. For errors greater than 5% these 70 Mev. pulses must trigger a gate whose lower level is 73.5 Mev. The effect will be computed for a 5 Mev. gate width. This gate will be opened if the triggering pulse occurs while the amplitude of a preceding pulse lies between 8.5 and 3.5 Mev. This time, which is  $b\tau$ , above, is given in Appendix II as  $(18.1 - 13.7) = 4.4 \mu\text{sec.}$

The per cent rate of these build-ups is therefore

$$Nb\tau \times 100 = 200 \times 4.4 \times 10^{-6} \times 100 = 0.09\%.$$

The effect of build-up in the uncollimated chamber produces a higher counting rate of false information than do build-ups in the collimated chamber but the range of error is more restricted. Thus in the case cited 1 in 1000 of the pulses opening the energy gate will be more than 5%, but none more than 12% in error. For a continuous spectrum of pulses the range of error is not thus restricted, but the number of pulses with a given error decreases rapidly as this error increases.

## 2. Chance Coincidences

For an ideal system with  $R = 1$  there are no chance coincidences. Each count in the collimated chamber is accompanied by a true coincidence count in the uncollimated chamber and since the coincidence resolving time,  $\tau_c$ , is less than the pulse length,  $\tau$ , any second pulse occurring within  $\tau_c$  falls into the classification of a build-up. Thus it is only the source deposits within the collimator holes that give rise to chance coincidences and the counting rate for these spurious pulses in the collimated chamber is  $C(R - 1)N$ .

The counting rate from the uncollimated chamber at  $G_2$  is  $fN$ . Consequently, the chance coincidence rate is  $fN CN(R - 1)\tau_c$ .

As a per cent of the true coincidence rate the chance rate,  $N(R - 1)\tau_c$ ,

$$= 200 \times 10 \times 10^{-6} \times 100 = 0.2\%,$$

for  $\tau_c = 10 \mu\text{sec.}$  and  $R = 2$  (see Section III).

In contrast to build-up distortions, the chance coincidence pulses are distributed in a normal fission spectrum. As mentioned in Section III, the source conditions were much worse in preliminary experiments where  $R$  was 5.4. In addition, pure argon was used as a chamber filling for these runs and consequently a resolving time  $\tau_c$  of  $32 \mu\text{sec.}$  was required. Furthermore a counting rate of  $N = 500$  counts per second was used. The resulting per cent of chance coincidences,  $500 \times 4.4 \times 32 \times 10^{-6} \times 100 = 7\%$ , produced a considerable distortion in the distributions.

## (d) THERMAL NOISE AND $\beta$ - $\gamma$ BACKGROUND

There are two causes of the "noise" apparent at the amplifier output: firstly, thermal noise in the cathode follower and the first circuit of the main amplifier and, secondly, pulses from the  $\beta$ - $\gamma$  background in the chamber. The first effect is much smaller than the second. The equivalent value in kev. for the standard deviation of a signal generator pulse distribution obtained in the absence of  $\beta$ - $\gamma$  background was about 65 kev. This is about twice the optimum value attainable, but is reasonable considering that the circuit employed involved two "first circuit" noise sources and a low input impedance.

The second effect, under the conditions of irradiation employed in the experiment, gave rise to an equivalent standard deviation of signal generator pulses of 450 kev. The effect may be understood semiquantitatively by the

following argument. Suppose (for various reasons)  $n$   $\beta$ -particles traverse the chamber per second giving an average pulse size corresponding to an energy  $E$ . When  $n$  is large compared to  $1/\tau$ , where  $\tau$  is a measure of the pulse duration, a steady current flows which is subject to the usual statistical fluctuations of random phenomena. The standard deviation would then be of the order of  $(n\tau)^{1/2}$  in the number of  $\beta$  pulses per amplifier pulse duration; that is, a Gaussian distribution in amplitude of pulses (of a frequency  $\sim 1/\tau$ ) of standard deviation  $\sigma_\beta = E(n\tau)^{1/2}$ .

In argon a fast  $\beta$  particle produces about 90 ion pairs per cm. The average track length in the chamber is about 10 cm. Thus on an energy scale corresponding to 28 ev. per ion pair,  $E = 90 \times 10 \times 28 \approx 25$  kev.  $\tau \approx 10^{-6}$  sec. The quantity  $n$  is a little difficult to determine but one may make an estimate from this knowledge that there is  $\sim 1\gamma$  per thermal neutron in the pile flux and this may well swamp any local  $\beta$ - $\gamma$  process (in an aluminum chamber). If we assume an efficiency for the production of  $\beta$ 's by  $\gamma$  quanta of  $10^{-2}$  and a thermal neutron flux of  $\rho v = 10^8$  neutrons per sq. cm. per sec. over an area of 10 sq. cm.

$$\begin{aligned} n &= 10^8 \times 10^2 \times 10^{-2} = 10^8 \text{ sec.}^{-1} \\ n\tau &= 10^3 \\ \sigma_\beta &\sim 750 \text{ kev.} \end{aligned}$$

(The mean current  $= n \times 90 \times 10 \times 1.6 \times 10^{-19} = 1.5 \times 10^{-8}$  amp.)

#### (e) CALIBRATION AND DISCUSSION OF ERRORS IN THE ABSOLUTE ENERGY MEASUREMENTS

Measurements of energy were made effectively at the chamber collecting electrodes by feeding pulses to these points from a signal generator through two small identical condensers (Fig. 3). If a signal generator pulse of amplitude  $V$  volts is applied through a coupling condenser of  $C$  farads it will produce a pulse at the input of the amplifier equal to the collection of a charge due to ionization of  $VC$  coulombs, independent of the total input capacity provided  $C$  is always connected. Clearly if  $V$  and  $C$  are both known this provides an absolute method of calibration. Pulses from the signal generator were thus treated in exactly the same way as ionization pulses, and any nonlinearity in the amplifier system was readily avoided.

Attenuators in the signal generator allowed the pulse amplitude to be varied over a wide range in accurately known small steps. Such pulses fed into the collimated side were recorded on the pulse analyzer, thus calibrating the pulse analyzer channel against signal generator millivolts, Fig. 7(a). These signal generator pulses were likewise fed into the uncollimated chamber. For each pulse amplitude, the firing level of the low level discriminator  $D_L$  was increased until  $T_1$  just failed to fire. In this way  $D_L$  was calibrated in terms of signal generator millivolts, Fig. 7(b). Calibration of  $D_H$  followed automatically from its voltage relation to  $D_L$ . It is worth mentioning here that, since the equipment

associated with each chamber was calibrated directly from the signal generator, there was no necessity for accurate balancing of the two main amplifiers.

Absolute calibration was obtained by measuring the natural  $\alpha$ -particle energies from the sources in terms of signal generator millivolts and using the known energies of these particles ( $U^{238} - 4.823$  Mev.,  $U^{235} - 4.396$  Mev.) to obtain the Mev. equivalent of one millivolt.

Such a method assumes, of course, that the number of electron volts per ion pair,  $w$ , in argon is the same for fission fragments as for  $\alpha$ -particles. As yet no accurate experiments have been performed to test this assumption. Henderson (15) measured fission energies by a calorimetric method and ob-

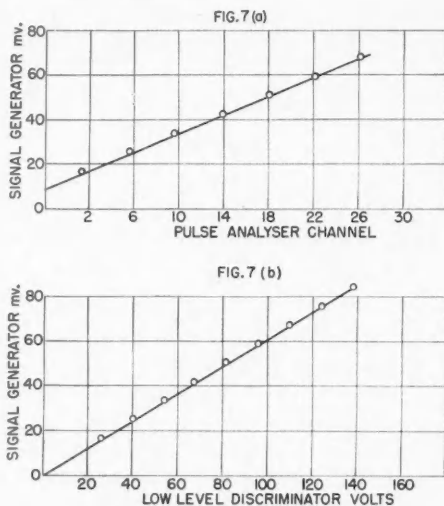


FIG. 7. (a) Calibration curve for pulse analyzer.  
(b) Calibration curve for discriminator.

tained  $177 \pm 1.8$  Mev. This measurement included part of the  $\beta$  decay energy of the fragments but very little of the neutron,  $\gamma$  or high energy  $\beta$  radiation. Henderson estimated that the kinetic energy was  $12 \pm 6$  Mev. less or  $165 \pm 8$  Mev. Ionization chamber measurements give a somewhat lower value. The mean of the values obtained by Deutsch and Ramsey (8) and by the present experimenters (see Table I) is 152.8 Mev. These results appear to be the most reliable since in each case the source was very thin and the emergent angle of the fragment track was restricted by a collimator. In our case there is a correction of about 2% (see below) to be made for source thickness and collimator loss: a similar correction would seem to be necessary in Deutsch and Ramsey's experiment. The corrected mean value then becomes 155.8 Mev.

Theoretically one would expect  $w$  to increase for fission fragments (relative to  $\alpha$ -particles) since the heavy fragment has a velocity only 0.6 times that of a 4.5 Mev.  $\alpha$ -particle. If we assume that  $w$  is the same for fission fragments and  $\alpha$ -particles of the same velocity,  $w$  for the heavy fragment will be 2% greater than for a 4.5 Mev.  $\alpha$ -particle, but for the light fragment will be almost the same. This variation of  $w$  with  $\alpha$ -particle velocity is discussed in the paper of Cranshaw and Harvey (6). The value of the total kinetic energy thus corrected is 157 Mev. We estimate the limits of error here as about  $\pm 3$  Mev., and there would seem consequently to be no serious discrepancy between the ionization and calorimetric measurements.

TABLE I  
SLOW NEUTRON FISSION IN  $U^{235}$

	Jentschke and Prankl	Flammersfeld, Jensen, and Gentner	Jentschke	Deutsch and Ramsey	Fowler and Rosen	Present experi- ment
Most probable energy of light group, Mev.	91	92	92.5	94	92.5	92.7
Most probable energy of heavy group, Mev.	57	59	65	60	61.2	59.0
Ratio of most probable energies	1.60	1.56	1.47	1.57	1.51	1.57
Most probable mass ratio of coincident pairs (on an equal ratio-interval curve)	—	—	—	1.49	—	1.485
Width at half-maximum of high energy peak, Mev.	17	15	13	12	15	12
Width at half-maximum of low energy peak, Mev.	22	19	20	19	24.5	20
Ratio of peak heights	1.3	1.22	1.49	1.57	1.46	1.37
Foil thickness, mm. air equivalent	0.05	0.1 (backing 0.34)	0.15	0.1	0.2	0.1

The 2% correction to the energy measurements mentioned above arises from two sources: (1) loss of energy by self-absorption in the source, and (2) loss of ions in the collimator.

The energy absorption in the source may be evaluated from the value 6.5 Mev. per mm. given by West (25) for the initial energy loss of an average fission fragment in standard nitrogen. A source (85% collodion, 15% uranium) of thickness 14  $\mu$ gm. per sq. cm. is the equivalent of  $\sim 0.1$  mm. of air and hence gives rise to an energy loss of 0.6 to 0.9 Mev. depending on the path of the particle through the source. The mean loss from this cause is, therefore,  $\sim 0.75$  Mev. or  $\sim 1\%$ . The  $\alpha$ -particle loss from the same cause is  $\sim 0.2\%$ . Since the fission energies are determined by comparison with  $\alpha$ -energies, the error in fission energies from this cause is about 0.8%.

The collimator losses arise from the recombination of ions produced in the weak field region inside the collimator holes. For the 0.010 in. collimator and



65 cm. gas pressure used the energy loss (assuming complete recombination but neglecting obliquity of track) is at most  $0.010 \times 25.4 \times 6.5 \times 0.9 = 1.25$  Mev. or 1.7%. The corresponding  $\alpha$ -particle loss is 0.4% and hence the net error is 1.3%. The combined error from both causes is therefore  $\sim 2\%$ .

## V. Experimental Results

### (a) RESULTS WITH $U^{235}$

The energy distribution was measured, first, with the energy gate wide open so that the whole range of fragment energies was recorded. The result is the usual double-humped curve shown in Fig. 8. The details of the distribution

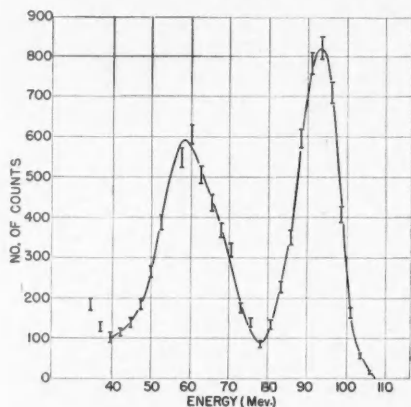


FIG. 8. Spectrum of fragment energies with  $U^{235}$ . Distribution measured with energy gate wide open.

were then examined by measuring the distributions associated with an energy gate 5 Mev. wide. The gate was set on the low energy end of the spectrum and moved up in discrete steps of 5 Mev. In each case the coincident distribution was recorded. The results are shown in Fig. 9 (a-m). In these figures the normal distribution curve of Fig. 8 is shown by a broken curve on a reduced scale, and the gating position relative to this curve is indicated. The curves are normalized to equal counting times: the standard error (of counting) computed from the unnormalized curves, is shown for the maxima only. The curves are uncorrected for the source and collimator losses discussed in Section IV(e). The corrected values are:

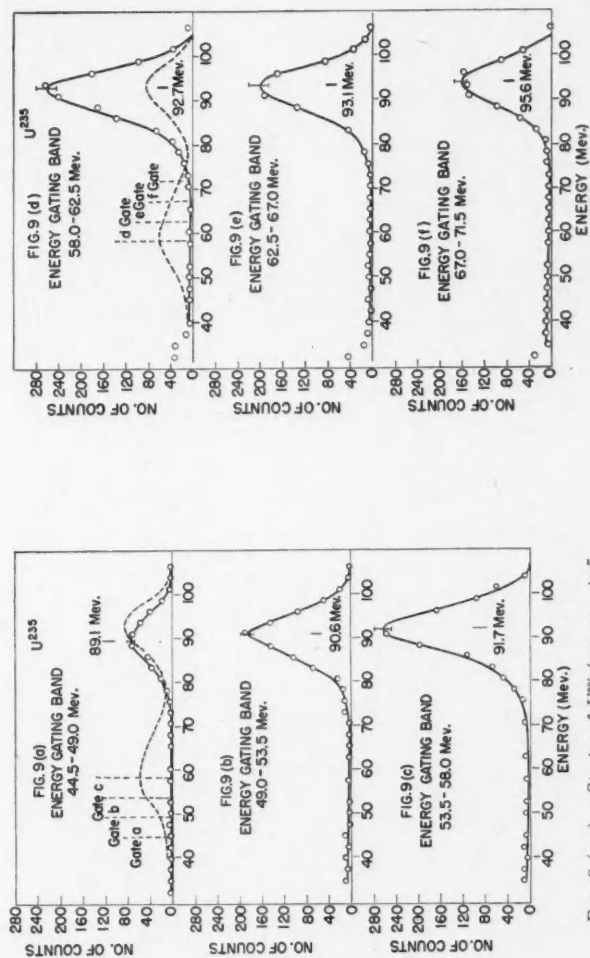
*Most probable energy of light fragment = 94.5 Mev.*

*Most probable energy of heavy fragment = 60.2 Mev.*

### (b) RESULTS WITH $U^{233}$

The experimental conditions using the  $U^{233}$  source were identical with those for  $U^{235}$  except that the higher isotopic purity of the source allowed the use of



FIG. 9 (a-c). Spectra of  $U^{235}$  (energy gate 5 Mev. wide).FIG. 9 (d-f). Spectra of  $U^{235}$  (energy gate 5 Mev. wide).

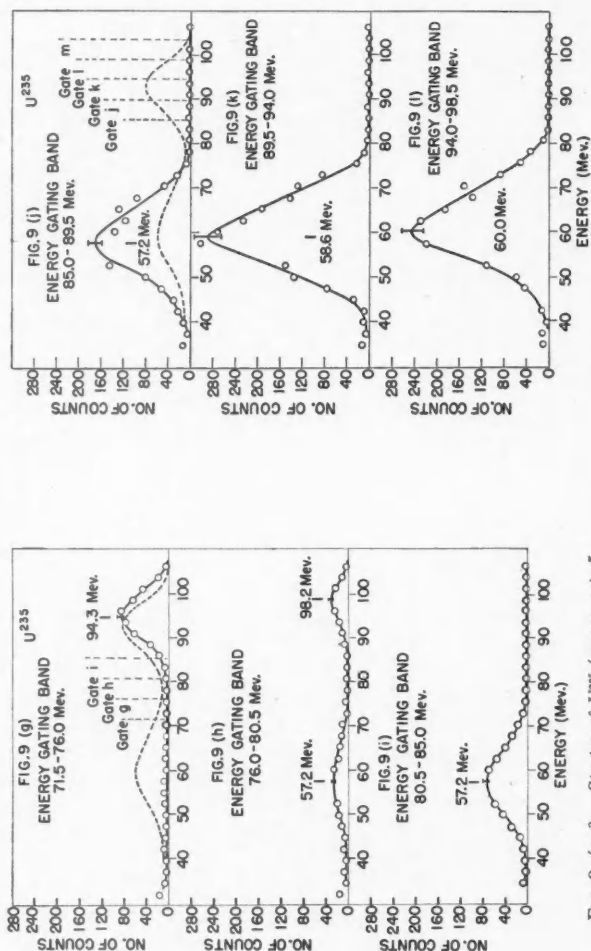
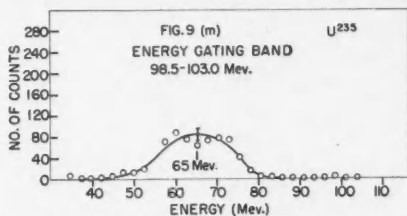
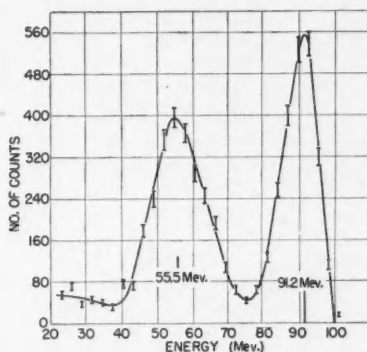


Fig. 9. (g-i). Spectra of  $U^{235}$  (energy gate 5 Mev. wide).

Fig. 9. (j-l). Spectra of  $U^{235}$  (energy gate 5 Mev. wide).

FIG. 9 (m). Spectra of  $U^{235}$  (energy gate 5 Mev. wide).

a lower neutron flux for a reasonable counting rate. This was a practical advantage since the chamber background ionization, which was proportional to the neutron flux, gave considerable "sparking" difficulties at high fields and high fluxes. The total distribution for a wide open gate is given in Fig. 10,

FIG. 10. Spectrum of fragment energies with  $U^{235}$ . Distribution measured with energy gate wide open.

and the partial distributions for a sequence of runs with a 5 Mev. wide gate are shown in Fig. 11 (a - k). Again the curves are uncorrected for source and collimator losses. The corrected values are:

*Most probable energy of light fragment = 93.0 Mev.*

*Most probable energy of heavy fragment = 56.6 Mev.*

## VI. Analysis of Experimental Results

### (a) DEPENDENCE OF GATED DISTRIBUTIONS ON GATING ENERGY

In Table I the results on  $U^{235}$  derived from the normal distribution curves are compared with those of previous workers. In this table the fragment energy values have been left uncorrected for source and collimator loss to form a better comparison with previous work which was likewise uncorrected. It will be noted that the agreement is very satisfactory and that in particular the widths of the distributions indicate adequate resolution in the present experiment.

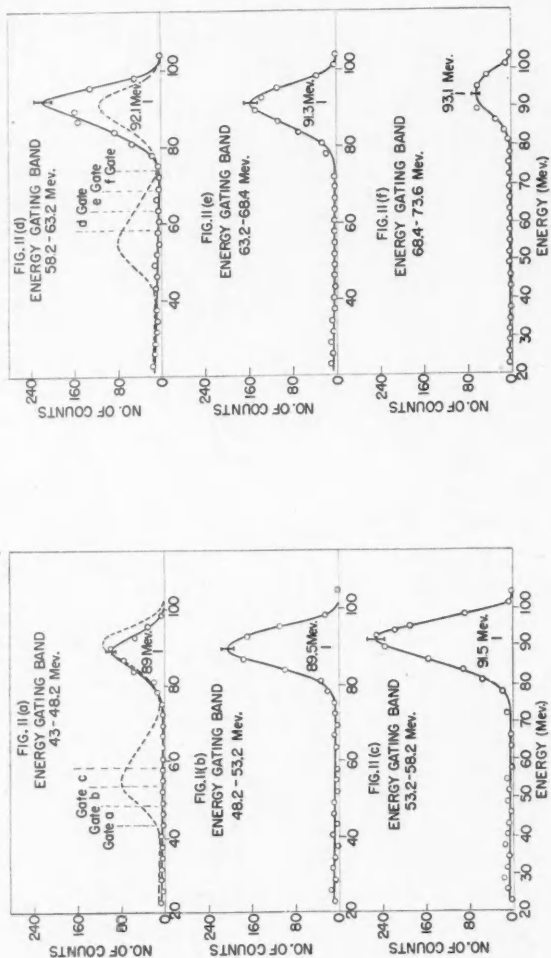
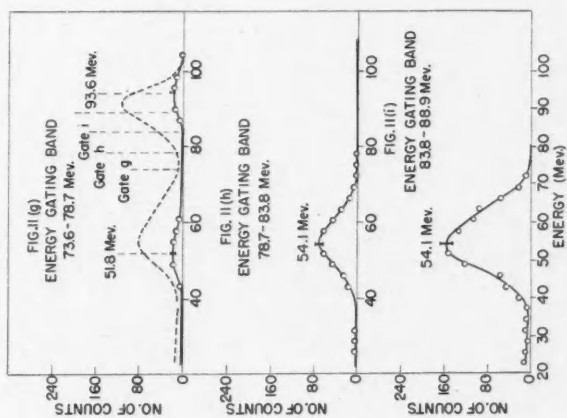
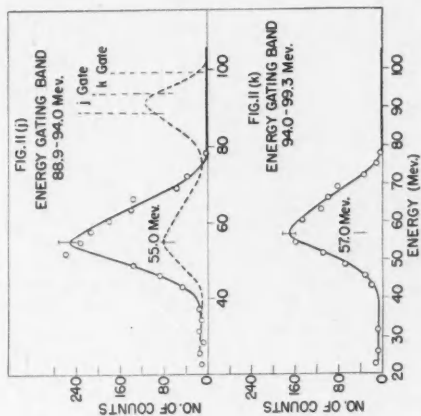


Fig. 11 (d-f). Spectra with  $U^{233}$  (energy gate 5 Mev. wide).

Fig. 11 (a-c). Spectra with  $U^{233}$  (energy gate 5 Mev. wide).

Fig. 11 (g-i). Spectra with  $U_{235}$  (energy gate 5 Mev. wide).Fig. 11 (j,k). Spectra with  $U_{235}$  (energy gate 5 Mev. wide).

The results of the gated runs are rather interesting. When the energy gate is set on the heavy fragment group, the energy distribution of the corresponding light group is almost independent of the position of the gate, and conversely. This result is shown in Tables II and III for the two fissionable materials.

TABLE II  
ANALYSIS OF GATED RUNS WITH  $U^{235}$

Mean energy of gate, Mev.	Coincident distribution	
	Most probable energy, Mev.	Width, Mev. (at half-maximum)
<i>Light fragment group</i>		
Ungated	92.7	12.4
47.0	89.8	12.9
52.0	90.3	11.3
56.0	91.6	11.2
60.2	91.7	11.5
64.6	92.1	11.3
68.9	93.2	12.0
73.3	95.0	12.0
$\Delta E = 26.3^*$	$\Delta E = 5.2^*$	$\Delta E = 1.7^*$
<i>Heavy fragment group</i>		
Ungated	59.0	19.8
78.0	57.4	17.5
83.2	57.3	17.2
87.5	58.5	16.9
91.7	59.6	17.1
96.2	61.7	17.4
$\Delta E = 18.2^*$	$\Delta E = 4.3^*$	$\Delta E = 0.6^*$

\*  $\Delta E$  is the maximum spread for the values in each column.

In each case the partial distribution covers nearly the whole range of the complete spectrum of one group. The distributions are not identical, however, and the shift that does occur is such that as the gating energy is increased, the corresponding distribution maximum also increases. This relationship between the gating energy and the energy of the corresponding maximum is shown in Fig. 12.

Flammersfeld *et al.* (10) presented their results in a manner similar to Figs. 9 and 11, but their statistical accuracy was too low to define accurately the position of the distribution peaks, and no curve similar to Fig. 12 is given. Neither Jentschke (18) nor Deutsch and Ramsey (8) have attempted to show such distribution peaks as the statistical accuracy in both cases is, again, too low. The situation may be summarized by the statement that a heavy frag-

ment of *lower* than average energy for the heavy group will be paired, on the average, with a light fragment of *lower* than average energy. The corresponding situation with *mass* distribution curve is quite different. Since the sum of the

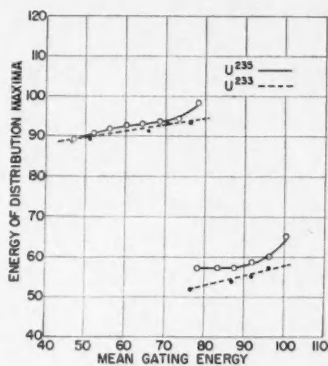


FIG. 12. Variation of most probable energy with the mean gating energy.

TABLE III  
ANALYSIS OF GATED RUNS WITH  $U^{235}$

Mean energy of gate, Mev.	Coincident distribution	
	Most probable energy, Mev.	Width, Mev. (at half-maximum)
<i>Light fragment group</i>		
Ungated	91.2	11.8
46.4	88.5	9.6
50.9	89.6	11.2
55.7	90.7	12.4
60.5	90.7	10.9
65.5	90.3	11.6
70.1	93.1	12.6
76.2	93.8	11.9
$\Delta E = 29.8$	$\Delta E = 5.3$	$\Delta E = 3.0$
<i>Heavy fragment group</i>		
Ungated	55.5	18.6
76.2	52.2	12.9
82.1	54.7	15.3
86.6	55.4	17.7
91.5	56.6	16.8
95.8	58.5	16.5
$\Delta E = 19.6$	$\Delta E = 6.3$	$\Delta E = 3.6$

masses is constant, a heavy fragment of *higher* than average mass for the heavy group must be paired with a light fragment of *lower* than average mass. Thus the double-humped energy distribution curve is not even approximately a simple inversion of the double-peaked mass distribution curve, as was first pointed out by Jentschke and Prankl (17).

Further indication of the relationship between fragment energies may be found by examination of Figs. 9(g) and 11(g). Here the gating band is set on the minimum between the two peaks of the total distribution. If the energy curves were an inverse picture of the mass curves, this experiment would have resulted in a single maximum at the same energy as the gate or perhaps two small maxima very close to this energy. The experimental result, however, is a curve with two maxima close to the energy peaks of the total distribution.

From Tables II and III it may be observed that the width of the gating band ( $\sim 5$  Mev.) can have very little effect on the measurements. Since a shift of mean gating energy of 5 Mev. produces only a small change in the distribution, the spread of energies about the mean through a 5 Mev. band will have considerably less effect. Some runs made with a 2.5 Mev. gate width verified this conclusion.

#### (b) MASS RATIO CURVES

Fig. 13 shows the distribution of mass (or energy) ratio for  $U^{235}$  and  $U^{233}$ . The mass ratio is the reciprocal of the energy ratio, since by conservation of momentum  $E_L M_L = E_H M_H$ , where  $E$  and  $M$  refer to mass and energy and the subscripts  $L$  and  $H$  refer to light and heavy fragments respectively. The curves

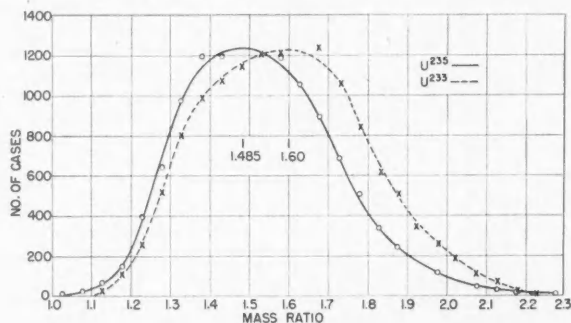


FIG. 13. Mass ratio curves for  $U^{235}$  and  $U^{233}$ .

were computed by determining directly from Figs. 9 and 11 the number of counts in equal energy intervals for a given energy (or mass) ratio and converting these figures to equal mass ratio intervals. The most probable ratios are 1.485 and 1.60 for  $U^{235}$  and  $U^{233}$  respectively. This ratio for  $U^{235}$  may be compared with 1.49 found by Deutsch and Ramsey (8).



## (c) MASS DISTRIBUTION

Figs. 14 and 15 show the mass number curves for  $U^{235}$  and  $U^{233}$  respectively. These curves were computed from the mass ratio curves of Fig. 13 by assuming total masses of 236 and 234 units in the two cases and converting the frequency of occurrence to equal mass intervals. The mass curves from isotopic identi-

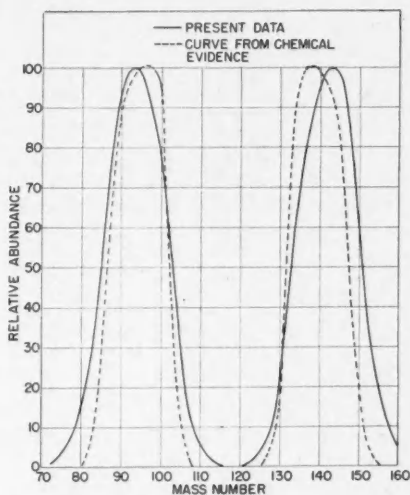


FIG. 14. Mass curve for  $U^{235}$  from present experiment and comparison with chemical curve.

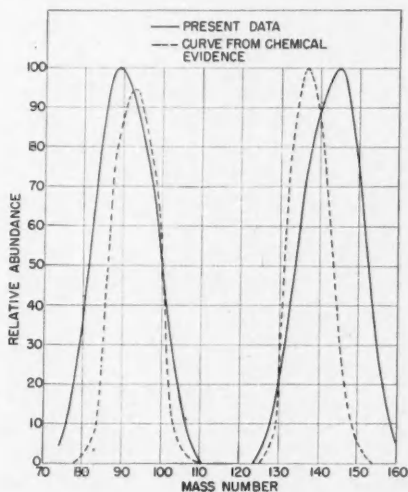


FIG. 15. Mass curve for  $U^{233}$  from present experiment and comparison with chemical curve.

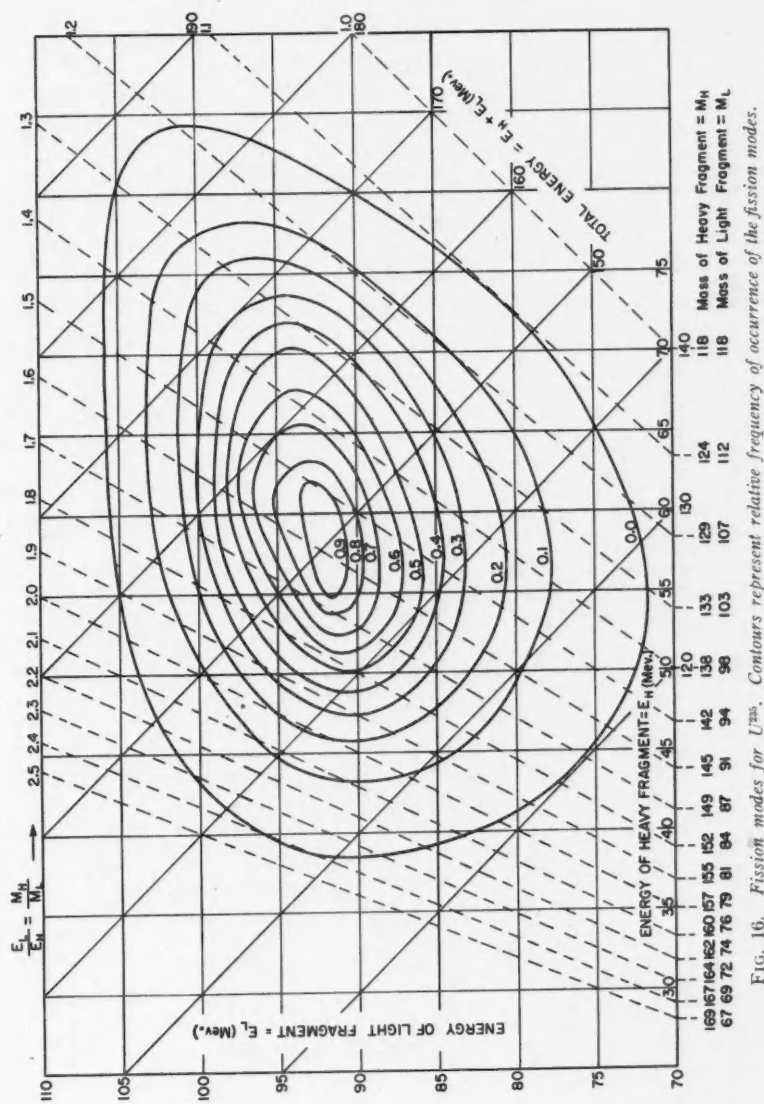
fication of fragment abundance (the "chemical method") are taken from Plutonium Project report (21) and from the paper by Steinberg, Seiler, Goldstein, and Dudley (23). The agreement is not very satisfactory, and especially in regard to the comparison of the peak positions in the  $U^{233}$  curves it is definitely poor. In this case the light fragment peaks differ by approximately 4 and the heavy fragment peaks by 9 mass units. A coincident fission fragment experiment yields, of course, the mass distribution *before* neutron emission whereas the chemical method applies to the fragments *after* neutron emission. Thus a shift towards higher mass must be expected in a coincident pulse experiment. The observed shifts, however, indicate that neutron emission occurs predominantly from the heavy fragment. This conclusion is contrary to the evidence obtained by DeBenedetti, Francis, Preston, and Bonner (7) in their experiment on the angular correlation of fission neutrons. The results of Deutsch and Ramsey (8) give no clear indication of such a shift but the accuracy in their results is hardly better than  $\pm 5$  mass units.

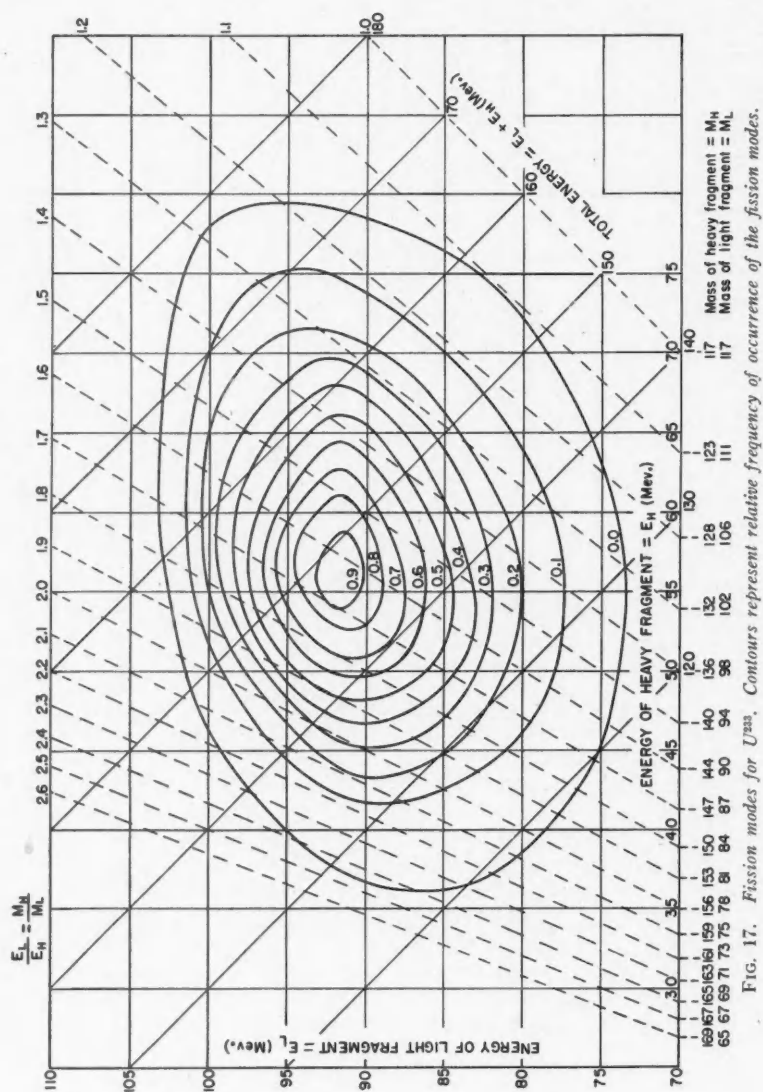
Examination of the curves of Steinberg *et al.* indicates an accuracy of  $\pm 2$  mass units in drawing the curves from the experimental points. In addition the sum of the most probable masses is  $93 + 136 = 229$  which indicates a shift of 5 mass units from the coincident pulse experiment where a total mass of 234 units is assumed. The accuracy of the peak positions from the present experiment is estimated as  $\pm 2$  mass units. It has been found that the mass curves plotted from preliminary data taken with considerably different experimental conditions (different source, collimator of same geometry but six times as thick, chamber filled with pure argon only, resolving time 30  $\mu$ sec.) are in agreement to this accuracy.

If the heavy fragment pulses in the chamber were slightly unsaturated while the light fragment pulses were saturated, the correction to be applied would be in the direction of removing the discrepancy. This condition, however, would have been apparent during the course of the experiment from the energy ratio of the fragments in the most probable case. This ratio was checked with widely varying collecting fields, and even when all pulses were well below saturation (70% of their maximum value) the ratio of the two peaks was unchanged. However, the measured energy ratio may be in error from another cause. As pointed out in Section IV(e), there is good reason to believe that the heavy fragment produces less ionization per Mev. than the light fragment. This would reduce the energy (or mass) ratio. A difference in  $w$  of 2% was estimated in Section IV(e), but it would have to be as high as about 5% to remove the discrepancy between the chemical data and the coincident pulse experiment.

#### (d) CONTOUR DIAGRAMS

Figs. 16 and 17 are contour diagrams of the modes of fission. The energies of the fragments are given by the rectangular co-ordinates and the total kinetic energy and mass ratio are given by the oblique co-ordinates. The contours represent relative frequency of occurrence. These curves are plotted directly





from the data of Figs. 9 and 11 and are uncorrected for source and collimator errors. Neglecting differences in  $w$  for the two fission fragments the most probable mode of fission in  $U^{235}$  is one of total kinetic energy 156 Mev. (corrected

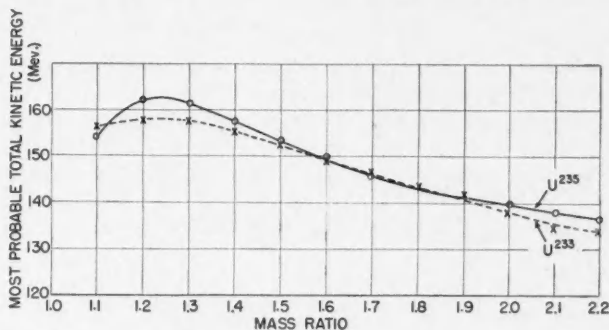


FIG. 18. Variation of the most probable total kinetic energy with mass ratio.

value) and mass ratio 1.57. Corresponding values for  $U^{238}$  are 150 Mev. and 1.64. The two diagrams are on the whole very similar, although in  $U^{238}$  the constant frequency curves are more nearly circular.

#### (e) VARIATION OF KINETIC ENERGY WITH MASS RATIO

Fig. 18 shows the most probable total kinetic energy as a function of mass ratio. The energy increases as the ratio decreases to a value  $\sim 1.25$ . From 1.25 to symmetrical fission, however, the energy decreases. Calculations of total fission energy (kinetic + excitation energies of the fragments) from nuclear masses (e.g., Bohr and Wheeler (1)) show that the total energy increases continuously to unity mass ratio. Consequently, in the region between ratios of 1.25 and unity the excitation energy is increasing rapidly. This decrease in kinetic energy confirms the work of Katcoff, Miskel, and Stanley (20), who require such a condition to explain their range measurements of plutonium fission fragments.

## VII. Discussion of Experimental Results

### (a) RANGE OF KINETIC ENERGIES IN FISSION

The wide range of kinetic energies released in different modes of fission is somewhat surprising. From the contour diagrams (Figs. 16 and 17) the variation in kinetic energy over all modes is about 60 Mev., while the maximum variation associated with a fixed mass ratio is nearly as great ( $\sim 50$  Mev.). For a fixed mass ratio, the total energy release in fission is determined by the difference in mass energy of the uranium nucleus plus a neutron and the mass energy of the final stable nuclei. This variation in total kinetic energy for a fixed mass ratio must arise either from variations in the number of neutrons

emitted or from variations in the primary charge division. The first alternative has been discussed by Way and Wigner (24), the latter has been considered by one of the present authors (3).

(b) COMPARISON OF SLOW NEUTRON FISSION IN DIFFERENT ELEMENTS

Table IV shows a comparison of energy distribution measurements in different materials fissile by slow neutrons. The figures for  $\text{Pu}^{239}$  are taken from the work of Deutsch and Ramsey (8). Again the uncorrected values are used for comparison. There is an indication here that fission becomes more symmetrical as the mass of the fissile nucleus increases. At the same time the total kinetic energy increases, which might be expected since the total available energy also increases as symmetry is approached.

TABLE IV  
COMPARISON OF FRAGMENT ENERGY MEASUREMENTS  
FOR THREE FISSIONABLE MATERIALS

	Present experiment		Deutsch and Ramsey
	$\text{U}^{233}$	$\text{U}^{235}$	$\text{Pu}^{239}$
Most probable energy of the light fragment, Mev.	91.2	92.7	93
Most probable energy of the heavy fragment, Mev.	55.5	59	65
Ratio of most probable energies	1.64	1.57	1.43
Most probable mass ratio (from an equal ratio interval curve)	1.60	1.485	1.32
Width at half-maximum of high energy peak, Mev.	14	12	12
Width at half-maximum of low energy peak, Mev.	22	20	20
Most probable fission mode	Total energy		156
	Mass ratio		1.43

### Acknowledgments

The authors wish to acknowledge the generous assistance of their colleagues in the Nuclear Physics Branch. In particular, special thanks are due to Dr. B. W. Sargent and Mr. A. G. Ward, who were constant sources of help and encouragement, and to Mr. J. McFadden, who assisted throughout the experimental work. In addition, the authors wish to thank the shops and operations staff for their co-operation.

### References

1. BOHR, N. and WHEELER, J. A. Phys. Rev. 56: 426. 1939.
2. BOOTH, E. T., DUNNING, J. R., and SLACK, F. G. Phys. Rev. 55: 981. 1939.
3. BRUNTON, D. C. Phys. Rev. 76: 1798. 1949.
4. BRUNTON, D. C. and HANNA, G. C. Phys. Rev. 75: 990. 1949.
5. BUNEMANN, O., CRANSHAW, T. E., and HARVEY, J. A. Can. J. Research, A, 27: 191. 1949.
6. CRANSHAW, T. E. and HARVEY, J. A. Can. J. Research, A, 26: 243. 1948.
7. DEBENEDETTI, S., FRANCIS, J. E., PRESTON, W. M., and BONNER, T. W. Phys. Rev. 74: 1645. 1948.
8. DEUTSCH, M. and RAMSEY, M. MDDC 945. 1945.

9. ELMORE, W. C. *Nucleonics*, 2: 16. 1948.
10. FLAMMERSFELD, A., JENSEN, P. and GENTNER, W. *Z. Physik*, 120: 450. 1943.
11. FOWLER, J. L. and ROSEN, L. *Phys. Rev.* 72: 926. 1947.
12. FRISCH, D. H. *MDDC* 521. 1946.
13. FRISCH, O. R. *Nature*, 143: 276. 1939.
14. HEALEY, R. H. and REED, J. W. *The behaviour of slow electrons in gases.* The Wireless Press, Sydney, Australia. 1941.
15. HENDERSON, M. C. *Phys. Rev.* 58: 774. 1940.
16. JENTSCHKE, W. and PRANKL, F. *Naturwissenschaften*, 27: 134. 1939.
17. JENTSCHKE, W. and PRANKL, F. *Z. Physik*, 119: 696. 1942.
18. JENTSCHKE, W. *Z. Physik*, 120: 165. 1943.
19. KAMMER, M. H. and BARSCHALL, H. H. *Phys. Rev.* 70: 372. 1940.
20. KATCOFF, S., MISKEL, J. A., and STANLEY, C. W. *Phys. Rev.* 74: 631. 1948.
21. Plutonium Project. *J. Am. Chem. Soc.* 68: 2411. 1946.
22. SNYDER, T. *MDDC* 959. 1945.
23. STEINBERG, E. P., SEILER, J. A., GOLDSTEIN, A., and DUDLEY, A. *MDDC* 1632. 1947.
24. WAV, K. and WIGNER, E. P. *Phys. Rev.* 73: 1318. 1948.
25. WEST, D. *Can. J. Research, A*, 26: 115. 1948.
26. WESTCOTT, C. H. and HANNA, G. C. *Rev. Sci. Instruments*, 20: 181. 1949.

## APPENDIX I

The discriminator proper consists of  $V_1$  and the associated bias setting potentiometer, Fig. 19. Consider first the operation with  $C_2$  omitted. If the input pulse is of greater amplitude than the positive bias applied to the cathode of  $V_1$ , the current flowing through  $V_{3A}$  via  $R_2$  will be diverted through  $V_1$ . Thus if the cathode of  $V_1$  falls  $v_0$  volts below earth, a current of  $(300/R_2 + v_0/R_2)$  will flow into  $C_1$ . If this happens for a time  $\tau$ ,  $n$  times per second there will be a net current through  $V_1$  of  $n\tau(300 + v_0)/R_2$ . The circuit is completed via  $R_1$ , and consequently a shift in the bias level will occur given by  $\frac{n\tau R_1}{R_2}(300 + v_0)$ . This is small here since  $n$  is only 150, and in the worst case  $\tau \approx 20 \mu\text{sec}$ , and  $v_0 = 200 \text{ v}$ , which gives 0.75 v. in 200 v.

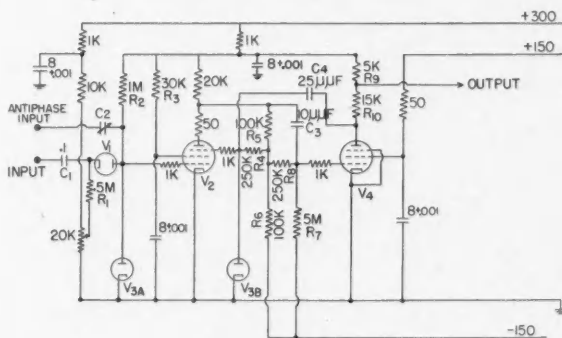


FIG. 19. Discriminator and trigger circuit. This is a detail from the main coincidence discriminator circuit, Fig. 4, and shows  $DL$  and  $T_1$  (or  $DH$  and  $T_2$ ).

$V_1$	$\frac{1}{2}$ 6AL5
$V_2$	6AS6
$V_{3A}$ (and B)	6AL5
$V_4$	6SH7

If substantially higher counting rates were to be employed it would be desirable to eliminate this effect by inserting a cathode follower between  $C_1R_1$  and  $V_1$ .

It should be noted that no d-c. restoration of pulses to the bias line is attempted. Such d-c. restoration is superfluous because of the low counting rate used here. (If counting rates are kept low enough for the probability of pulses sitting on each others' tails to be small d-c. restoration is always unnecessary).

$R_2$  is made fairly small, that is, the standing current through  $V_{3A} = i$  is large, so that steeply falling pulses can be dealt with. If the pulse falls at a rate  $dv_0/dt$ , the self-capacity of  $V_1$  will give rise to a current  $C_{V_1}dv_0/dt$ . If this is less than  $i$  only a small change in the triggering level will result. If it exceeds  $i$  the grid of  $V_2$  will be driven negative (and the trigger circuit fired) while  $V_1$  is still nonconducting. The value  $i = 3$  ma. enables pulses falling at the rate of 200 v. in 0.2  $\mu$ sec. to be tolerated ( $C_{V_1} = 3\mu\text{mf.}$ ).

However this small change in current will cause a very small potential change across  $V_{3A}$  sufficient to trip the trigger circuit since this is extremely sensitive. Rather than decrease this sensitivity it was decided to maintain the facility of dealing with fast pulses by adding a neutralizing condenser  $C_2$ . This is connected to a positive "antiphase" version of the pulse which is already available earlier in the complete circuit. In view of the behavior described above it is clear that fast pulses are acceptable even if  $C_2$  is not exactly correct in value, and with antiphase pulses of slightly different shape (in practice an almost inevitable difficulty).

$V_2$ ,  $V_4$  form a very sensitive trigger circuit which responds to any drop greater than  $\sim 1/10$  v. in the potential of the grid of  $V_2$ .

The main point of interest is the self-stabilization of the anode potential of  $V_2$ , which is achieved by d-c. negative feedback ( $R_5$  and  $R_6$ ) to the suppressor grid, which in this valve has good control of the anode current. The grid of  $V_4$  may then be run very close to the point at which conduction starts in  $V_4$  without the usual danger of instability. It has previously been usual in circuits of this type to avoid this danger either by heavy biasing of  $V_4$  or by running  $V_2$  so that the anode potential in the quiescent state lies below the "knee" of the pentode  $i_a/V_a$  characteristic, with a consequent loss of gain in this stage. Either of these solutions means a large, and consequently somewhat uncertain triggering threshold.

In this circuit the potential of the suppressor grid of  $V_2$  is  $-1 \pm 1$  v. depending on the health of the valve; the anode potential is  $148 \pm 2$  v. if  $R_5$  and  $R_6$  are exactly equal, which is of course not necessary.

By means of  $R_7$  and  $R_8$  the grid potential of  $V_4$  is set 7.5 v. below the suppressor potential of  $V_2$ , that is,  $V_4$  is run with a bias of  $8.5 \pm 1$  v.

The gain between grid and anode of  $V_2$  is about 100 for fast pulses ( $C_4$



"holding" the suppressor) and thus the uncertainty of 1 v. in the level of  $V_4$  grid is reflected as a 1/50 v. uncertainty in the triggering level at the grid of  $V_2$ . Since it requires a positive pulse of amplitude about 4 v. on the grid of  $V_4$  to cause conduction the triggering level is about 1/12 v.

The grid of  $V_4$  will respond to fast pulses by virtue of  $C_3$  which is made approximately equal to the input capacity of  $V_4$ , thus giving an essentially aperiodic coupling network.

The time constant  $C_4R_4$  determines the length of trigger pulse produced. If, however, the operating pulse holds  $V_2$  in the cutoff state for a longer period than this, it prevents the circuit recovering. Consequently in this case a pulse is produced of duration equal to the time  $V_2$  is cut off. This behavior is frequently an advantage as it avoids double triggering on any spurious long pulse.

If, as in this case, the full gain of  $V_2$  is to be exploited, that is, the valve run right up to its rating, it is particularly important to consider the screen dissipation. A wide range of valve performances was encountered in practice. Consequently a circuit designed to work satisfactorily with the poorest valve will, if a good valve is inserted, divert a large current to the screen. This precludes running the screen from a constant voltage source. Rather  $R_3$  must be made large enough (and a consequently higher supply line voltage used) so that the screen dissipation is automatically limited. This means that at high counting rates the screen potential will fall and the triggering level will change, but this effect is exceedingly small in the present application. With this exception there will be no change in any operating conditions with repetition frequency.

The reason for splitting the anode load of  $V_4$  is merely that a relatively low output was needed and the capacitive loading on  $V_4$  could thus be reduced.

## APPENDIX II

### Pulse Duration

The pulse rise and pulse length are determined by the main amplifier time-constants—the equivalent circuit is shown in Fig. 20, where we neglect the loading of  $C_2R_2$  on  $C_1R_1$ .

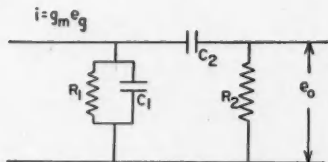


FIG. 20. Equivalent circuit for main amplifier band width control.

The pulse duration will depend slightly on the shape of the pulse rise from the electron collection in the chamber, but when the amplifier rise time con-

stant is longer than the collection time a close approximation to the true pulse duration is obtained using a step function input pulse.

A simple analysis of the transient response of this circuit is achieved using the Laplace Transform method (9).

For a unit step function input voltage  $e_g$  the output voltage  $e_0$  is given by

$$e_0 = e_g G \frac{\tau_2}{\tau_2 - \tau_1} (e^{-t/\tau_2} - e^{-t/\tau_1}),$$

where  $G = g_m R_1$ ,  $\tau_1 = C_1 R_1$  and  $\tau_2 = C_2 R_2$ .

To calculate the time at which the pulse reaches its maximum amplitude we set  $de_0/dt = 0$ . That is,

$$-\frac{1}{\tau_2} e^{-t_m/\tau_2} + \frac{1}{\tau_1} e^{-t_m/\tau_1} = 0, \text{ where } t = t_m, \text{ for } e_0 = e_{0 \max}.$$

$$\therefore t_m = \frac{\tau_2}{\lambda - 1} \ln \lambda, \text{ where } \lambda = \frac{\tau_2}{\tau_1}.$$

$$\therefore e_{0 \max} = G e_g \lambda^{1/1 - \lambda}.$$

$$\frac{e_0}{e_{0 \max}} = K (e^{-t/\tau_2} - e^{-t/\tau_1}) \quad \text{where } K = \frac{\lambda (\frac{\lambda}{\lambda - 1})}{\lambda - 1}$$

$$= 2K e^{-\alpha t} \sinh \beta t \quad \text{where } \alpha = \frac{\lambda + 1}{2\tau_2} \quad \beta = \frac{\lambda - 1}{2\tau_2}.$$

Case (a): time  $t_1$  for pulse to decay to 20% of its maximum amplitude.

$$\text{i.e., } \frac{e_0}{e_{0 \max}} = 0.2.$$

$$\frac{e^{\alpha t_1}}{\sinh \beta t_1} = 10 K.$$

Values of  $\tau_1$  and  $\tau_2$  in the amplifier are somewhat uncertain owing to stray capacities. The values  $\tau_1 = 1 \mu\text{sec.}$ ,  $\tau_2 = 5 \mu\text{sec.}$  fit the measured pulse shape reasonably closely. With these values  $\lambda = 5$ ,  $K = 1.87$ ,  $\alpha = 0.6$ ,  $\beta = 0.4$ ,

$$\text{then, } t_1 = 11.25 \mu\text{sec.}$$

Case (b):  $t_1 = 5\tau = 56.25 \mu\text{sec.}$

$$\begin{aligned} \frac{e_0}{e_{0 \max}} &= 3.74 e^{-33.75} \sinh 22.5 \\ &\approx 2 \times 10^{-5}. \end{aligned}$$

Case (c):  $t_1 = 20 \mu\text{sec.}$

$$\begin{aligned} \frac{e_0}{e_{0 \max}} &= 3.74 e^{-12} \sinh 8 \\ &\approx 0.03. \end{aligned}$$

Case (d): time  $b\tau$  (see Section IV(c), 1(ii)) for a 70 Mev. pulse to decrease from 8.5 Mev. to 3.5 Mev.

Let  $t_1$  and  $t_2$  be the times for the pulse to reach  $\frac{8.5}{70} = 0.12$  and  $\frac{3.5}{70} = 0.05$  of the maximum respectively,

then  $t_1$  is given by 
$$\frac{e^{0.6 t_1}}{\sinh 0.4 t_1} = 31.2,$$

from which

$$t_1 = 13.75,$$

similarly

$$\frac{e^{0.6 t_2}}{\sinh 0.4 t_2} = 75,$$

from which

$$t_2 = 18.15 \mu\text{sec}.$$

$$b\tau = t_2 - t_1 = 4.4 \mu\text{sec}.$$



## CANADIAN JOURNAL OF RESEARCH

### Notes on the Preparation of Copy

**GENERAL:**—Manuscripts should be typewritten, double spaced, and the **original and one extra copy** submitted. Style, arrangement, spelling, and abbreviations should conform to the usage of this Journal. Names of all simple compounds, rather than their formulae, should be used in the text. Greek letters or unusual signs should be written plainly or explained by marginal notes. Superscripts and subscripts must be legible and carefully placed. Manuscripts should be carefully checked before being submitted, to reduce the need for changes after the type has been set. If authors require changes to be made after the type is set, they will be charged for changes that are considered to be excessive. **All pages, whether text, figures, or tables, should be numbered.**

**ABSTRACT:**—An abstract of not more than about 200 words, indicating the scope of the work and the principal findings, is required.

#### ILLUSTRATIONS:

(i) **Line Drawings:**—All lines should be of sufficient thickness to reproduce well. Drawings should be carefully made with India ink on white drawing paper, blue tracing linen, or co-ordinate paper **ruled in blue only**; any co-ordinate lines that are to appear in the reproduction should be ruled in black ink. Paper ruled in **green, yellow, or red should not be used** unless it is desired to have all the co-ordinate lines show. Lettering and numerals should be neatly done in India ink preferably with a stencil (**do not use typewriting**) and be of such size that they will be legible and not less than one millimeter in height when reproduced in a cut three inches wide. All experimental points should be carefully drawn with instruments. Illustrations need not be more than two or three times the size of the desired reproduction, but the ratio of height to width should conform with that of the type page. **The original drawings and one set of small but clear photographic copies are to be submitted.**

(ii) **Photographs:**—Prints should be made on glossy paper, with strong contrasts; they should be trimmed to remove all extraneous material so that essential features only are shown. Photographs should be submitted **in duplicate**; if they are to be reproduced in groups, one set should be so arranged and mounted on cardboard with rubber cement; the duplicate set should be unmounted.

(iii) **General:**—The author's name, title of paper, and figure number should be written in the lower left hand corner (**outside the illustration proper**) of the sheets on which the illustrations appear. Captions should not be written on the illustrations, but typed on a separate page of the manuscript. All figures (including each figure of the plates) should be numbered consecutively from 1 up (arabic numerals). **Each figure should be referred to in the text.** If authors desire to alter a cut, they will be charged for the new cut.

**TABLES:**—Titles should be given for all tables, which should be numbered in Roman numerals. Column heads should be brief and textual matter in tables confined to a minimum. **Each table should be referred to in the text.**

**REFERENCES:**—These should be listed alphabetically by authors' names, numbered in that order, and placed at the end of the paper. The form of literature citation should be that used in the respective sections of this Journal. **Titles of papers should not be given in references listed in Sections A, B, E, and F, but must be given in references listed in Sections C and D.** The first page only of the references cited in papers appearing in Sections A, B, and E should be given. **All citations should be checked with the original articles.** Each citation should be referred to in the text by means of the key number; in Sections C and D the author's name and the date of publication may be included with the key number if desired.

The *Canadian Journal of Research* conforms in general with the practice outlined in the *Canadian Government Editorial Style Manual*, published by the Department of Public Printing and Stationery, Ottawa.

### Reprints

Fifty reprints of each paper without covers are supplied free. Additional reprints, if required, will be supplied according to a prescribed schedule of charges. On request, covers can be furnished at cost.



